INFORMATION TO USERS

This manuscript has been reproduced from the microfilm master. UMI films the text directly from the original or copy submitted. Thus, some thesis and dissertation copies are in typewriter face, while others may be from any type of computer printer.

The quality of this reproduction is dependent upon the quality of the copy submitted. Broken or indistinct print, colored or poor quality illustrations and photographs, print bleedthrough, substandard margins, and improper alignment can adversely affect reproduction.

In the unlikely event that the author did not send UMI a complete manuscript and there are missing pages, these will be noted. Also, if unauthorized copyright material had to be removed, a note will indicate the deletion.

Oversize materials (e.g., maps, drawings, charts) are reproduced by sectioning the original, beginning at the upper left-hand corner and continuing from left to right in equal sections with small overlaps. Each original is also photographed in one exposure and is included in reduced form at the back of the book.

Photographs included in the original manuscript have been reproduced xerographically in this copy. Higher quality 6" x 9" black and white photographic prints are available for any photographs or illustrations appearing in this copy for an additional charge. Contact UMI directly to order.

UMI

A Bell & Howell Information Company
300 North Zeeb Road, Ann Arbor MI 48106-1346 USA
313/761-4700 800/521-0600

A Study of Turbulence and Fine Scale Temperature Variability of the Ocean Thermal Boundary Layer Under Breaking Surface Waves

by

Johannes Richard Gemmrich
Diplom in Meteorologie, Christian Albrechts Universität, Kiel, Germany, 1990

A Dissertation Submitted in Partial Fulfillment of the
Requirements for the Degree of
DOCTOR OF PHILOSOPHY
in the Department of Physics and Astronomy

We accept this dissertation as conforming to the required standard

Dr. D. M. Farmer, Supervisor (Department of Physics and Astronomy and Institute of Ocean Sciences, Sidney, B.C.)

Dr. C. J. R. Garrett, Department Member (Department of Physics and Astronomy)

Dr. R. G. Lueck, Outside Member (School of Earth and Ocean Sciences)

Dr. N. Djilali, Outside Member (Department of Mechanical Engineering)

Dr. J. N. Moum, External Examiner (Oregon State University, Corvallis, Oregon)

University of Victoria

Supervisor: Dr. David M. Farmer

ABSTRACT

Although turbulence near the ocean surface is of great significance to the air-sea exchange of heat, gas and momentum it is a poorly understood phenomenon especially at high wind speeds when vertical transfer processes tend to be greatest. This work evaluates ocean surface turbulence at high sea states by exploiting heat as a naturally occurring passive tracer. To this end, a freely drifting instrument with a mechanically driven temperature profiler, fixed depth thermistors and conductivity cells was used to monitor the fine scale temperature structure and breaking wave activity. These open ocean measurements form the basis for a comprehensive account of the near surface turbulence field. Temperature profiles reveal a rich fine structure which, when combined with independent air-sea heat flux measurements reveal the presence of a surface layer of wave enhanced turbulence, modulated by subsurface advection associated with Langmuir circulation. The concept of wave enhanced turbulence, previously based on observations in fetch limited environments, is here extended to open ocean storm conditions.

Generation of turbulence depends on the scale and frequency of breaking events. Our observations, which span a wide range of conditions from a coastal strait to the open ocean, show that wind speed or wave age are inadequate predictors of the occurrence frequency of wave breaking, motivating a scaling based on energy input. The decay of turbulence following wave breaking proceeds more rapidly than for isotropic turbulence, permitting generation of a thermal boundary layer a few centimetres thick, which accounts for brief temperature fluctuations observed beneath breaking waves. Advection due to Langmuir circulation also leaves its signature on the near surface temperature field. Both advection and enhanced diffusion are reconciled in a two-dimensional model of the upper ocean boundary layer, providing a framework for studying Langmuir circulation and upper ocean turbulence in terms of the measured temperature structure. The depth integrated dissipation derived from a model analysis of the data closely matches the energy input into the wave field, identifying breaking waves as the major source of turbulent kinetic energy.

Examiners:

Dr. D. M. Farmer, Supervisor (Department of Physics and Astronomy and
Institute of Ocean Sciences, Sidney, B.C.)

Dr. C. J. R. Garrett, Department Member (Department of Physics and Astronomy)

Dr. R. G. Lueck, Outside Member (School of Earth and Ocean Sciences)

Dr. N. Djilali, Outside Member (Department of Mechanical Engineering)

Dr. J. N. Moum, External Examiner (Oregon State University, Corvallis, Oregon)

Table of Content

List of Tables

List of Figures

Acknowledgments

First of all, I thank Dr. David Farmer for the opportunity to work on this exciting research project. The thesis work would not have been possible without his insight and enthusiasm. He also provided me with financial support which is highly appreciated.

I am very grateful for the help offered by my committee members. In particular I thank Dr. Chris Garrett for giving generously of his time and ideas, Dr. Rolf Lueck for his guidance on technical aspects of this work and Dr. Ned Djilali for serving as a committee member.

I am indebted to Grace Kamitakahara-King, Willi Weichselbaumer and Vadim Polonichko for helping to solve numerous computing problems. Thanks are due to Alan Adrian, Nick Hall-Patch, Don Lapshinoff and Ron Teichrob for designing, building and constantly upgrading the instrumentation and to the crews of R/V Parizeau, R/V John P. Tully and R/V Wecoma for making data collection under severe conditions possible.

Dr. Peter Craig kindly provided me with the code for his turbulence closure model which is greatly appreciated. I also thank Dr. Jim Edson for the meteorological data for one of the experiments and Dr. Mark Trevorrow and Vadim Polonichko for processing the acoustical data. Gray Campbell is thanked for proof-reading the thesis.

Thanks go to all my fellow students and colleagues at the Institute of Ocean Sciences; it has been a pleasure working with you. Finally, I thank Angela Kleine-Büning for her support and patience.

SMS Gazelle

First German research vessel used to study waves and temperature structure in the open ocean (March 10, 1874 - May 12, 1876)

1. Introduction

1.1 Context

Covering more than 70% of the earth's surface, the air-sea interface forms the most important boundary for the atmosphere as well as the ocean. Essentially all energy entering the ocean has to pass through this interface, geothermal heating and tides being the primary exceptions.

The heat capacity of the top 2.5 m of the world oceans is equal to the entire heat capacity of the dry atmosphere [Gill, 1982], making the ocean far more efficient in global heat transport than the atmosphere, and through an interplay of storage and release of heat in and from the ocean surface layer the diurnal and seasonal variability of air temperature in the marine boundary layer is smoothed.

The exchange of momentum, heat, gases and particles between the atmosphere and ocean is mainly governed by processes within the ocean surface layer. While suppression of this transfer to molecular transport close to the surface results in a viscous (in the case of momentum transfer) and molecular sublayer (for heat and gases) of typically less than 1 mm thickness the transport occurs generally via turbulent motions. The thermal molecular boundary layer, often called the cool skin [e.g. Hasse, 1971, Katsaros, 1980], attracted attention due to its significance to remote sensing [Schlüssel *et al.*, 1990]. Less is known about certain aspects of the turbulence in the ocean surface layer. As shown within this thesis the near surface layer is a very energetic environment and approximately 88% of the kinetic energy transferred from the wind to the ocean is dissipated within the upper two metres. Thorpe [1995] divides oceanic near surface turbulence into four classes.

- active turbulence generated by breaking surface waves and by the motion of bubbles generated in the process of breaking,
- turbulence resulting from the impact of precipitation,
- turbulence generated by coherent motions of Langmuir circulation and thermal convection,
- internal turbulence due to the shear stress of a mean flow.

At moderate to high wind speeds the combined action of breaking waves and Langmuir circulation dominate the air-sea exchange processes on the aquatic side. These form the link, which is the main focus of this work, between the diffusive process close to the air-sea interface and the advective field of Langmuir circulation.

The most apparent process occurring at the ocean surface is the breaking of surface gravity waves and visible air entrainment manifested as whitecapping. Breaking waves are known to be an important mechanism for the transfer of gas [Thorpe, 1982; Kitaigorodskii, 1984; Woolf & Thorpe, 1991; Farmer *et al.*, 1993; Keeling, 1993], momentum [Melville & Rapp, 1985; Lamarre & Melville, 1991] and salt and water droplets [Bortkovskii, 1987; Ling, 1993] between the atmosphere and ocean, and they are responsible for the dissipation of wave energy [Melville & Rapp, 1985; Rapp & Melville, 1990; Agrawal *et al.*, 1992], thus being a source of the turbulent kinetic energy of the surface layer. However, their contribution to the vertical transport of heat is less clear.

Laboratory measurements [e.g. Duncan, 1981; Rapp & Melville, 1990; Skyner & Greated, 1992] provide useful insight on the dynamics of breaking waves, yet the scaling of the results to natural conditions remains open. The ocean surface layer during a storm is a very hostile environment for direct measurements, and field observations of even the size and frequency of breaking waves are sparse, leaving little guidance for the interpretation of laboratory results.

Measurements of velocity fluctuations in the surface layer in Lake Ontario at significant wave heights of ~ 0.3 m [Agrawal *et al.*, 1992] provided the first evidence of enhanced near surface turbulence, attributed to breaking waves. However, the applicability of these results to open ocean conditions has yet to be established. A few turbulence shear probe measurements in the ocean surface layer [Anis & Moum, 1992; Osborn *et al.*, 1992; Anis & Moum, 1995] show enhanced turbulence levels. However, these observations were all taken at moderate wind speeds and limited fetch conditions. Nevertheless, simple mixed layer models [Craig & Banner, 1994; Terray *et al.*, 1996] are starting to include wave enhanced turbulence.

Another important feature of the surface layer is Langmuir circulation [Langmuir, 1938]. To a first order approximation this consists of counter-rotating longitudinal cells, roughly aligned with the wind direction. Due to their ability to accumulate microbubbles within the convergence region, active acoustics provides a means for remotely monitoring their spatial and velocity structure [Thorpe, 1984; Smith, 1992; Farmer *et al.*, 1997]. Langmuir circulation is not only thought to enhance air-sea gas transfer by trapping gas bubbles at several metres depth [Farmer *et al.*, 1993], but also plays a significant role in regulating biological activity [Denman & Gargett, 1995] by vertical mixing of nutrients as well as pollutants and advection of phytoplankton into the sunlit near surface region. However, beside observations of temperature fluctuations beneath bubble clouds [Thorpe & Hall, 1987], which could not unambiguously be connected to Langmuir circulation, little observational evidence exists to evaluate their role in mixing of heat.

Only well defined small scale processes are amenable to direct simulations, whereas numerical models of large and meso-scale processes like climate, weather and ocean circulation have to rely on parameterization of subgrid processes. Air-sea exchange processes are usually represented by bulk exchange coefficients, relating the flux through the interface to bulk quantities on either side. The parameterizations are intended to represent the unresolved processes; a noticeable example is the influence of the wave field on the exchange coefficients of momentum, heat and moisture [*e.g.* Donelan, 1990]. Yet, the parameterization is often empirical and neglects the physics of the small scale processes. Furthermore, the same parameterizations are used for different quantities without a clear understanding of their physical basis. Also, any parameterization lacks generality if only based on empirical grounds, a restriction especially serious in studies of changing conditions such as climate change. It is therefore important to improve our understanding of the physics governing small scale processes, which might be of great importance on a global scale.

1.2 Basic goals and thesis plan

The overall objective of this project is to improve our physical understanding of small scale processes relevant to air-sea exchange primarily of heat, gases and momentum at high wind speeds, and in particular to build a framework for utilizing observations of the fine scale temperature variability in the analysis of the near surface turbulence field. These tasks were addressed in the following way.

Prior to this work no turbulence measurements within the top metre of the ocean during high wind speeds were available. In this thesis it is shown that utilizing heat as a naturally occurring passive tracer allows us to observe turbulence in this hostile environment where conventional velocity and shear probe measurements have not previously been used. Thus, the concept of wave enhanced turbulence, which so far is primarily based on measurements in a fetch limited lake environment [Agrawal *et al.*, 1992] and at moderate wind speeds [Anis & Moum, 1992; Osborn *et al.*, 1992; Anis & Moum, 1995], can be tested in the open ocean at high sea states.

Turbulence levels are expected to depend on the size, frequency and air entrainment of breaking waves. Despite its importance to oceanographers and meteorologists [Banner & Donelan, 1992], knowledge of turbulence is limited by the lack of field observations. Extensive data sets on properties of breaking waves under a variety of forcing conditions, collected during the course of this project, provide a basis for addressing the question of the scales of breaking waves.

The thesis is structured in the following way. Chapter 2 summarizes the background necessary for the study of turbulence and the thermal variability of the ocean surface layer. The terminology is introduced and prior work briefly reviewed. The measurement approach and in particular the description of a novel instrument for monitoring breaking waves and the near surface temperature structure, as well as a description of the supporting measurements, are given in chapter 3. Data were gathered during four large scale experiments in the open ocean and in a coastal strait. Descriptions of these experiments including accounts of the meteorological and oceanographic conditions are presented in chapter 4. Chapter 5 contains the analysis of these data, which is split into two major sections. The first deals with the generation of turbulence due to breaking waves. This includes the discussion of scales and frequency of occurrence of breaking waves and corresponding air entrainment under a wide variety of conditions. In the second part near surface turbulence as manifested in the fine scale temperature structure is analyzed. Temperature variability is attributed to breaking and Langmuir circulation. Chapter 6 describes the modeling of the near surface temperature variability, which links the turbulence of breaking waves with the advective field of Langmuir circulation. The starting point is a one-dimensional turbulence closure model [Craig & Banner, 1994] which incorporates the injection of the turbulent kinetic energy via breaking waves. Based on the insight on mean turbulence levels a model of the decay of turbulence beneath breaking waves is developed. Inclusion of the advective field of Langmuir circulation leads to a two-dimensional advective-diffusion model of the ocean surface layer. This model provides a basis for interpreting upper ocean temperature measurements. All three model components are evaluated against the observations. Chapter 7 summarizes the chief scientific findings of this work.

2. Background

2.1 The ocean thermal boundary layer

The density of water is roughly 800 times that of air and hence the ocean surface layer can in most cases be treated as a wall bounded layer. Modifications arise due to surface waves and clearly within breaking waves a wall approximation is not appropriate. Nevertheless, a wall type boundary layer serves as a valid reference and the basic physics will be reviewed in the following.

The ocean surface exchanges heat with the atmosphere through radiation and turbulent fluxes. The heat has to be removed (for the case of net outgoing heat flux) or stored (for the case of net incoming heat flux) in the bulk of the water, thus causing a vertical temperature gradient which is described by the following flux gradient relation:

$$\frac{\partial T}{\partial z} = -\frac{1}{c\rho k(z)} Q(z)\,. \tag{2.1}$$

c is the heat capacity, ρ the density, k the effective thermal diffusivity and Q the heat flux through the boundary. The total heat flux is the result of the concerted action of radiative and turbulent fluxes and is given by:

$$Q(z) = \lambda(z)\,(1 - \alpha)\,SW + (H + LE + IR) \tag{2.2}$$

SW represents the incoming solar radiation (short-wave), H the sensible heat flux, LE the latent heat flux, IR the net infra red radiation, which is the sum of outgoing infra red radiation and incoming atmospheric back radiation, α is the albedo of the sea surface and $\lambda(z)$ is a depth dependent absorption factor for short-wave radiation.

The effective thermal diffusion coefficient is the sum of the molecular diffusivity and turbulent eddy diffusivity. The latter can be parameterized as

$$k_T \propto l_m q \tag{2.3}$$

where q is the mean turbulence velocity and the mixing length l_m represents the distance which a fluid parcel has to travel before it mixes completely with the new surrounding. This parameterization is valid for any downgradient mixing process. In the case of a wall bounded layer it takes the form:

$$k_T = \kappa\, u_* z\,, \tag{2.4}$$

where u_* is the friction velocity $\kappa = 0.4$ is the von Karman constant and z the distance from the wall. An expression more appropriate for the wind driven ocean surface layer was recently proposed by Craig & Banner [1994]. This will be discussed in more detail in chapter 6.

According to wall layer theory turbulence is suppressed close to the sea-air interface, and heat has to be transported mainly by molecular diffusion. This results in a strong vertical temperature gradient close to the interface which is commonly described as the *cool skin* and was first observed about 50 years ago [Bruch, 1940; Woodcock, 1941]. The terminology refers to the common situation in mid and high latitudes where the sum of H, LE and IR is generally positive, i.e. the ocean is losing heat. However, during strong insolation and light wind, which in turn reduces the turbulent fluxes, a warm skin can build up. The thickness δ of the cool skin is of order of 1 millimeter and the temperature drop is typically a few tenths of a degree, however values of $\Delta T > 1.5$K have been observed [Katsaros, 1980].

On dimensional grounds the thickness of the viscous sublayer scales as:

$$\delta_v \propto \frac{v}{u_*} \tag{2.5}$$

where v is the kinematic viscosity.

Assuming the thermal molecular sublayer thickness being proportional to the thickness of the viscous sublayer $\delta \propto \delta_\upsilon$ yields [Saunders, 1967]

$$\Delta T = C \frac{\upsilon \,(LE + H + IR)}{k \; u_*} \tag{2.6}$$

The factor of proportionality C turned out to be wind dependent, varying from about 2 to 10. [e.g. Saunders, 1967; Hasse, 1971; Graßl, 1976; Simpson & Paulson, 1980; Kent *et al.*, 1996]

The significance of the cool skin is twofold. Firstly, sea surface temperature derived from satellite borne radiometers represents the skin temperature, whereas traditionally water temperature is sampled within the bulk of the water at 0.2 m - 2.5 m depth. Therefore, parameterizations based on the bulk water temperature have to be corrected, if driven by remotely sensed temperature values. Secondly, the solubility of CO_2 in salt water is temperature dependent, increasing by roughly 3% per 1 K cooling. Robertson and Watson [1992] estimate the modeled oceanic global uptake of CO_2 could increase as much as 0.7 Gt C yr^{-1} if the partial pressure of CO_2 measured in the surface layer was corrected for the skin effect.

A series of simultaneous measurements of radiometric and bulk SST in the Northeast Atlantic [Schlüssel *et al.*, 1987, 1990] and in the equatorial Pacific [Coppin *et al.*, 1991] confirmed the existence of the cool skin. The study in the equatorial region, where winds are predominantly light and the sky overcast, showed a mean temperature deviation $T(z)-T(skin) = \Delta T = +0.3$ K, out of a sample of 460 15 minutes averages, with very few negative values. Schlüssel *et al.* [1990] generally found largest temperature deviations during nighttime. The temperature deviation increases with decreasing cloud coverage and decreases for increasing wind speed. Under an overcast sky with light winds the average ΔT was negative during daytime. For all other conditions average values were between 0.16 K and 0.33 K.

In situ measurements of the cool skin are extremely difficult, due to the small vertical extension of the skin and its possible disruption by the measuring probe. Nevertheless, measurements of Mammen & von Bosse [1990] with a rapidly sampling temperature sonde combined with a surface detector did resolve the cool skin at least during relatively calm conditions. Only a few examples are given, with δ varying between 5×10^{-4} m and 5×10^{-3} m and ΔT from 0.05 K to 0.3 K. Some of their profiles suggest the action of small-scale convection rolls, known as surface renewal, which was theoretically postulated by Liu & Businger [1975] and supported by recent observations under natural conditions [Gemmrich & Hasse, 1992].

Below the cool skin heat is believed to be mixed like a passive tracer by wall type turbulence. Turbulence is created by momentum input from the atmosphere by shear stress which remains constant within a certain layer, and the temperature profile in the so called *constant stress layer* has to be adiabatic. Beside the forced turbulence due to shear stress further mixing can be provided by convection. The relative importance of convection is expressed in terms of the Monin-Obukhov Length:

$$L = -\frac{u_*^3}{k\,B} \tag{2.7}$$

where

$$B=\frac{g\alpha\, Q}{c_p}+g\beta\ (E-P)\ S \tag{2.8}$$

is the buoyancy flux, α and β are the thermal and haline expansion coefficients, respectively, E and P are evaporation and precipitation, respectively and S is salinity. Generally, the thermal buoyancy flux is much larger than the haline contribution and the second term in (2.8) is often neglected. Within layers shallower than L turbulence production is dominated by forced convection, i.e. mechanically introduced turbulence, whereas at depths below L free convection is the main source of turbulence.

2.2 Breaking surface waves

Surface waves are the most energetic motions in the ocean mixed layer. As the waves break this energy is released into the upper ocean and breaking waves are thought to be a major factor in turbulence generation. Wave breaking occurs when the particle velocity of the fluid at the crest exceeds the phase speed of the wave. This is the basic definition of a breaking wave. For irrotational waves this definition is equivalent to a limiting wave form with a crest angle of 120° [Stokes, 1880], which implies a wave slope of 1/7. The dynamical criterion for wave breaking states that the particle acceleration at the crest equals half the gravitational acceleration.

The most dramatic form of breaking is found in plunging breakers, where the waves overturn and a sheet of moving water plunges down at some distance forward from the wave crest. This type of breaking is most common in shallow water and on beaches. In deep water the common breakers are spilling breakers where a turbulent current of crest-water spills down the forward face of the wave. Air entrainment during this process appears as white capping. Wave breaking without air entrainment, the so called micro-scale breaking, occurs at wave heights of only a few centimetres and is therefore often overlooked. Yet, micro scale breakers are widespread even at low wind speeds and may play an important role in air-sea exchange processes [Wu, 1995].

Despite the long history of breaking wave studies no comprehensive theory of wave breaking has yet been established. However, numerical modeling of plunging breakers up to the point where the surface impacts on itself [Dold & Peregrine, 1986] and simple models of spilling breakers are available [Longuet-Higgins & Turner, 1974; Tulin & Cointe, 1988]. Recent reviews of breaking wave studies and the role of breaking waves in air-sea interactions are given by Banner & Peregrine [1993], Banner & Donelan [1991] and Melville [1996].

Due to their energetic and unsteady nature detailed studies of breaking waves are extremely difficult under field conditions. However, insight into processes related to wave breaking has also been gained from controlled breakers in laboratory tanks. The physical consequences of deep water breaking waves established are:

- A significant fraction of the momentum transfer from wind to ocean currents passes through the wave field [Mitsuyasu, 1985]. The air-sea momentum flux τ can be written as the sum of a wave induced component τ_{wave} and a component τ_{turb} due to turbulent fluctuations not correlated with the wave phase [Stewart, 1961].

$$\tau = \tau_{wave} + \tau_{turb} \tag{2.9}$$

Komen *et al.* [1994] summarize that for young waves essentially all momentum flux is supported by waves, and even for fully developed seas the wave contribution is more than 50%. Approximately 95% of the momentum is transferred to the ocean surface layer locally, via wave breaking [Melville, 1996].

- Breaking waves are thought to be a major source of energy dissipation, thus limiting the wave growth and providing the turbulent kinetic energy for mixing in the upper ocean. Phillips [1985] postulated the existence of an equilibrium range where at a given frequency the sum of energy input into the wave field, energy dissipation and wave-wave interactions equals zero and all three components are significant. Under this assumption the spectral rate of energy loss ε is proportional to the cube of the friction velocity and the square of the wave length

$$\varepsilon \propto \frac{u_*^3}{k^2}, \tag{2.10}$$

where k is the wave number. Evidence for wave induced turbulence is found in the dissipation measurements in the surface layer of natural water bodies [Agrawal *et al.*, 1992; Anis & Moum, 1992; Osborn *et al.*, 1992; Anis & Moum, 1995]. More detailed information on wave induced mixing is gained from an extensive laboratory study of breaking waves [Rapp & Melville, 1990]. They found dye to be mixed down to a depth of approximately 10% of the wave length within two wave periods after wave breaking, from where it diffused rather slowly. The dye was confined to a layer of 15% - 20% of the wave length even after 10 wave periods.

- Enhanced air-sea gas transfer rates at wind speeds greater than approximately 10 m/s [Liss & Merlivat, 1986] are attributed to processes relating to breaking waves. Enhanced turbulence levels beneath breaking waves were found to double gas exchange rates in a laboratory tank [Jähne, 1990]. Breaking waves also inject air-bubbles in the upper ocean, thereby effectively increasing the surface area of the air-sea interface. Subsurface motions often draw microbubbles down to several metres depth where they collapse and dissolve due to the increased pressure. Models of bubble-mediated gas transfer are evolving [Woolf & Thorpe, 1991; Keeling, 1993], and enhanced air-sea gas fluxes due to breaking waves are observed in the ocean [Wallace & Wirick, 1992; Farmer *et al.*, 1993].

- Microbubbles generated by wave breaking are exploited as nearly passive tracers in acoustical studies of the upper ocean flow field [Thorpe, 1984], and air entrainment is the major cause of naturally occurring noise in the ocean. Vagle *et al.* [1990] assumed an implicit relationship between wind speed and wave breaking activity and developed an algorithm for estimating wind speeds from ambient noise measurements.

- The ability of small scale breaking to create spikes in the backscatter signal of active microwave sensors not only provides a means for remotely sensing breaking waves but also has to be considered in algorithms for retrieving *e.g.* wind stress from microwave signals.

- Breaking waves not only inject air bubbles into the water but also release water and salt particles into the atmospheric boundary layer. This sea spray may enhance the latent air-sea heat flux [Ling, 1993] and is a source of marine aerosols.

- Furthermore, breaking waves are of great significance to marine engineering due to their ability to inflict serious damage to ships and coastal and offshore structures.

2.3 Langmuir circulation

Langmuir [1938] was the first to analyze systematically the cause of the wind-aligned bands of convergences and divergences on the surface of lakes and the ocean, often manifested by accumulation of flotsam in long narrow streaks. The underlying circulation can be described as pairs of vortices of alternating sign, aligned with the wind direction, with downward flow beneath convergences and upwelling below divergences. The distance between adjacent convergence zones, often labeled the cell spacing, varies from a few metres up to roughly 100 m, whereas the vertical extension, called cell depth, is limited by the mixed layer depth. The structure of individual rolls remains coherent over time periods of order 20 minutes and can be found generally at moderate and high wind speeds. This circulation is now commonly referred to as Langmuir circulation, although the term "windrow" is sometimes found. A review of earlier observations and theories concerning Langmuir circulation is given in Leibovich [1983].

The prevailing theory for the formation of Langmuir circulation is the Craik-Leibovich model [Craik, 1977; Leibovich, 1977], which describes the circulation as an instability caused by the combined action of wind stress and surface waves. A small initial crosswind perturbation of the surface current causes crosswind velocity shears. The vertical vortex lines associated with this shear are tilted by the vertical shear of the Stokes drift of the surface waves, resulting in streamwise vorticity with surface convergence at the maximum of the surface current. Water reaching the surface is accelerated by the action of the wind stress, and downwind currents are greatest near the convergence zone, thus providing a positive feedback.

Nondimensionalization of the governing equations for Langmuir circulation [Leibovich, 1977] yields the dimensional Langmuir number

$$\mathrm{La} = \left(\frac{\nu_T \beta_s}{u_*} \right)^{3/2} \left(\frac{S_0}{u_*} \right)^{-1/2} \qquad (2.11)$$

which represents the ratio of the viscous to inertial forces. In Equation 2.11 ν_T is an eddy viscosity, typically taken as a constant, $2S_0$ is the surface magnitude and $[1/(2\beta_s)]$ the e-folding depth of the Stokes drift, and u_* is the water friction velocity.

In a numerical analysis of the Craik-Leibovich model Li & Garrett [1993] found the maximum downwelling velocity $w_{\max}$ to be proportional to $La^{-1/3}$,

$$w_{\max} = 0.72\, u_* \left(\frac{S_0}{u_*\, \mathrm{La}} \right)^{1/3} \tag{2.12}$$

Thus providing a relationship between downwelling velocities, which can be measured, and eddy viscosity.

In a later paper Li & Garrett [1995] added a buoyancy forcing term and the heat equation to the two-dimensional model so as to derive the temperature field of Langmuir circulation. They also estimated the role of buoyancy forcing in Langmuir circulation. They found the ratio between thermal and wave forcing through Stokes drift can be expressed as the Hoenikker number Ho:

$$\mathrm{Ho} = -\frac{\alpha\, g\, Q\, /\, (c_p\, \rho_w)}{S_0\, \beta_s\, u_*^2} \tag{2.13}$$

where α is the coefficient of thermal expansion, g the gravitational constant, Q the surface heat flux, and c_p, ρ_w are heat capacity and density of sea water, respectively.

For small La the critical value where thermal forcing equals wave forcing is $\mathrm{Ho}_{crit} = 3$ and for $\mathrm{Ho} \ll \mathrm{Ho}_{crit}$ the temperature field is dynamically inactive so that temperature can be regarded as a passive tracer. By fitting their numerical estimates to a scale analysis of the governing equations Li & Garrett [1995] obtained the following expression for the temperature difference of the surface boundary layer between convergence and divergence zone.

$$\delta\tilde{\theta} = C\frac{S_0\,\beta_s\,u_*}{\alpha\,g}\left(\frac{S_0}{u_*}\right)^{-1/3}\ \mathrm{Ho}\,\mathrm{Pr}^{1/2}\,\mathrm{La}^{-1/6}\,. \tag{2.14}$$

Here C is an empirical constant and Pr is the turbulent Prandtl number, defined as the ratio between eddy diffusivity of heat and eddy viscosity. Equation 2.13 yields typical values for the horizontal temperature difference of order 10 mK.

In his pioneering work Langmuir [1938] used fluorescent dye as well as floats made of light bulbs and umbrellas to map the subsurface flow of these large eddies in a lake. D'Asaro & Dairiki [1996] deployed neutrally buoyant floats in a wind driven sea, which revealed eddy overturn times of order of 10 minutes and maximum downwelling velocities of 0.12 m/s. Weller & Price [1988], deploying fixed depth and profiling current meters from the research platform Flip, detected downward velocities beneath surface convergences up to 0.2 m/s.

Since microscopic air bubbles, generated by breaking waves, have a lifetime of several minutes and relatively small rise speeds, they are drawn into the convergence zones, where they accumulate and generate elongated bubble clouds persistent for several minutes [Thorpe, 1992]. These subsurface bands of microbubbles can be detected acoustically [Thorpe & Hall, 1983; Thorpe, 1985; Zedel & Farmer, 1991], and parameters like cell spacing, persistence and velocity are inferred. (See also section 3.2.2).

Images of these bubble clouds confirm the predominantly 2-dimensional nature of Langmuir circulation. However, evidence of cell merging, Y-junctions and shorter bands embedded within the dominant bands [Thorpe, 1992b; Farmer & Li, 1995] point toward processes in the downwind dimension. This is addressed in 3-dimensional large eddy simulation models (LES), now being applied to the ocean surface layer, including Langmuir circulation [Skyllingstad & Denbo, 1995; McWilliams, *et al.*, 1996]. The turbulent field is separated into large scale flows, which are resolved explicitly, and small scale flows, which have to be parameterized. These models are capable of producing amalgamation of convergence zones as well as coexistence of several length scales, similar to the structures observed.

2.4 Energetics of the ocean surface layer

In a steady wall-bounded layer the input of turbulent kinetic energy due to shear production is balanced by its dissipation ε and it follows:

$$\varepsilon = \frac{u_*^3}{k\,z} \tag{2.15}$$

Dissipation of turbulent kinetic energy close to the surface is of great importance to many physical and biochemical processes, such as air-sea gas exchange, mixing of near surface waters and distribution of nutrients and pollutants, and the structure of near surface dissipation has been subject of several investigations. Soloviev *et al.*, [1988] made turbulence measurements with a vertically profiling shear probe in the Atlantic at wind speeds between 2 m/s and 6.5 m/s and found good agreement with the dissipation profile in a wall bounded layer. Drift current measurements by Churchill & Csanady [1983] in the coastal zone of Lake Huron and Cape Cod Bay at wind speeds between 3 m/s and 8 m/s showed roughly a logarithmic velocity profile, which is characteristic for a turbulent flow near a solid wall. On the other hand, the existence of a free surface allows for wave induced velocities, usually much larger than the turbulent velocities, and the breaking of surface waves injects a sudden burst of kinetic turbulent energy and momentum [Donelan, 1990]. Hence, the classical wall layer might not be applicable to the ocean near surface layer at moderate or high wind speed. Long-term velocity measurements from a tower in Lake Ontario gave highly intermittent energy dissipation rates much greater than the expected wall layer estimate given in Equation 2.15 [Drennan *et al.*, 1992, Agrawal *et al.*, 1992]. During an eighty minute record at a wind speed of 12 m/s they observed about 30 events with $\varepsilon k z / u_*^3 > 20$, the maximum being above 100. Between these bursts the dissipation level is consistent with the wall-layer estimate. Anis & Moum [1992], analyzing 366 profiling measurements in the subtropical Pacific under convective conditions and with wind speeds varying from 7 m/s to 9 m/s, found dissipation rates above approximately 15 m depth to be several times higher than can be explained by shear stress and buoyancy. Measurements shallower than 6.5 m had to be omitted due to possible contamination by the ship's wake. Further evidence for enhanced turbulence levels is found in the short record of a turbulence sensor mounted on a submarine at a wind speed of approximately 8 m/s [Osborn *et al.*, 1992], which indicates dissipation rates exceeding wall layer dissipation by over one order of magnitude in the top part of the mixed layer. As pointed out by Agrawal *et al.*, [1992] short term measurements or vertical profilers might not be able to resolve the intermittent energy bursts and therefore bias the estimate of the total dissipation.

Drennan *et al.*, [1992] as well as Anis & Moum [1992, 1995] concluded that a shallow surface layer of enhanced turbulence exists, which is directly influenced by (breaking) waves. Below this layer wall-layer scaling may apply. However, in the presence of coherent motions advection is likely to alter the turbulence field.

Based on the Lake Ontario measurements Terray *et al.*, [1996] proposed a scaling of the dissipation rate dependent on wind and wave parameters. Close to the surface the scaling gives nearly constant dissipation about one order of magnitude larger than predicted by wall layer theory. At a depth of one significant wave height dissipation starts to decay as z^{-2} and approaches wall layer scaling at a sufficient depth, which depends on the energy flux from breaking and on wind stress. Two assumptions are included in this scaling: the depth integrated dissipation being equal to the energy input from the wind and the wave stirred region scales with the significant wave height. The energy input from the wind into the waves was defined as the integral of the temporal wave growth rate:

$$F = g\int \frac{\partial S}{\partial t}\, d\omega\, d\theta = g\int \beta S\, d\omega\, d\theta \tag{2.16}$$

where $S(\omega, \theta)$ is the directional wave height spectrum and β the temporal growth rate of wave energy in the absence of nonlinear interactions and dissipation.

However, for long fetches wave energy divergence could be as large as 50% of the local energy input [Richman & Garrett, 1977] resulting in a smaller wave growths. Hence, Equation 2.16 may underestimate the total wave energy input significantly.

A different approach to estimate the energy input from wind into waves is taken by Gemmrich *et al.*, [1994]. As pointed out by Stewart [1961] the rate of energy input is equal to the wind stress across the air-sea interface times a speed:

$$F = \tau_W \bar{c}_p + \tau_s U_s \tag{2.17}$$

where τ_W, τ_s are the components of momentum flux supported by waves and skin friction, respectively, $\bar{c}_p$ is an effective phase speed of waves acquiring energy and U_s is the surface drift. The primary energy balance of the ocean mixed layer is between the energy input by the wind and dissipation integrated over the depth H of the mixed layer:

$$F = \int_0^H \varepsilon \, dz \tag{2.18}$$

For a fully rough flow ($U_{10} > 7.5 \text{ m/s}$) all air-sea momentum transfer is supported by surface waves [Kinsman, 1965, Donelan, 1990]. Hence, (2.17) reduces to

$$F = \rho u_*^2 \bar{c}_p \tag{2.19}$$

and (2.18) and (2.19) will lead to

$$\bar{c}_p = \frac{\int \varepsilon \, dz}{\rho u_*^2} \tag{2.20}$$

Utilizing dissipation profiles by Anis & Moum [1992], Osborn *et al.*, [1992] and Drennan *et al.*, [1992] Gemmrich *et al.*, [1994] estimated $\bar{c}_p$ in the range of 0.55 m/s to 0.72 m/s - a value which seems to be rather independent of wind speed and wave parameters.

Considering the underestimation of the energy input F due to the neglect of the buoyancy flux, the divergence of surface and internal wave energy fluxes and the local change of wave energy and mechanical energy of the surface mixed layer increases the range of the effective phase speed to 0.1 m/s - 1.0 m/s.

3. Measurement approach

The upper few metres of the ocean during a storm are a rather hostile environment for *in situ* measurements. Waves not only exert great forces on any instrument platform, but also displace the free surface by several metres within seconds. Any measuring device in this environment therefore has to be sturdy enough to withstand the wave forces, but small enough to follow the surface and not to disturb the flow.

During the course of this study a surface drifter capable of measuring the small-scale near surface temperature field and air-entrainment within breaking waves has been developed within the Ocean Acoustics Group, led by Dr. D. M. Farmer, at the Institute of Ocean Sciences.

This instrument played the central role in data acquisition for this project, and a description of it is given in the following section. Some details on calibration and testing are given in Appendix A.

Due to the complex nature of the ocean surface layer any study of a single process occurring within this layer requires knowledge of atmospheric and oceanic forcing. The observations methods this project directly relies on are briefly described in section 3.2.

3.1 An instrument for monitoring breaking waves and near surface thermal structures

The basic mechanical design consists of a vertical sensor boom supported by two surface floats approximately 1 m to each side and hinged via two horizontal arms to an electronics housing, which is supported by a separate float. A schematic drawing of the instrument is given in Figure 3.1. The hinged connection allows all sensors on the lightweight boom to stay at a constant depth in all but very steep surface slopes. In order to avoid interference with the surface structure to be measured, the floatations of the sensor boom are positioned approximately 1 m to the side of the boom and are wedge shaped. A subsurface drogue attached via a 35 m line at the sensor side of the instrument ensure the sensors point into the wind and minimizes flow disturbance caused by the instrument. It further reduces drift which for an instrument floating at the surface can be substantial during periods of high wind speed.

Although modifications and additions to the instrument were made before each experiment the basic design remained unchanged and following sensors were attached:

- Four conductivity cell/thermistor assemblies were mounted at varying depths between 0.17 m and 1.8 m. The conductivity cells consist of four parallel electrodes. A constant current ($I_{rms} = 50$ mA, $f = 45$ kHz) is supplied at the outer pair. The voltage drop across the inner two electrodes, which is a function of conductivity of the surrounding medium, is the signal which gets recorded. The sensitive measuring volume is approximately a sphere of diameter 0.18 m.

Rapid temperature fluctuations within breaking waves require fast thermistor response, which unfortunately is combined with fragile design. Thermometrics FP07 thermistors (7 ms response time in water) embedded in an aluminum housing and guarded by a screen provide satisfactory performance.

A separate thermistor at 0.2 m above the sea surface monitors air temperature.

- Two video cameras, one looking from the bottom of the electronics case towards the upper half of the sensor boom, the other giving an aerial view of the upper arm and floatation, were operating during the November 1991 experiment. The video recordings were used to verify the surface following properties of the sensor array and to confirm the interpretation of high void fractions as breaking waves.
- A Lucas Accustar II dual axis clinometer and a fluxgate compass were placed within the electronics case.
- A solid state accelerometer (Lucas NovaSensor) was mounted on the sensor boom. (It was not present during the November 1991 experiment).
- During the December 1993 and April 1995 experiment an acoustic 3-axis current meter (NE Sensortec UCM40 MkII) had been attached at 0.62 m and 0.45 m depth respectively, approximately 0.24 m to the side of the sensor boom.
- Modifications for the April 1995 experiment replaced the pipe-shaped sensor boom with an aluminum I-beam. Along this beam a thermistor mounted on a small cart was traveling through the water column driven by a precise stepper motor. The profiling

distance was from 1.8 m depth to 0.2 m above the air-sea interface at a speed of 0.5 m/s and a period of 60 s.

- Further, a capacitance wire gauge (Richard Brancker Research LTD., Model WG-30) had been added for accurate surface detection. (See Appendix A).
- A SeaBird SBE3 thermistor was mounted at 1.8 m depth during the April 1995 experiment.

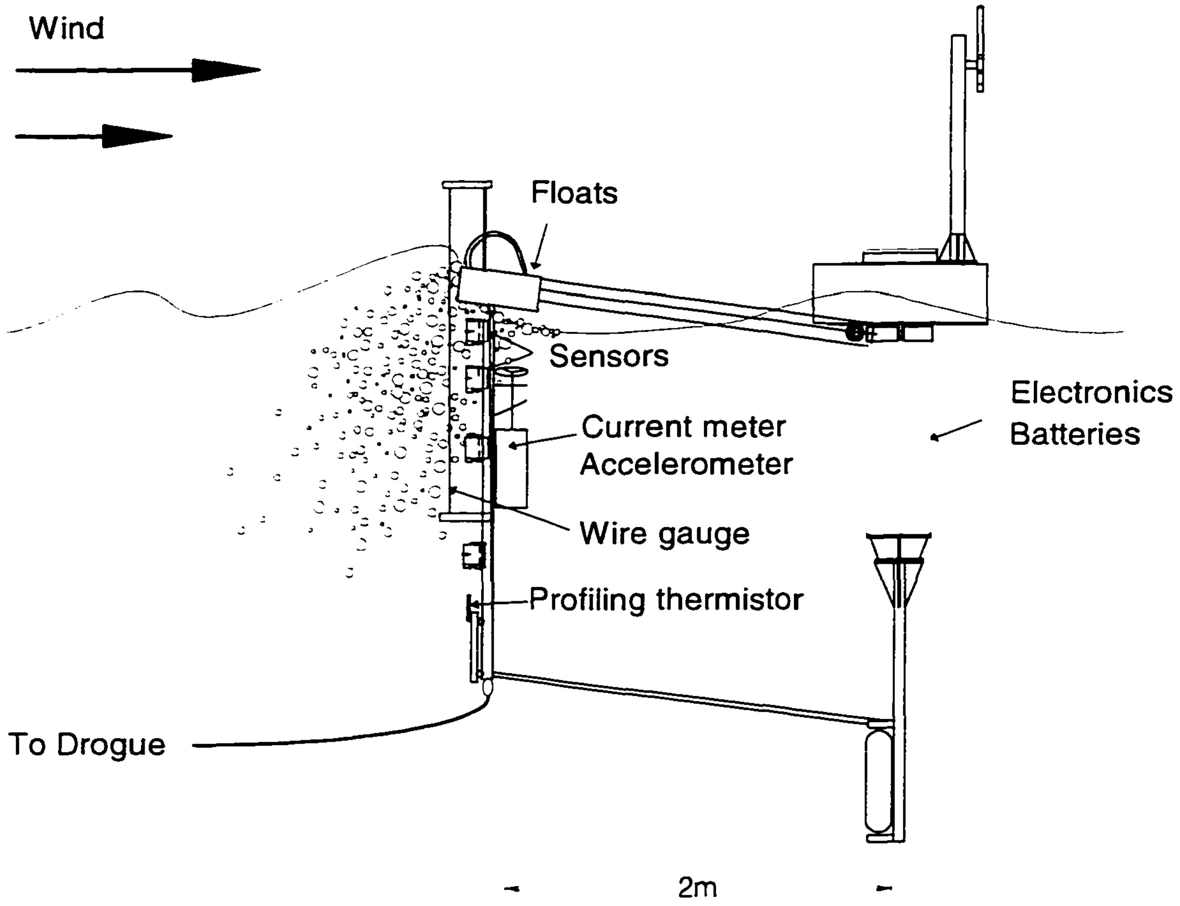

Figure 3.1: Self contained instrument for measurement of breaking waves and surface layer thermal processes. (Version used in April 1995 experiment)

Conductivity, temperature and surface height are sampled at 343.75 Hz (687.5 Hz during the November 1991 experiment). The sampling rate for current meter, tilt meter, compass and accelerometer is 10 Hz and the SeaBird thermistor is sampled at 2 Hz. All data are stored on video tape as 16 bit numbers, where the two least significant bits are occupied for synchronization. The signal enhancement scheme developed by Mudge & Lueck [1994] is applied to the conductivity and the temperature measurements (excluding the SeaBird sensor). The given deconvolution of the combination of the signal and its scaled derivative, which are both recorded separately, reduces the quantization noise and enhances the resolution of short term fluctuations above the software imposed limitation of 1 mK. A summary of specifications for the individual sensors can be found in Table 3.1.

Sensor	Range	Accuracy	Resolution	Sampling rate
Conductivity cell	0.5 S/m to 4 S/m	2.3 mS/m	1.3 mS/m	343.75 Hz *
Thermistor	2°C to 25°C	2 mK	1 mK	343.75 Hz *
Thermistor (SeaBird)	-5 °C to 35 °C	2 mK	1 mK	2 Hz
Current meter	-3.0 m/s to +3.0 m/s	5 mm/s	1 mm/s	10 Hz
Accelerometer	-2.0g to +2.0g	0.01g	0.002g	343.75 Hz $^+$
Clinometer	-20° to +20°	0.2°	0.2°	10 Hz
Compass	0° to 360°	5°	5°	10 Hz
Surface detector	-0.5m to 0.5m	2 mm	0.1 mm	343.75 Hz *

Table 3.1: Summary of sensor specifications. Sampling rates marked by *, $^+$ are down-sampled in data retrieving software to 34.375 Hz and 10 Hz, respectively

All fast response thermistors and conductivity cells, the capacitance wire gauge, the tilt meter and compass were calibrated prior to each cruise. Details of the calibration procedures are given in Appendix A. Calibrations of the SeaBird thermistor, the current meter and the accelerometer were provided by the manufacturers.

Typically, the instrument is deployed at the beginning of a storm and remotely turned on during periods of interest. A combination of a flashing beacon, a VHF transmitter and ARGOS transmitter assures a safe tracking of the drifter.

3.1.1 Theory of void fraction measurements

Void fraction meters based on the impedance method have been known for a long time in many engineering and physics applications for the investigation of steady and unsteady two-phase flows [see e.g. Bernier, 1982]. However, their use in geophysical fluid dynamics is a novelty and the test deployment of a void fraction sensor by Lamarre & Melville [1992] is probably the only oceanographic application of this method published so far.

Several analytical expressions relating the effective conductivity of a suspension of solid particles or bubbles to the volumetric fraction occupied by the particles have been developed during the last century. Basically, the disturbance of a homogeneous electric field by a small sphere of different conductivity is evaluated and the contributions of many such disturbing spheres are integrated. The modified potential determines the effective conductivity of the suspension. An overview is given by Olsen [1967]. For the case of air bubbles (zero conductivity) the solution gets slightly simplified. Upon recommendation of Ninnis [1991] we will apply the following model:

$$\frac{\sigma_e}{\sigma_0} = 1 - \frac{3\Phi}{2+\Phi^2} \tag{3.1}$$

where σ_e is the effective conductivity of the air-water mixture, σ_0 the conductivity of the sea water and Φ the volume fraction of the air. The solution for the air fraction is then given by:

$$\Phi = \frac{3-\sqrt{9-8\eta^2}}{2\eta}, \qquad \eta = 1 - \frac{\sigma_e}{\sigma_0} \tag{3.2}$$

The total impedance across two electrodes immersed in salt water consists of a resistive and a capacitive component, which can be thought of as being in parallel. For the case of sea water an excitation frequency of 50 kHz is low enough that the resistance dominates the probe response, but high enough to prevent polarization.

As seen in equation (3.2) void fraction is a function only of the ratio between the conductivity of the undisturbed sea water and the conductivity of the mixture when air bubbles are present, i.e. between and during breaking waves. This means that no calibration of absolute values is necessary. In laboratory tests Ninnis [1991] found good agreement between observed and theoretical values for $\Phi < 0.2$. For large air fractions

($\Phi > 0.6$) the theory breaks down and observations of those large values have to be considered as indication of large air fractions only.

The reference conductivity of seawater σ_0 is given by the measured conductivity between breaking events. However, conductivity increases with increasing temperature and salinity and fluctuations of these parameters introduce an apparent void fraction signal. Expected temperature fluctuations are smaller than ±2 K and within this range conductivity is a linear function of temperature, which results in an apparent void fraction of 1.7% for a temperature change of 1K. Temperature is measured next to each conductivity cell and the temperature effect is corrected for in the data processing. Similarly, salinity changes of 1 psu give an apparent void fraction of 1.8%. However, no significant salinity fluctuations with periods comparable to the breaking frequency (of order 30 s) are expected, and hence the salinity effect on void fraction is neglected. Low frequency salinity fluctuations are accounted for in the determination of the background conductivity σ_0.

3.2 Ancillary measurements

Interpretation of near surface temperature and conductivity data rely on the knowledge of the environmental conditions, in particular the wind and wave field and the air-sea heat flux. Measurement and processing methods of these quantities will be summarized in the following. Further, modulations of the temperature field by Langmuir circulation form a significant part of this project. Therefore, the acoustical platform used for monitoring these circulations will also be described briefly.

3.2.1 Meteorological observations

Standard meteorological observations during most experiments included in this thesis were made with a Coastal Climate Company MiniMet buoy, the exception being the Marine Boundary Layer experiment when meteorological data were supplied by J. Edson (Woods Hole Oceanographic Institute).

The MiniMet buoy is freely floating, restricted only by a sub-surface drogue to stay in the vicinity of the experiment. Measurement specifications are summarized in Table 3.2. The height of the measurements is 3 m above the water surface and 0.4 m below for the water temperature.

Adjustment of the wind speed from the measurement height to a standard height of 10 m is performed according to Smith [1981a]. This method accounts for stability effects and changes of surface roughness with increasing wind speed.

Quantity	Accuracy	Resolution
Wind speed	(see text)	0.1 m/s
Wind direction	2°	1°
Air / water temperature	0.1 K	0.1 K
Air pressure	0.5 hPa	0.1 hPa

Table 3.2: Specifications of MiniMet buoy measurements

Furthermore, two processes occurring under strong winds cause underestimation of the wind speed. First, strong winds tend to tilt the buoy somewhat, resulting in an angle between horizontal wind and anemometer and second, large waves, (significant wave heights of up to 6 m were encountered during one experiment), shelter the anemometer. The error arising through these effects is unknown, but a significant underestimation of wind speeds above roughly 15 m/s is anticipated.

Sensible and latent heat flux (see Equation 2.2) as well as the flux of horizontal momentum τ are calculated from the bulk aerodynamical formulae [see *e.g.* Krauss & Businger, 1994]:

$$\begin{aligned} LE &= -\rho_a\, L\, C_E\, (q_{10} - q_s)\, u_{10} \\ H &= -\rho_a\, c_{pa}\, C_H\, (T_{10} - T_s)\, u_{10} \\ \tau &= \rho_a\, C_D\, u_{10}^2 \end{aligned} \tag{3.3}$$

where ρ_a is the density of air, c_{pa} the specific heat of air at constant pressure, u_{10} the wind speed at 10 m height, L the heat of vaporization, q_{10} the specific humidity at measurement height, q_s the saturation specific humidity at sea surface temperature, C_D is the drag coefficient and C_H, C_E are exchange coefficients for sensible and latent heat, respectively. The friction velocity u_* is obtained from

$$u_* = \sqrt{\frac{\tau}{\rho}} \tag{3.4}$$

Values for C_D, C_H and C_E are taken from the table of Smith [1981b]. Specific humidities are based on hourly wetbulb temperature measurements aboard the research vessel at approximately 10 m height, which are converted following the standard procedure [see *e.g.* Liljequist & Cehak, 1984].

For the December 1993 experiment radiative fluxes are measured with a pair of Aanderaa solar radiation sensor (sensitivity: 0.3 μm to 2.5 μm) and net radiation sensor (sensitivity: 0.3 μm to 60 μm) mounted on the upper deck of the vessel. Net radiation includes direct and scatter solar radiation as well as thermal radiation from the ocean and the atmosphere. Furthermore, the sensor itself is a black body and emits infrared radiation proportional to its temperature. Hence, the net infrared radiation of the water body *IR* is given by

$$IR = \varepsilon \sigma T_w^4 - \sigma T_a^4 - NR + SW \tag{3.5}$$

where σ is the Stefan-Boltzmann constant, T_a and T_w are air and sea surface temperature, respectively, $\varepsilon = 0.96$ is the emissivity of the ocean surface, *NR* is the measured net radiation and *SW* the measured solar radiation. The first term on the right of Equation 3.5 represents the outgoing radiation of the surface, whereas the second is the thermal radiation of the sensor itself. The albedo of the ocean surface is taken to be constant at $\alpha = 0.06$. For most applications in this thesis the heat budget of the thermal boundary layer above the shallowest sensor is of interest and the fraction of absorbed solar radiation is taken as 0.49, which for pure water corresponds to an absorption depth of 0.17 m [see *e.g.* Hasse, 1971].

3.2.2 Acoustical observation of bubble clouds

Probing the ocean near surface layer by acoustical methods has been for several years a key project of the Ocean Acoustics Group, led by Dr. D. Farmer, at the Institute of Ocean Sciences. Microscopic air bubbles (radii 10μm to 200μm) , predominantly generated by breaking waves [Thorpe, 1992], can serve as excellent tracers for monitoring Langmuir circulation. Due to their resonant characteristics, these micro-bubbles are strong scatterers of acoustic energy and are readily detectable at air fractions as low as 10^{-8}.

The main instrument for these acoustical observations is the SeaScan II instrument platform. It is designed to operate autonomously, suspended from a surface float at roughly 25 m depth. It is equipped with six upward looking sonars (29 kHz to 397 kHz) and two steerable fan beam sidescan sonars (100 kHz), each one rotating 180° within 38 s. Modifications of the instrument prior to the Marine Boundary Layer experiment included the addition of two more sidescan sonars, each of them now rotating 90° within 30 s. The main axis of the sidescan sonars is inclined by 15° (up), thereby scanning the near surface layer within a circular field of approximately 300 m radius. A detailed description of the instrument can be found in Trevorrow & Teichrob [1994].

The air bubbles are carried by the convergent flow into the downwelling region of Langmuir circulation, where they accumulate and build linear subsurface bands, often called bubble clouds [Zedel & Farmer, 1991]. Whilst rotating sidescan images provide a horizontal image of these bubble clouds, the upward looking sonars reveal their vertical penetration as the instrument drifts across cells. The strongest backscatter occurs at the ocean surface, and hence time series of surface elevation and wave height spectra can be calculated. Furthermore, vertical velocities within the bubble clouds can be inferred from the frequency shift of the signal scattered back from moving bubbles. Similarly, during a mode of operation where the sideward looking sonars are held at a fixed direction, the Doppler velocity reveals wave orbital motions, from which directional wave spectra can be calculated [Trevorrow & Booth, 1995]. If the wave motions are eliminated by appropriate filtering, the horizontal velocities associated with Langmuir circulation can be extracted as well [Farmer *et al.*, 1997].

Retrieval and processing of SeaScan data utilized in this project were carried out by Dr. M. Trevorrow (IOS) and V. Polonichko (IOS, UVic).

During the Marine Boundary Experiment high resolution *in situ* measurements of bubble size distributions in the top few metres of the ocean were obtained by an acoustical resonator [Farmer *et al.*, 1997].

4. Observations

Research on vertical exchange processes in the upper ocean boundary layer has been the focus of several field experiments of the IOS Ocean Acoustics Group in recent years. In the following we present deployment summaries of the surface drifter (section 3.1) for two main experiments. A test deployment and an experiment in which this instrument was utilized for ancillary measurements of wave statistics are also summarized. The main emphasis is to present meteorological and surface wave conditions during these deployments, realizing that oceanographic processes like stratification, mixed layer formation, fronts or horizontal advection, which are very important for gas exchange studies, play a secondary role in wave breaking and observations of near surface turbulence field and its effects on temperature gradients close to the boundary. However, these processes will be taken into account where necessary. Analysis of these observations is subject of chapter 5.

4.1 Test deployment in Georgia Strait, November 1991

An initial test deployment of the instrument was carried out in November 1991 in the coastal water of the Strait of Georgia, BC aboard the research vessel *C.S.S. Parizeau*. The location of the test (124°48'W, 49°48'N) is marked on Figure 4.1. Although this first version of the instrument suffered from a number of limitations and lacked key sensors that were used to provide the primary data sets discussed in this thesis, the results motivated sensor improvements and identified temperature signals associated with breaking waves. This deployment on 24/11/91, 1030h - 1820h, PST also provides breaking wave statistics in a fetch limited (20 km) environment which will be discussed in section 5.1.6. A discussion of the environmental data, reproduced in Figure 4.2, as well as details of the heat flux estimation can be found in Farmer & Gemmrich [1996].

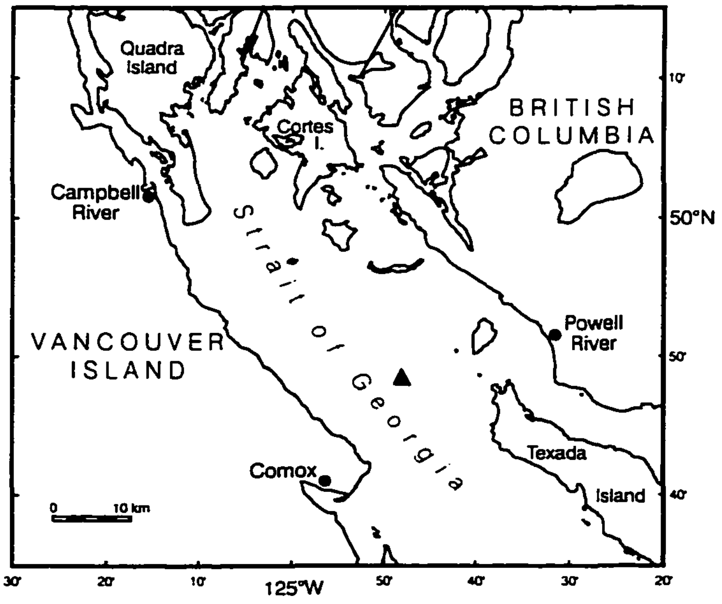

Figure 4.1: Location of the November 1991 test deployment in Georgia Strait (triangle).

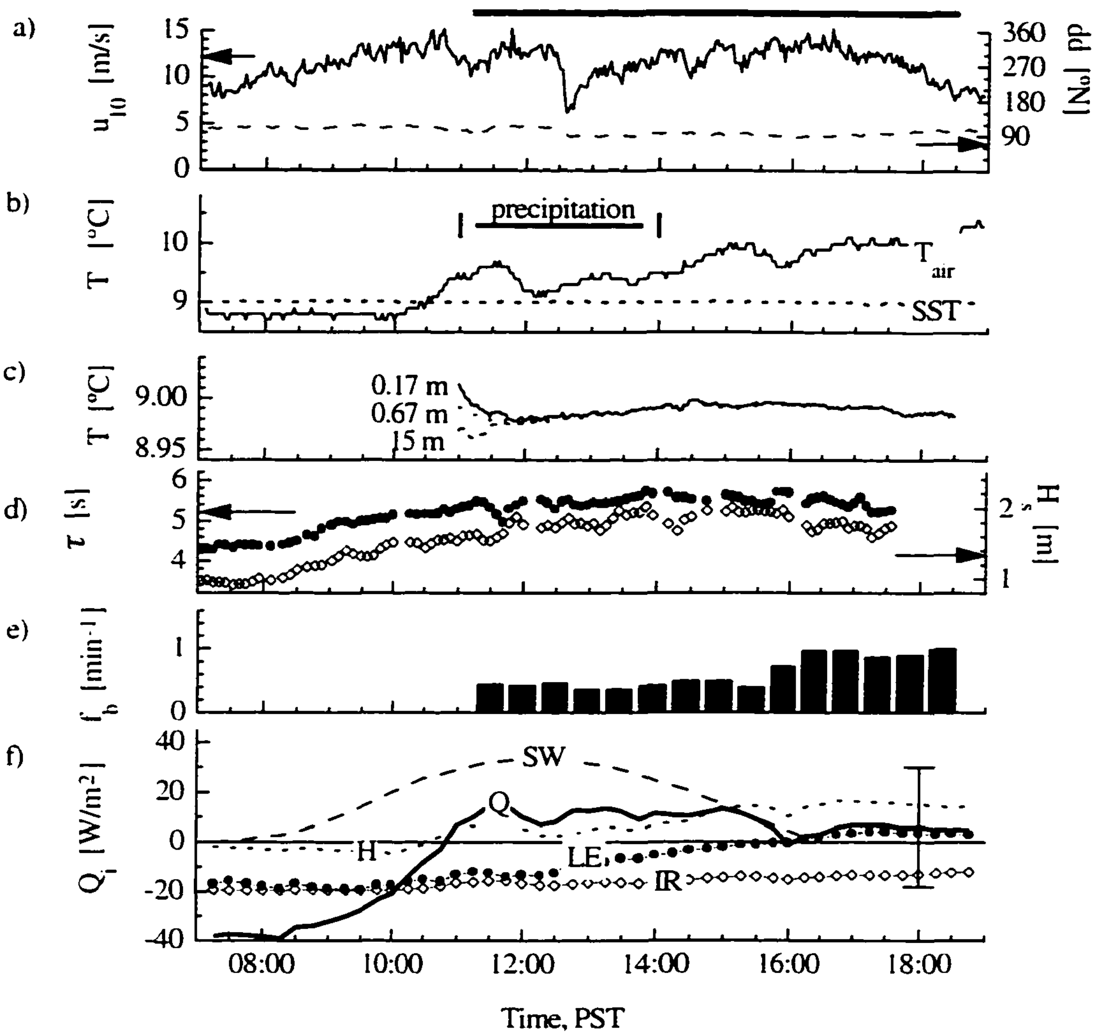

Figure 4.2: Environmental conditions for the Strait of Georgia deployment, 24/11/91. a) Wind speed corrected to 10m and direction. The horizontal bar indicates the duration of the instrument deployment. b) Air temperature T_{air} and water temperature *SST* and time of major precipitation. c) Temperature at 0.17m (solid), 0.67m (dotted) and at 15 m (dashed). d) Dominant wave period τ (solid symbols) and significant wave height H_s (open symbols). e) Breaking wave frequency f_b. f) Components of bulk heat flux Q: latent *LE* and sensible *H* heat fluxes, net infra-red radiation *IR* and fraction of short-wave radiation *SW* absorbed out of the thermal boundary layer.

4.2 CST-7 II experiment, February 1992

CST-7 Phase II (Critical Sea Test 7), a combined air-sea research / ocean acoustic study, took place in the Gulf of Alaska in February / March 1992 [Root & Hanson, 1992]. During this experiment our surface drifter was utilized to monitor the frequency of breaking waves and no temperature measurements were obtained. The research vessel was *CSS John P. Tully*.

A primary goal of the CST-7 programme was to relate acoustic reverberation to environmental conditions, and therefore a comprehensive set of environmental measurements was collected. This includes standard meteorological observations aboard *CSS John P. Tully* and *R/V Cory Chouest*. Processing of the meteorological data was coordinated by J. Hanson (Johns Hopkins University / Applied Physics Laboratory). Directional wave observations with a Datawell WAVEC buoy were carried out and processed by R. Marsden (Royal Roads Military College).

The deployment on 24/02/92 - 26/02/92 of our surface drifter provided the first measurements of breaking frequency in the open ocean. (For discussion see section 5.1). The experiment site at 45°48' N, 150°01' W, more than 500 nautical miles from the nearest coast, provides a fetch unlimited environment for wave development.

The instrument was deployed in light wind from WSW at 24/02/92, 2340h (all times are UTC). As an intense low pressure system moved over the test site from the south the wind shifted towards N and increased steadily until it reached a maximum of 16 m/s at 25/02/92, 2220h. As the centre of the low pressure system passed the test site the wind speed dropped rapidly to 5 m/s within 1½ hours, and the wind direction veered to ESE. The environmental conditions are shown in Figure 4.3.

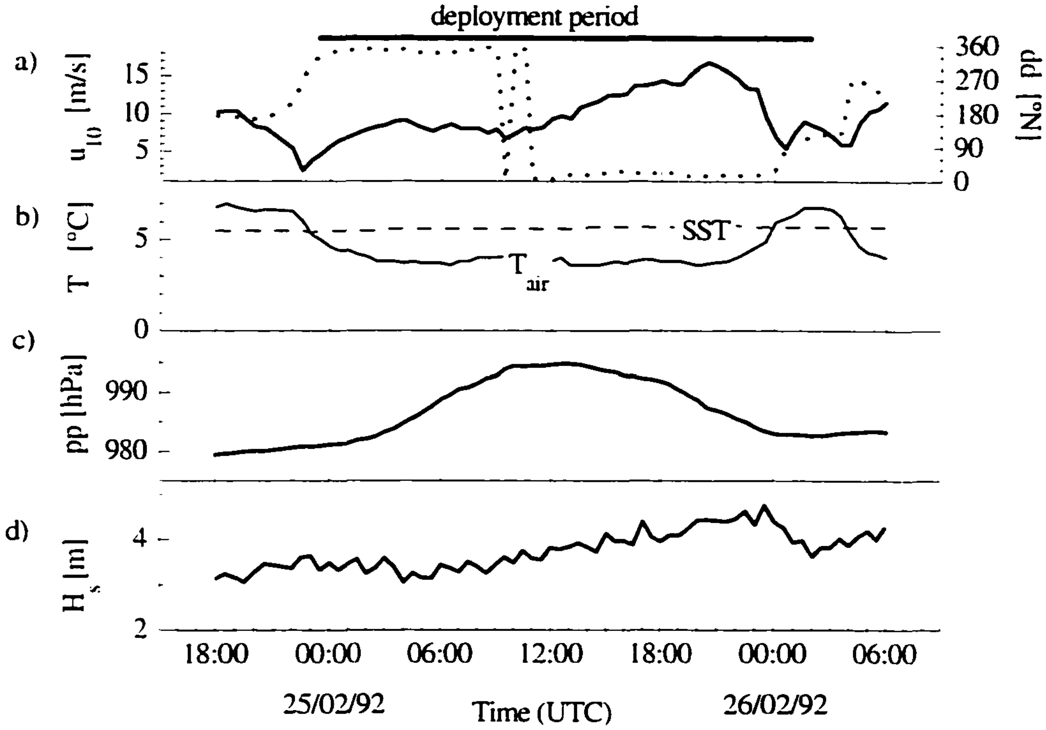

Figure 4.3: Environmental conditions for the Gulf of Alaska deployment, 24/02/92. a) wind speed (solid) corrected to 10 m and direction (dashed), b) air temperature (solid) and sea surface temperature (dashed), c) barometric pressure and d) significant wave height.

The wave field was dominated by the remainder of a previous storm located to the south east of the test site, i.e. waves with 0.09 Hz dominant frequency coming from ESE. As the wind increased, new wind waves developed. According to the prevailing wind direction these waves traveled in a direction approximately opposite to that of the swell. Figure 4.4 shows the directional wave spectrum from the WAVEC buoy at 25/02/92, 2000h. Although the actual spectral density varies during this deployment, this directional characteristics of the wave field shown in Figure 4.4 remain valid throughout the whole period of interest. In summary the wave field can be described as developing wind waves of dominant frequency 0.12 Hz - 0.15 Hz opposing young, decaying swell with frequency 0.09 Hz.

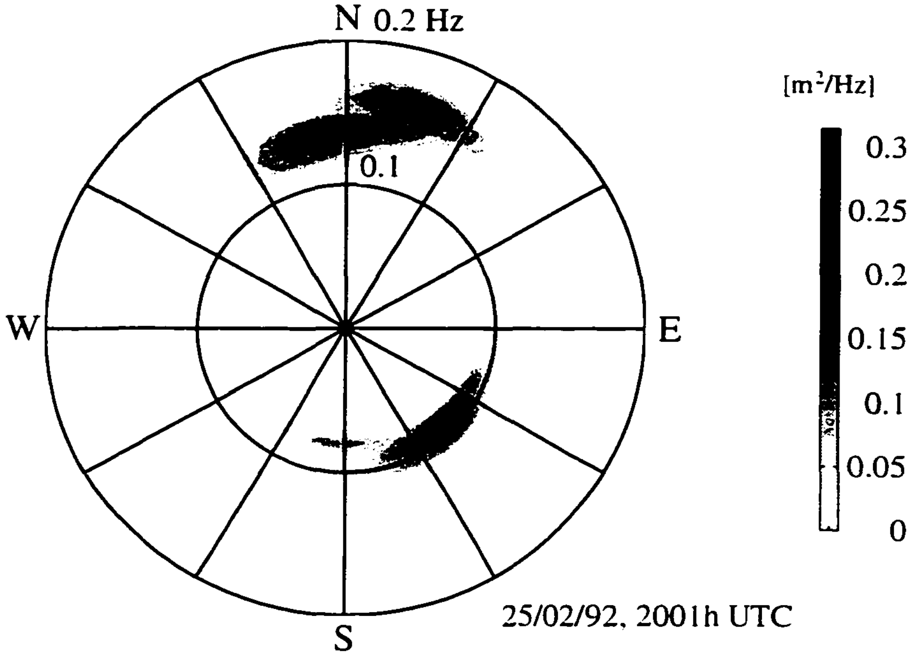

Figure 4.4: Directional wave field at 25/02/92, 2000h (UTC).

4.3 NE Pacific, December 1993

This experiment took place during 29 November to 18 December 1993 off the West Coast of Vancouver Island in the vicinity of 48°57'N and 127°00'W. The research vessel was the *CSS John P. Tully*. The overall theme of the experiment was a study of surface processes at high sea state, such as wave breaking, gas exchange and Langmuir circulation.

A series of low pressure systems passed through the region and high sea states were indeed encountered. Maximum wind speed during this experiment reached hurricane force (Beaufort 11) and a record wave height of 30.8 m was observed in the south entrance of Hecate Strait, just 200 km northwest of the experimental site [Gower & Jones, 1994].

Two deployments of the surface drifter will be discussed in chapter 5 and details of the environmental conditions are given below. Meteorological data were collected with the MiniMet buoy and the WeatherPak radiation package aboard *CSS John P. Tully*. (see section 3.2.1).

The instrument was deployed at 03/12/93 1330h (all times are local) and was set to record every odd hour until 04/12/93, 0525h. Figure 4.5 summarizes the meteorological and wave conditions. The wind with speeds of 10 m/s - 16 m/s was from the North, allowing for a fetch of approximately 80 km. Heavy rain prevailed for the first four hours of the deployment, but only traces of precipitation were observed after 1800h. The sea remained warmer than the air throughout the whole period. Developing wind waves (Figure 4.6) and existing swell gave a significant wave height increasing from 4 m to 5 m within 12 hours. Strong wind and drier air masses during the night allowed for substantial ocean heat loss, increasing from -50 W/m^2 at noon to -250 W/m^2 during the night.

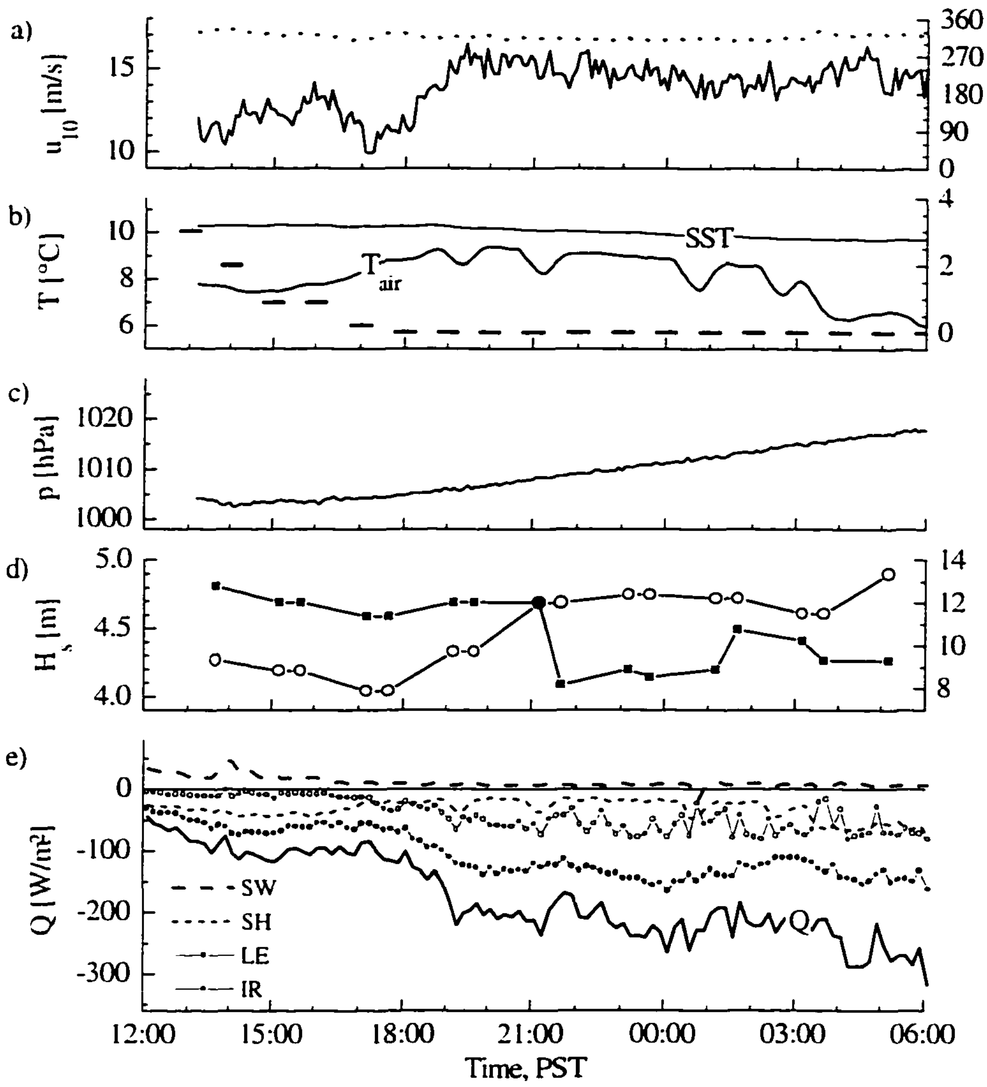

Figure 4.5: Environmental conditions 03/12/93 - 04/12/93. a) wind speed (solid) corrected to 10 m height and wind direction (dashed), b) air temperature , sea surface temperature and precipitation rate (dashes), c) barometric pressure, d) significant wave height (open) and peak wave period (solid), e) air-sea heat flux components: absorbed solar radiation SW (dashed), net infra red radiation IR (open circles), sensible heat flux SH (dots), latent heat flux LE (solid circles) and total heat flux out of the thermal boundary layer Q (solid line).

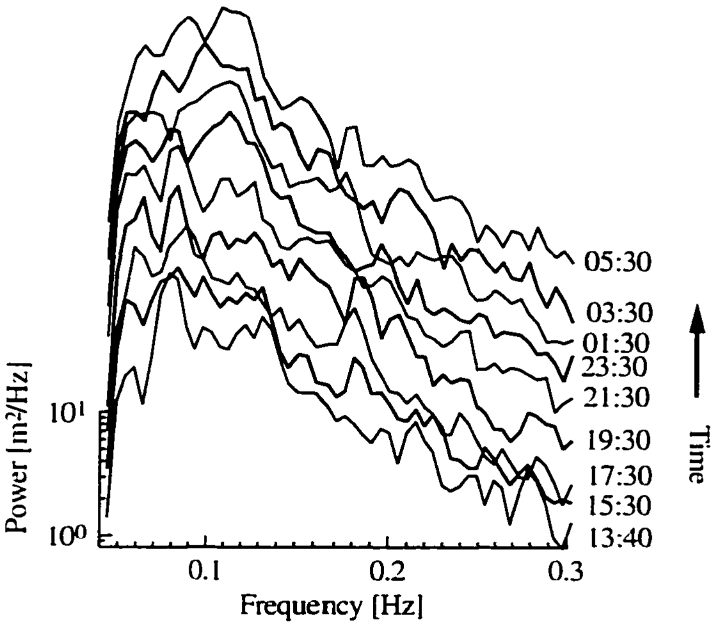

Figure 4.6: Wave height spectra for 03/12/93, 1340h to 04/12/93, 0530h obtained with surface drifter. Spectra are offset by 200%.

The nearby drifting SeaScan provided side-scan sonar images of the near surface bubble field for 1 hour periods at 3 hour intervals. An example of two images is given in Figure 4.7. The images were jointly processed by Dr. M. Trevorrow (IOS) and V. Polonichko (IOS, UVic). Bubble clouds appear black on the image. At 1313h only short, poorly organized structures can be seen, which is a sign of weak Langmuir circulation activity. However, the second image taken at 2135h shows narrow elongated structures aligned with the wind and consistent for more than 100 m. Those bubble clouds were organized by pronounced Langmuir convergences.

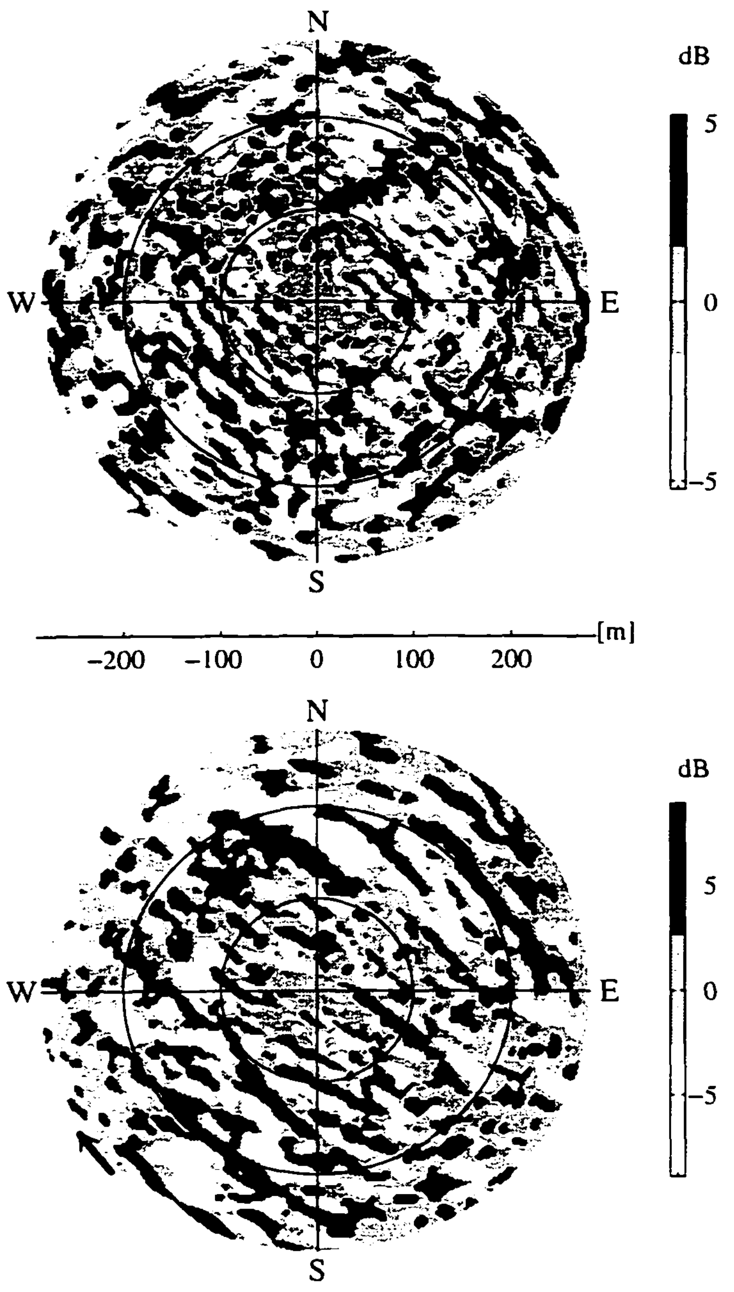

Figure 4.7: Scanning sonar (100 kHz) images showing bubble cloud distribution on 03/12/93 at 1313h (top panel) and 2135h (bottom)

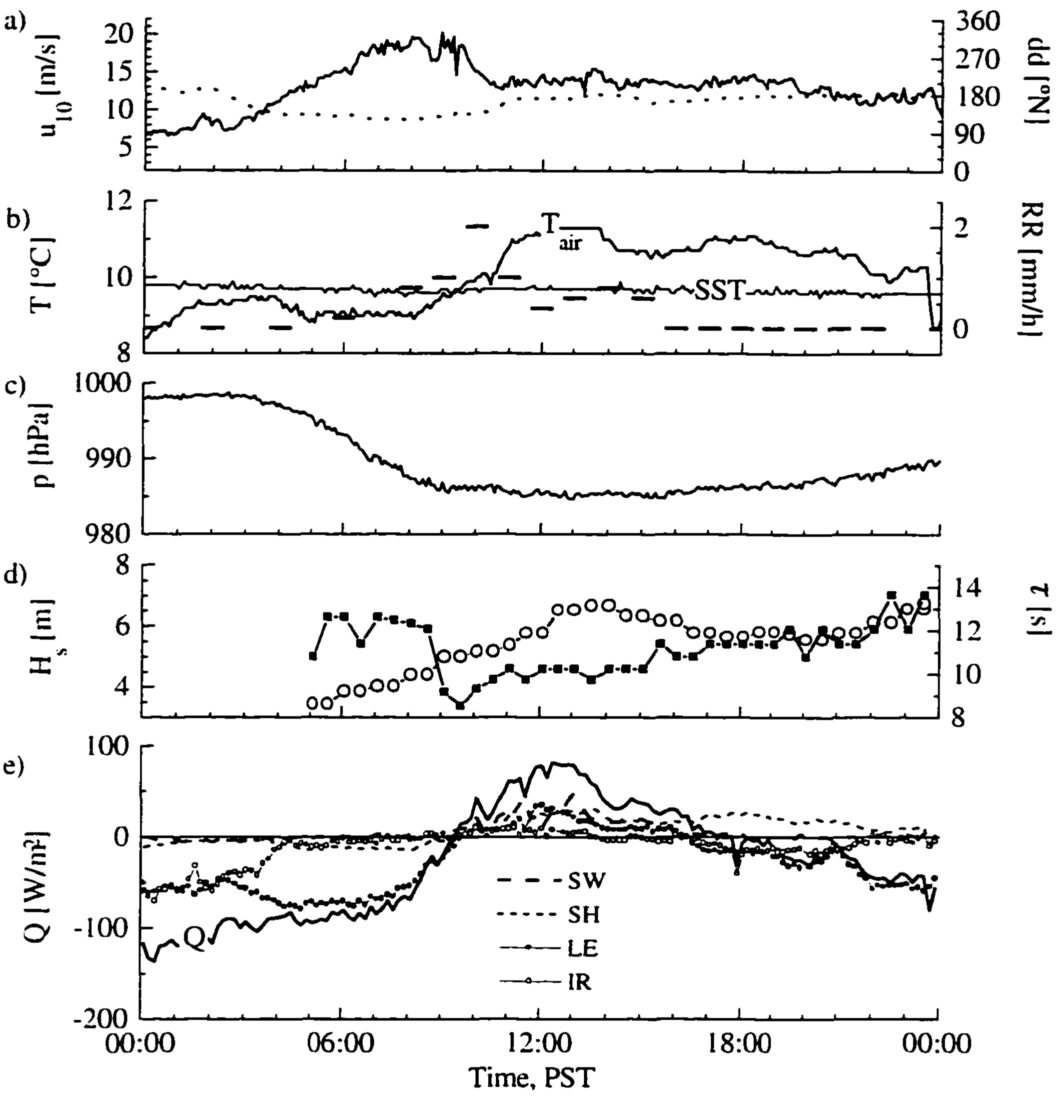

Figure 4.8: Environmental conditions 09/12/93. a) wind speed corrected to 10 m height (solid line) and wind direction (dashed), b) air temperature , sea surface temperature and precipitation rate (dashes), c) barometric pressure, d) significant wave height (open) and peak wave period (solid), e) air-sea heat flux components: absorbed solar radiation SW (dashed), net infra red radiation IR (open circles), sensible heat flux SH (dots), latent heat flux LE (solid circles) and total heat flux out of the thermal boundary layer Q (solid line).

The second deployment on 09/12/93 from 0448h to 2357h covered the peak of a storm with wind speeds up to 20 m/s (Figure 4.8). The low pressure system responsible for this storm was located further to the North and had a centre pressure of 952 hPa. The prevailing wind direction from the South made for unlimited fetch and wind waves were rapidly developing with peak periods growing from 8 s to 12 s. The significant wave height increased from 4 m to 7 m, which made for a very impressive sight, but prohibited the deployment of SeaScan. The air-sea temperature difference changed the sign around 1000h and remained positive until 2330h. Precipitation was observed from 0600h to 1500h with a maximum of 2 mm/h in the late morning. Despite the strong wind the air-sea heat flux was rather small, varying from -100 W/m^2 at night to 80 W/m^2 at noon. Latent heat flux and net infrared radiation offset the ocean heat gain due to the sensible heat flux in the evening, giving rise to an overall heat loss after 1800h. The combination of positive air-sea temperature difference and negative heat flux is worth noticing for its important implications on the analysis of temperature anomalies in breaking waves (section 5.2).

The ARGOS satellite tracked positioning system provides coordinates of the instrument location at irregular intervals, which can be combined to a coarse instrument drift track. This was done for the 09/12/93 deployment. (Figure 4.9). The track resembles an almost complete inertial oscillation with the end point approximately 7 km west of the starting point. Surprisingly, the instrument drifted roughly perpendicular to the wind direction, thus traversing successive Langmuir convergence zones.

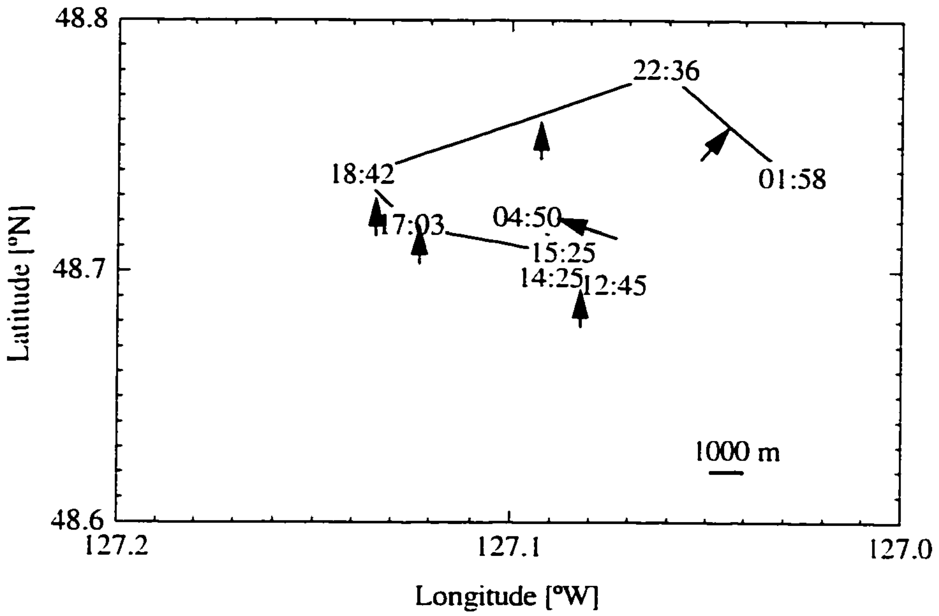

Figure 4.9: ARGOS instrument positions for 09/12/93. Arrows indicate wind direction at given time.

4.4 Marine Boundary Layer (MBL) Experiment, April 1995

During this experiment, which was carried out off Monterey, California in April and May 1995 and provided the primary data set for this thesis, research groups from several institutions in Canada and the United States collaborated to study the atmospheric and oceanographic part of the marine boundary layer. Our participation was from aboard *R/V Wecoma*. In our analysis we will focus on 18 April, when the surface drifter and the acoustic package were operating simultaneously. Meteorological observations were obtained from *R/V Wecoma* and *R/P Flip* and analyzed by J. Edson (Woods Hole Oceanographic Institution).

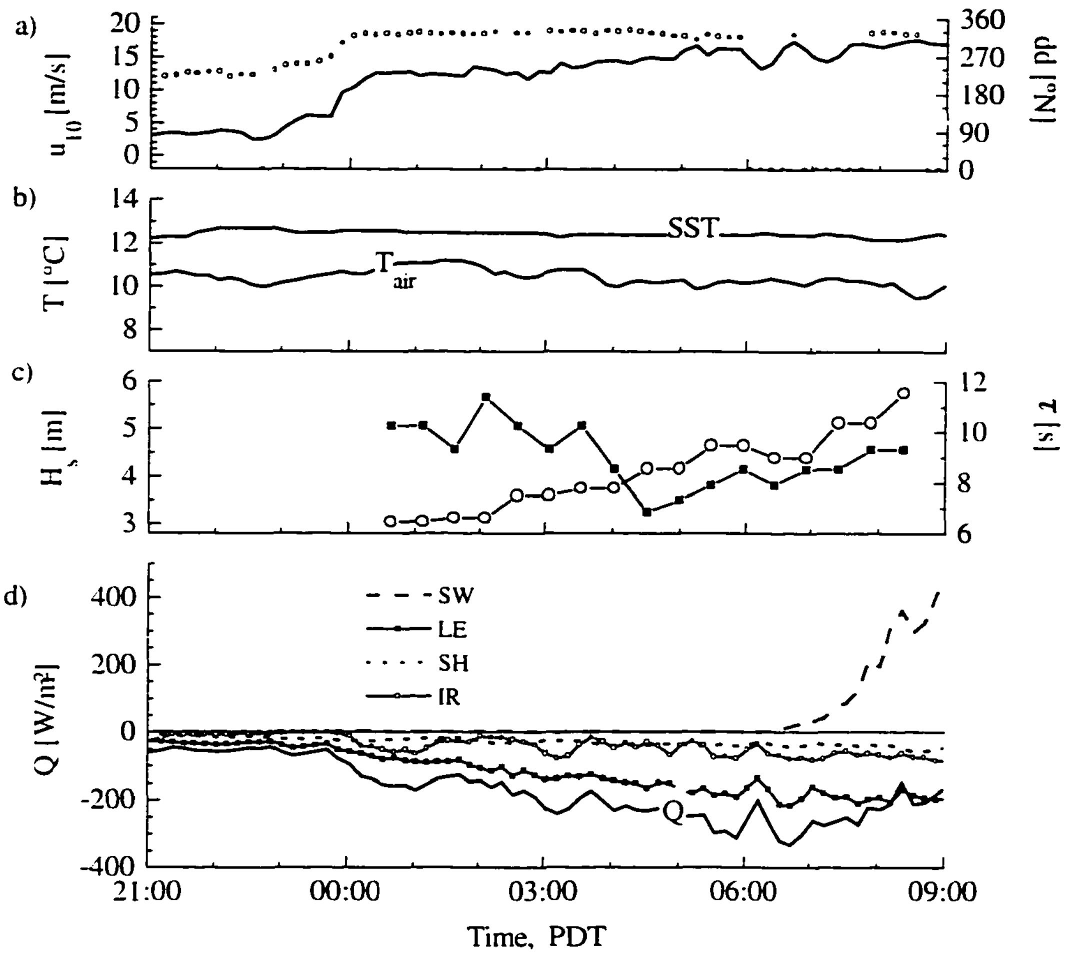

Figure 4.10: Environmental conditions during 18/04/95 deployment. a) wind speed corrected to 10 m height (line) and wind direction (circles), b) air temperature , sea surface temperature, c) significant wave height (open) and peak wave period (solid), d) air-sea heat flux components: total solar radiation SW (dashed), net infra red radiation IR (open circles), sensible heat flux SH (dots), latent heat flux LE (solid circles) and total heat flux out of the thermal boundary layer Q (solid line).

The surface drifter had been modified for improved measurements of the near surface temperature field. The most important modification of the instrument , which provided us with the key data set used in analysis of the turbulent diffusivity, was the addition of an electrically driven temperature sensor. The additional weight affected the surface following properties of the sensor boom slightly, but measurement of the surface location by capacitance wire gauge allowed for depth correction. (See also Appendix A1.3).

The instrument was deployed 18/04/95 0015h (all times are local, *i.e.* PDT), at 36°15'N and 122°26'W and acquired data until 0825h. This data set provides the basis for the modeling approach in Chapter 6. Environmental conditions are given in Figure 4.10.

After a fairly calm day the wind picked up just before the deployment and increased then from 10 m/s to 17 m/s, with steady direction from NNW. The air-sea temperature difference of roughly 2 K remained nearly unchanged throughout the deployment. No precipitation fell on this day. Wind waves were developing under unlimited fetch conditions with significant wave height growing from 3 m to over 5 m. The heat flux within the thermal boundary layer increased from -150 W/m^2 to -350 W/m^2 just before sunrise, mainly by latent heat loss due to evaporation.

The acoustic package SeaScan, floating nearby scanned the near surface bubble field every even hour from 16/04/95, 1200h to 19/04/95, 0244h. Further, a self contained thermistor package (TR-1000, Brancker Research LTD.), which was attached to the SeaScan rubber cord at 6.5 m depth, recorded temperature with 0.2 Hz sampling rate. Data acquired with these instruments are utilized in supporting the interpretation of the near surface temperature field and are discussed in the appropriate sections (*i.e.* sections 5.2.3 and 6.3.3). Due to the presence of a layer of warm surface water Langmuir circulation was inhibited prior to approximately 0100h (Polonichko *et al.*, 1997).

5. Data Analysis

5.1 Wave breaking

In this section we will present the characteristics of breaking waves concerning scale, strength and frequency of breaking. These properties govern the generation of turbulence by injecting the turbulent kinetic energy into the surface layer. First we summarize the detection criterion and the inherent data processing techniques. Further, breaking scale and mean breaking characteristics, which dominate over individual fluctuations and hence provide a general description of the breaking wave, are presented. The relation between the frequency of breaking and the wind and wave field is examined in section 5.1.6.

5.1.1 Detection of breaking waves

The intercomparison of breaking wave field observations are made difficult by the lack of a well-accepted criterion for what constitutes a breaking event. Different measurement techniques rely on varying criteria with somewhat arbitrary thresholds.

Breaking wave criteria can be divided into two classes, the first relating to some characteristics of the surface elevation at a point and the second to observations of air entrainment or whitecaps.

Longuet-Higgins & Smith [1983] defined a breaking event by the occurrence of a sudden jump in the surface elevation measured by a wire gauge. A similar method was applied by Thorpe & Humphries [1980] who used a surface slope criterion in combination with a minimum wave height. A more elaborate detection function relating breaking waves to surface elevation was utilized by Weissman *et al.*. [1984] and Katsaros & Atatürk [1992]. They looked at the spectral energy for various frequency bands of the surface elevation time series recorded in Lake Washington and concluded breaking events generate a characteristic burst in the 18 Hz - 32 Hz band.

The most obvious technique for measuring air entrainment in breaking waves is the visual observation of the sea surface [Toba, 1971, Holthuijsen & Herbers, 1986]. In this category falls also the related field of whitecap coverage observations [Monahan & O'Muirhearataigh, 1986], which however can not be readily compared to point observations.

Air entrainment in breaking waves has also been recognized as a main source of ambient noise in the ocean [Knudsen *et al.*, 1948], which can be monitored remotely. Single point measurements of the ambient noise yield an integral distribution of breaking waves [Farmer & Vagle, 1988], whereas a hydrophone array may enable the tracking of individual breaking events [Ding & Farmer, 1992, 1994].

Similar to Su & Cartmill [1992] and Lamarre & Melville [1992] we define a breaking event by its air entrainment into the top of the water column. While this criterion utilizes a well defined measurable property of all breaking waves except micro-breaking, the definition of a suitable threshold again seems arbitrary. Longuet-Higgins & Turner [1974] modeled a spilling breaker as a turbulent gravity current entraining air while riding down the slope of a wave. Their theory predicts that a density difference greater than 8% is required to sustain a steady motion. We therefore define a breaking event as incidents with air fraction greater than 0.08 at our top sensor. However, we find variation of the threshold between 0.05 and 0.1 alters the amount of detected breaking events by less than 4%. For thresholds below approximately 0.03 foam patches not related to active breaking are also included and significantly more events would be detected.

5.1.2 Surface height data processing

By definition acceleration is equal to the second derivative of the displacement. Therefore, the double integration of the vertical component of the acceleration yields the surface elevation. Pitch Θ and roll Φ of the instrument tilt the measurement axis of the accelerometer relative to the vertical, and a reduced acceleration is measured. The true vertical component of the acceleration is:

$$a = a_{meas} / (\cos\Theta \cos\Phi) \tag{5.1}$$

where a_{meas} is the measured acceleration. However, for a typical deployment like on 03/12/93 the median absolute pitch is < 6° and the median absolute roll is < 5°. This results in a correction of about 1%. Only about 5% of the time the correction is greater than 5%, with a maximum of 9%. The measurement principle of the inclinometer used in our instrument is that gravity acts on the horizontal axis of an accelerometer if it is tilted. Hence, tilt and possible horizontal acceleration would cause an identical signal on the inclinometer and can only be distinguished by their spectral properties. Horizontal accelerations are expected to be of short pulse like nature and are not recorded by the damped accelerometer of the inclinometer. We therefore expect the inclinometer to measure true instrument tilt.

The integration of the acceleration is done in frequency space:

$$\eta(t) = \mathcal{F}^{-1}\left\{H(\omega)\frac{-1}{\omega^2}A(\omega)\right\} \tag{5.2}$$

where η is the surface displacement, H a high pass filter, ω the radian frequency, A the Fourier transform of the vertical component of acceleration and $\mathcal{F}^{1}$ stands for the operation of inverse Fourier transform. This process is extremely sensitive to low frequency noise which has to be filtered. The filter window Γ consists of zeros up to a frequency of 0.045 Hz, unity above 0.05 Hz and a smooth transition (Hanning window) in between. No wave motion is expected at frequencies below 0.05 Hz and this filter assures a rigorous cut off of all instrument noise at lower frequencies.

5.1.3 Air entrainment in breaking waves

In the active part of a breaking wave large amounts of air bubbles are entrained into the top of the water column. Properties of this entrainment such as magnitude, duration and penetration are observed with the array of conductivity cells.

Short data records from the conductivity cells (converted into air fraction) and the capacitance wire gauge starting at 0137h on 18/04/95 are shown in Figure 5.1. The air fraction at 0.12 m nominal depth exhibits several spike-like signals, varying from roughly 1% up to 85%. Three different processes can be associated with these signals.

An active breaking event approximately 10 s after the start of this record (see insert in Figure 5.1) generates air entrainment which reaches a maximum of 44% at the top sensor, and even at the second sensor a signal of 2% air fraction can be detected. At the shallowest sensor the entire signal lasts approximately 0.8 s. At the second sensor the signal onset is delayed by approximately 0.1 s, and rising of the bubbles provide for a shorter duration of air entrainment at greater depth. Note that during 18/04/95 air fractions at the two deepest sensors at 0.36 m and 0.51 m depth, respectively, are too low to be resolved with our system. The sensor depth during this event varies by approximately 50 mm, but the minimum sensor depth of 93 mm ensures that no spurious signal due to surface proximity is present (see Appendix A).

The large air fraction occurring at approximately 26 s after the start of this record, however, is most likely caused by surface proximity of the conductivity cell. The capacitance wire gauge records the height of the water column above the depth of the shallowest sensor of 31 mm. Tests show a significant apparent air fraction to be recorded for surface proximities less than 30 mm (Appendix A). However, the wire gauge and the conductivity cell are separated horizontally by approximately 20 mm, allowing for a possible shallower depth at the conductivity sensor location. We therefore exclude all

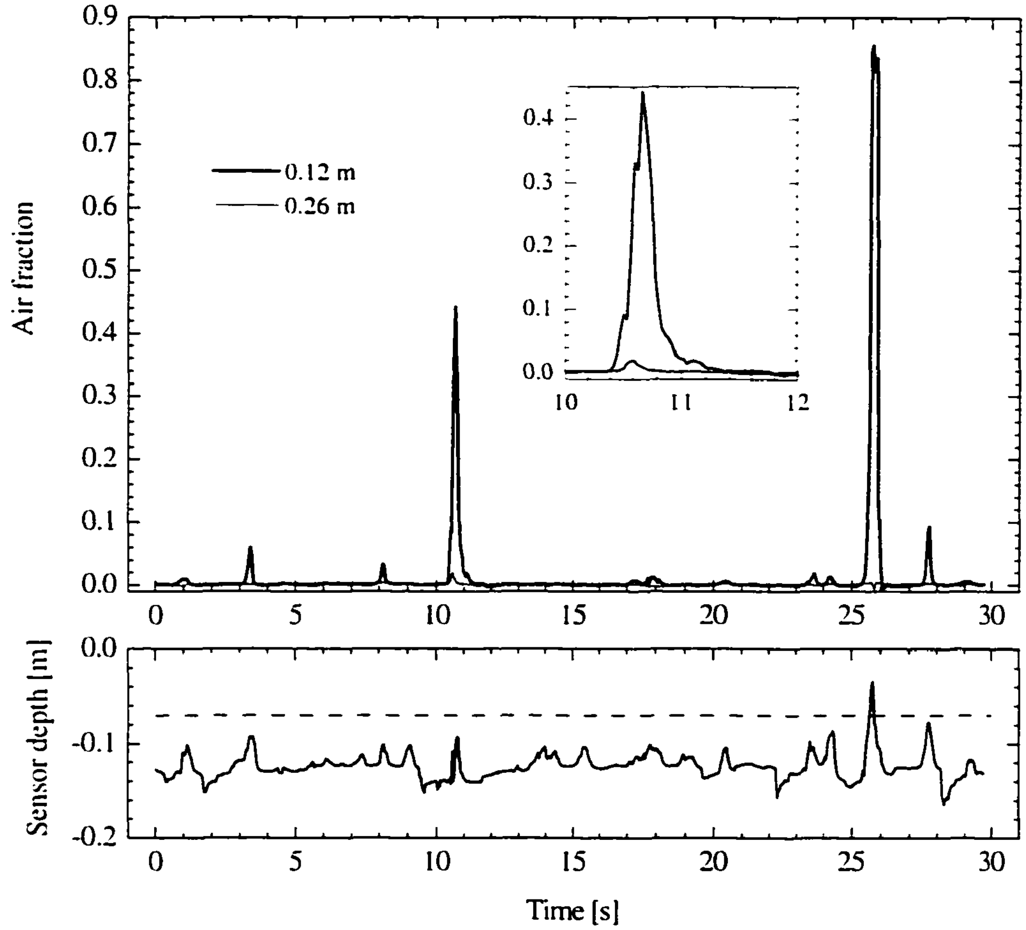

Figure 5.1: Air fraction measured at 0.12 m and 0.26 m (top) and corresponding sensor depth (bottom). The dashed line represents minimum depth to exclude signal bias due to proximity of the conductivity cell to the surface. Start time of the record shown is 0137h, 18/04/95. The first large peak is associated with wave-breaking, but the second is caused by the sensor moving too close to the surface.

conductivity signals during times of less than 70 mm water height, recorded by the capacitance wire gauge, from further data analysis.

Air fraction signals less than 8% at the shallowest sensor are thought to be associated with air entrainment in the vicinity of the sensor which results in a reduced signal.

Detectable air entrainment at depth greater than 0.5 m is most likely an indication of a plunging breaker, which is not very common in deep water. For the open ocean data typically less than 2% of breaking events result in air entrainment which is with our sensors still measurable below 0.25 m.

However, during two deployments a much higher fraction of breaking events with deeper air entrainment was found. In Georgia Strait (24/11/91) more than 8% of the waves can be detected at the second sensor (0.32 m) and 5% at 0.51 m depth. This suggests that the wave field in this fetch limited environment contains a higher fraction of plunging breakers than anticipated under open ocean conditions. During this deployment a dominant wave length of roughly one third and half the significant wave height of typical open ocean waves make for steeper waves which are more likely to plunge down on the steep forward face of the wave. During the 25/02/92 deployment a similarly high percentage of 9.5% of breaking events cause detectable air entrainment at 0.46 m depth and 2% can be detected at 0.75 m depth. This high incidence of deeply penetrating air entrainment is most likely linked to the condition of strongly forced wind waves opposing a swell (Figure 4.4), which will also steepen the waves.

The average time evolution of air entrainment, obtained from all 935 breaking events within the 18/04/95 data set, which show a top sensor depth of at least 0.08m, is given in

Figure 5.2. Normalization of air fraction is done with respect to the maximum value at the top sensor during the event, and time is scaled by the signal duration at this sensor. The signal is nearly symmetrical forming a broad peak lasting about 50% of the whole signal duration with rapid increase and decline. An average residual air fraction of 5% of the maximum value remains present after the rapid drop for at least 50% of the signal duration. At 0.26 m depth the average maximum value drops to less than 4% of the value at 0.12 m and to less than 3% at 0.36 m depth. No air entrainment can be detected at the deepest sensor at 0.51 m.

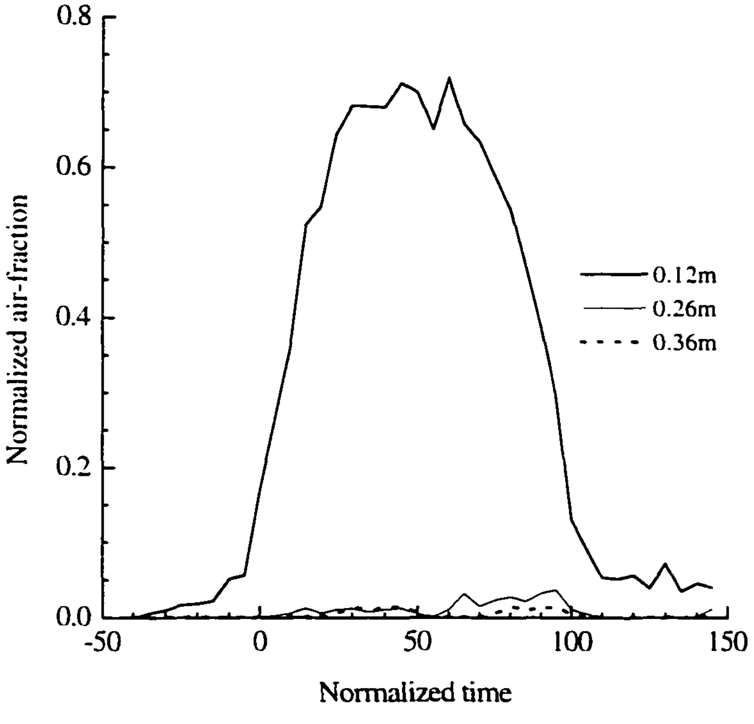

Figure 5.2: Average air fraction normalized by the maximum value at 0.12 m and time scaled by event duration, for all breaking events on 18/04/95.

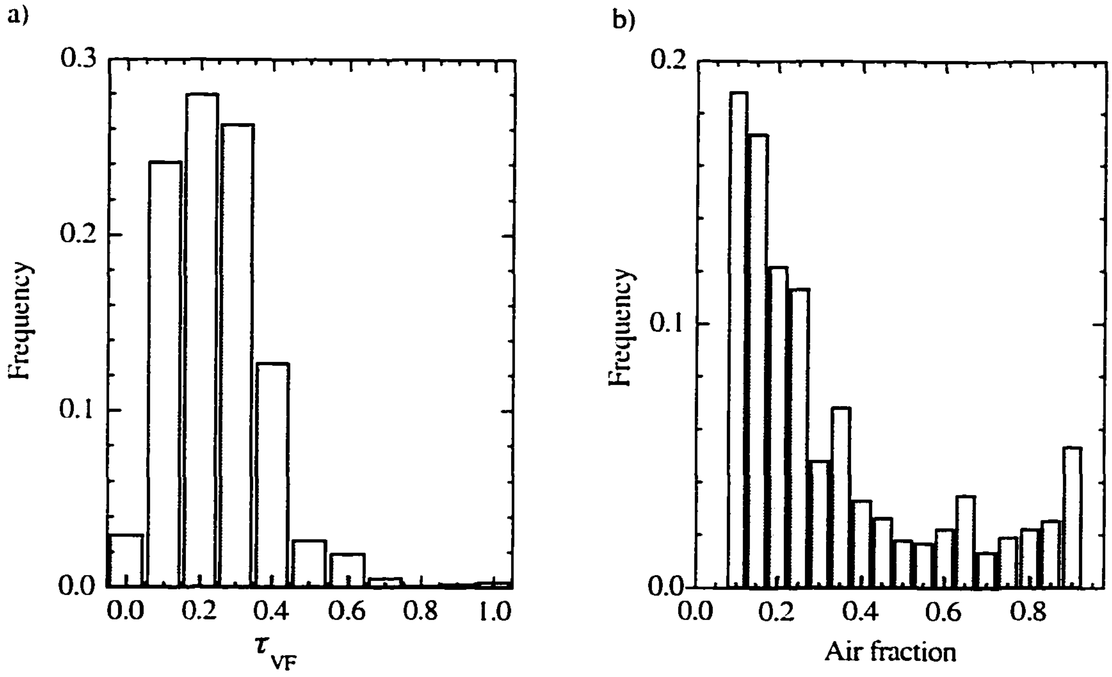

Figure 5.3: Distribution of a) duration of air entrainment and b) maximum air fraction on 18/04/95. Nominal depth is 0.12 m.

As seen above, the initial air entrainment in spilling breakers with air fractions of several percent is a very shallow process. Therefore, at a fixed point the signal duration of large air fractions is very brief. The distribution of the signal duration, *i.e.* the period the air fraction remains above the threshold defining a breaking wave, for 18/04/95 (Figure 5.3a) shows the majority of breaking events last between 0.1 s and 0.4 s. Assuming that the signal results from large air bubbles getting pushed down to the sensor depth and the drop is due to the air bubbles rising out of the field of measurement, the signal duration can be used to estimate an average of the bubble injection and rise speed. Taking the median value of signal duration (0.24 s) and a maximum distance of 0.09 m to the sensor, for the air to be detected (section 3.1) the speed is estimated as roughly 0.75 m/s. However, it should be noted that injection is caused by a downwelling jet, whereas the rise of bubbles is mainly governed by the slower buoyant motion, yielding a downwelling motion greater than the mean value of 0.75 m/s.

The distribution of the maximum air fraction beneath breaking waves at 0.12 m (Figure 5.3b) peaks at values just above the threshold value of 0.08 (section 5.1.1), shows a minimum at around 0.5 and a slight increase in the occurrence of larger values. (Values above 0.25 have to be considered approximate). The median value of maximum air fraction is 0.23.

5.1.4 Time and length scales of breaking waves

The size of a breaking wave is of great importance for estimating its energy dissipation, air-entrainment and generation of turbulence. In the ocean, breaking may occur at several scales from the microscale of a few centimetres up to the length of the dominant waves. Little is known about the distribution of scales. Phillips [1985] suggested the use of the phase speed c_{brk} of the breaking wave as a measure of the breaking scale, a method taken up by Ding & Farmer [1994]. By tracking the sound of breaking waves in the open ocean they obtained statistics on duration, velocity, spacing and breaking probability. Their 23 data sets, each of 30 minutes length show the ratio of c_{brk}/c_p to decrease from 0.75 for a dominant wave speed $c_p = 4.0\ \mathrm{m/s}$ to c_{brk}/c_p = 0.45 for a stronger wave field with $c_p > 10\,\mathrm{m/s}$. To our knowledge these are the only field observations of the breaking scale. Two recent studies, estimating the energy dissipation by breaking waves, yield also a scale of the breaking wave. Thorpe [1993] scaled laboratory measurements of dissipation rates of steady breaking waves with observed breaking frequencies and found, in order to match dissipation rates observed within the ocean mixed layer, the ratio c_{brk}/c_p has to take a value of 0.25. However, Melville [1994] pointed out that in the more realistic case of unsteady spilling breakers and a more complete account of the oceanic dissipation rate c_{brk}/c_p varies between 0.4 and 0.64. Furthermore, Thorpe's parameterization of the breaking frequency is not supported by our observations (see section 5.1.6).

The combination of breaking wave detection with the conductivity sensors and the local surface elevation allows estimation of the breaking scale. We define the wave period τ_{brk} of a breaking wave as the time between two successive local minima in the surface elevation, however a hysteresis effect is accounted for by disregarding waves with an elevation change of less than 0.1 m. Accordingly, the height H_{brk} of the breaking wave is defined as the difference in the surface elevation between the local minimum previous to the breaking event and the maximum within the period of the breaking wave. The peak period τ_p of the wave field is obtained from the peak of the wave height spectrum, and the significant wave height H_s is equal four times the standard deviation of the surface elevation [Kinsman, 1965]. Both quantities are calculated from data segments of 30 minutes duration. The following analysis summarizes the scale and geometry (section 5.1.5) of 57 breaking waves during the 03/12/93 deployment, which were characterized by a minimum air fraction $VF \geq 0.2$ and a temporal separation to preceding event of at least 16 s.

Figure 5.4 shows the distribution of the breaking wave period normalized by the period of the dominant waves τ_{brk}/τ_p. Applying the dispersion relation for linear deep water gravity waves yields $\tau_{brk}/\tau_p = c_{brk}/c_p$ which allows comparison with literature results. Most important, we find that breaking waves exist over a wide range of scales, most of them being significantly shorter than the dominant waves. The median value is 0.56, which is slightly higher than the peak value in the 0.3 to 0.4 range bin. 79% of the data fall into the range 0.2 to 0.8 and only 4% are less than 0.2. Melville's [1994] estimate of $0.4 < c_{brk}/c_p < 0.64$ covers only 25% of our data, and the range 0.45 to 0.75 reported by Ding & Farmer [1994] includes 35% of this data set. Thorpe's [1993] ratio of $c_{brk}/c_p = 0.25$, is low for this data set. In terms of wave length, which is related quadratically to wave phase speed, our data indicate that breaking happens over a wide range of scales, predominantly between 5% and 80% of the wave length of the waves containing most energy. For the open ocean this translates into breaking waves having a length of several meters up to more than 100 m.

The lower panel of Figure 5.4 gives the distribution of the normalized surface height at the onset of the air entrainment, *i.e.* when the air fraction surpasses a threshold of 0.08, and the normalized maximum height of the breaking wave. The normalization is done with respect to the significant wave height. 90% of air entrainment at the sensor depth started at a positive elevation above the mean surface level. The median value is at 0.34.

The above derived lower bound of the bubble injection velocity of 0.75 m/s leads to a delay of 0.3 s between the onset of breaking and the onset of air entrainment at the shallowest sensor depth, and for the majority of breaking events there is no significant difference in surface elevation between those two incidents. It has been argued [Phillips & Banner, 1974] that the augmentation of the surface drift near the long-wave crests facilitates the onset of breaking. However, our data set shows less than 4% of the breaking waves start at heights comparable to the significant wave height and does not support the concept of preferential breaking on or near the crests of longer waves.

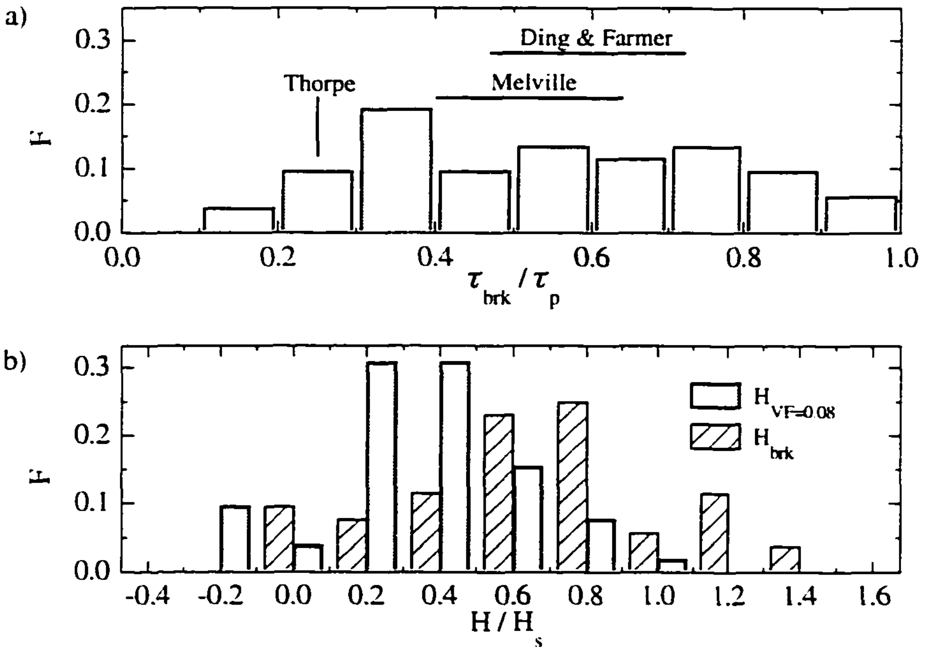

Figure 5.4: Distribution of scale of breaking waves on 03/12/93. a) Normalized period of breaking waves. Bars refer to breaking scale estimates by Thorpe [1993], Melville [1994] and Ding & Farmer [1994]. b) Normalized height of breaking waves (pattern) and normalized surface elevation at the onset of air-entrainment (gray).

The data show that 83% of the waves which break have a height less than the significant wave height. The distribution shows a slight peak in the range from 0.6 to 0.8. The median value is 0.67. Somewhat striking is the high proportion (11%) of breaking waves being smaller than 10% of the significant wave height , *i.e.* these waves have a height of less than 0.3 m.

5.1.5 Mean geometry of a breaking wave

Each breaking wave is individual in its characteristics, depending on very local conditions of wave and wind field. However, we expect the similarities of individual breaking waves to be strong enough to allow us a collective description of at least some of their properties. This is obtained in the following manner: All 52 breaking events were extracted as short data segments of 16 s length, which were centered at the time when the air fraction exceeds the threshold of 0.08. Subsequently, air fraction, surface height and velocities were ensemble averaged. The results are presented in Figure 5.5.

The average air fraction reaches a maximum value of 0.38 and a signal higher than 0.08 lasts for approximately 0.5 s. However, in several cases the signal is up to 1.5 s long, which prevents the average signal from dropping below 0.02 for the duration of these few longer events. At the beginning of the air entrainment the air fraction rises slowly from the detection threshold of 0.005 to 0.02 within approximately 0.2 s from where it reaches the maximum value within less than 0.2 s. The decrease of the signal is similarly rapid.

Due to the wide range of variations in the surface elevation of breaking events, as discussed in section 5.1.4, we subtract the minimum value of surface elevation within the breaking wave prior to averaging the surface elevations. Although the time series of the air fraction signal at a fixed point is given (Figure 5.5b), the graph could also be interpreted as a cross section of a wave traveling from right to left.

The surface rises steadily from an average value of 1.1 m to 3.5 m within 3.5 s and then

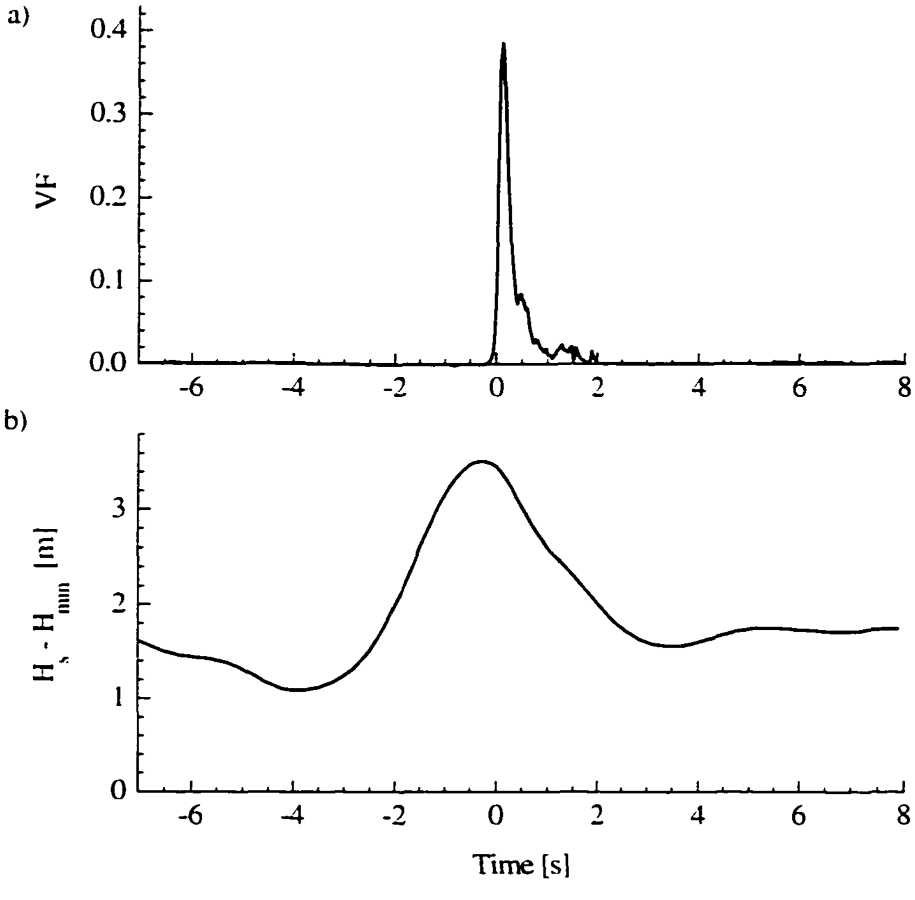

Figure 5.5: Average breaking wave quantities: a) air fraction at 0.18 m depth, b) surface elevation above minimum elevation within the period of the breaking wave.

drops off to 1.6 m within the next 4 s. The time of the maximum surface elevation coincides with the onset of the air entrainment, *i.e.* where the air fraction exceeds our detection limit. At the time of the maximum air fraction the surface has already dropped by 0.18 m. However, this value has to be taken with some caution since the reduced buoyancy of the floats in the foam of a whitecap could cause an apparent drop in surface height (which is obtained from the acceleration of the sensor boom), but not as much as 0.18 m on average. The surface geometry found here agrees with the onset of the instability starting at the crest, where the water particle speed exceeds the phase speed of the wave and spills forward. Although the active air entrainment occurs at the forward side of the wave a cloud of air is only detected at 0.2 m depth substantially downstream from the crest. An even more pronounced delay of the air fraction signal relative to the maximum surface elevation was observed by Lamarre & Melville [1994] in a study of large-scale three dimensional laboratory waves.

5.1.6 Frequency of breaking waves

The frequency of occurrence of a breaking wave at a point not only determines the energy input into via breaking waves to the ocean surface layer, but it is also a key parameter for a potential scaling of laboratory results of breaking wave studies to field conditions. The knowledge of how often a breaking wave is expected at a certain point is also of great significance for ocean engineering and risk assessment. Within the last 25 years there have been several field studies evaluating the frequency of breaking [Toba, 1971, Thorpe & Humphries, 1980; Longuet-Higgins & Smith, 1983; Weissman *et al.*, 1984;

Holthuijsen & Herbers, 1986; Su & Cartmill, 1992; Ding & Farmer, 1994], using different detection methods (section 5.1.1). Partly due to the different breaking criteria but more important due to an incomplete account of the physical processes leading to the breaking of waves, no consistent description of the relation between breaking frequency and the relevant physical parameters exists.

As a first order approximation, the frequency of breaking is expected to closely follow the wind speed. This can be seen *e.g.* in the breaking frequency during the 25/02/92 deployment. For a scatter plot of breaking frequency versus wind speed summarizing most of the published data see Holthuijsen & Herbers [1986] or Thorpe [1993]. Figure 5.6 (top panel) shows the 15 minute mean value of the breaking frequency, expressed as number of breaking waves detected at the sensor per minute, and the corresponding wind speed (bottom panel). Also shown is the number of breaking waves exceeding an air fraction threshold of 0.05 at the conductivity cell in 0.46 m depth and 0.03 at the two lower sensors. Results from the three deeper sensors can not be interpreted as breaking frequency but rather as the frequency of intense breaking waves, most likely of plunging nature. While the wind speed increased steadily from 5 m/s at 2300h, 24/02/92 to 17 m/s at 2000h, 25/02/92 the breaking frequency shows also an upward trend from 0.5 breaking waves per minute up to 2.5. However, despite the decreasing wind speed after 2020h the breaking frequency increases further until 0000h, 26/02/92. By that time the wind speed had already dropped by more than 10 m/s. Not until three to four hours after the change in the trend of the wind speed did the breaking frequency decline. During this period the wind and wave field were clearly not in equilibrium, and it is seen that the wave development has to be considered as a relevant factor in evaluating the breaking frequency. We restrict our further analysis to breaking statistics obtained during the first four deployments of our instrument, thereby excluding possible uncertainties due to different instrumentation and breaking criteria.

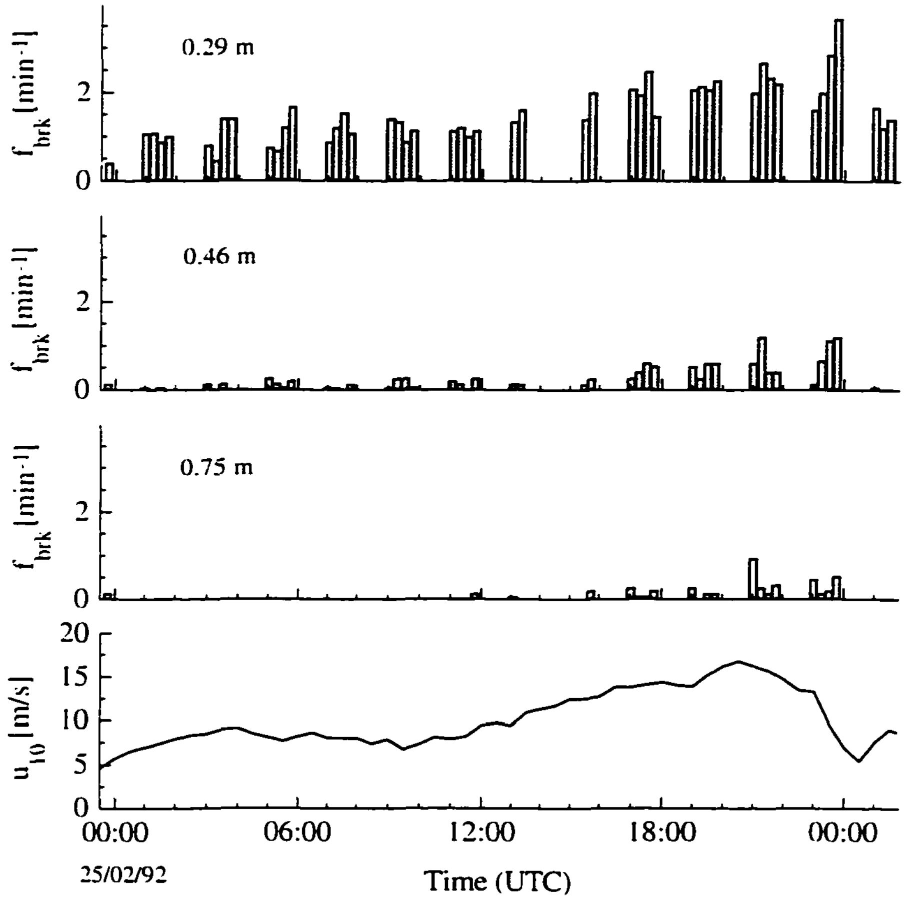

Figure 5.6: Frequency of breaking waves on 25/02/92 (top) and frequency of deeply penetrating breaking waves (panel 2-3). Note that the instrument did record only during odd hours and no data were collected between 1340h and 1520h. Lower panel gives wind speed during the deployment period.

Commonly, the state of the wave development is described by wave age c_p/u_{10} or c_p/u_*. For a "young" wave field the phase speed c_p of the dominant waves is much smaller than the wind speed at 10 m height. Definition of the wave age in terms of phase speed and friction velocity accounts for differences in wind-wave coupling due to wave steepness and atmospheric stratification and if available is the preferred definition.

The frequency of occurrence of breaking waves can be normalized by the period of the dominant waves τ_p to obtain the *fraction of breaking waves* or the *relative breaking frequency*. Figure 5.7 gives the relative breaking frequency as a function of inverse wave age. Each data point represents a mean value over 30 minutes. While in general data points are widely scattered a trend of decreasing relative breaking frequency towards more developed waves can be observed for individual data sets. However, no trend holds for different deployments. On 03/12/93, when the inverse wave age ranged between 0.2 and 0.35, less than 15% of waves did break. For the same range of inverse wave age this fraction was two to five times larger on 09/12/93. Both data sets were obtained by the same instrument and the same breaking criterion was applied. Wind speed for both periods are comparable, but wind direction differed by approximately 150°, creating a fetch limited environment on 03/12/93. Fetch during the 24/11/91 deployment was even shorter, and these data build a cluster on the scatter plot, almost completely separated from the open ocean data.

Two conclusions can be drawn from the separation of individual data sets: using wave age as description of forcing of breaking waves lacks some key physical processes concerning the breaking frequency, and secondly the period of dominant waves is not the appropriate normalization of breaking frequency. This is in keeping with the broad range of breaking scales as seen in Figure 5.4, with less than 10% of breaking waves having a scale comparable to the dominant waves.

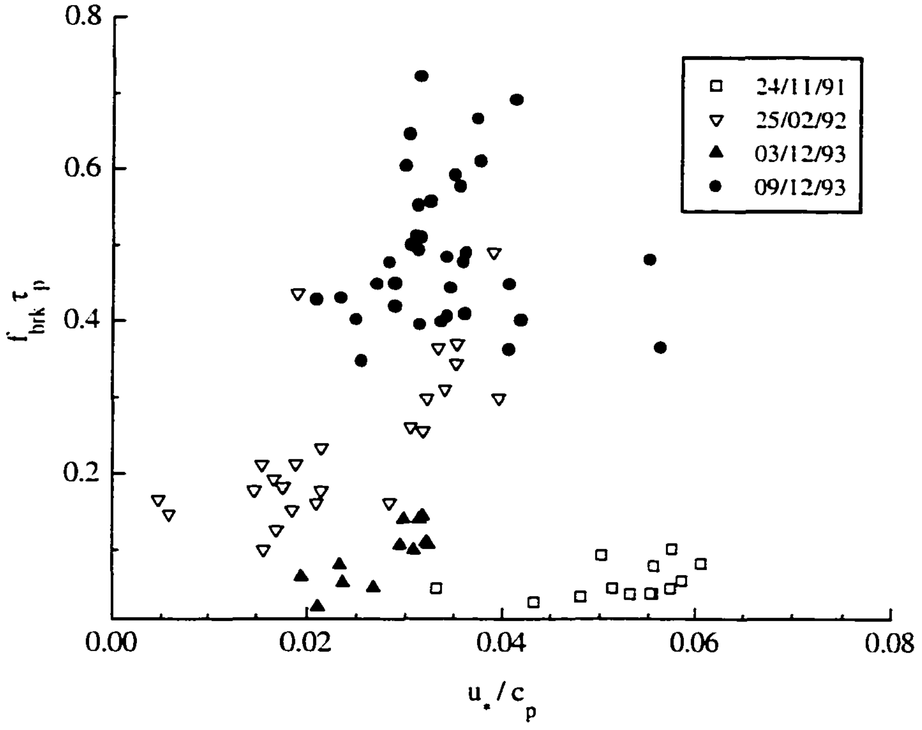

Figure 5.7: Relative breaking frequency as function of inverse wave age for four deployments. Each data point represents a 30 minutes average.

Breaking is believed to be the main factor in wave energy dissipation [Komen *et al.*, 1994]. We therefore expect the occurrence of breaking waves to be related to the energy input into the wave field, which ultimately gets dissipated. The energy input from the wind into waves predominantly occurs through form drag at high frequency waves, and for fully developed seas it can be estimated from Equation (2.19) [Gemmrich *et al.*, 1994]. This estimate can serve as a reference state. Form drag exerted from the atmosphere on a wave component also depends on the amplitude of that spectral component. For wave fields differing from the reference state the actual spectrum of the high frequency waves has to be taken into account. This is done in the formulation given in Equation (2.16). There is general agreement of the growth factor β being proportional to the square of the wind speed and the cube of the frequency, but individual parameterizations differ in their exact formulation [Plant, 1982; Donelan & Pierson, 1987; Hsiao & Shemdin, 1983; Caudal, 1993].

The formulation by Donelan & Pierson

$$\frac{\beta}{\omega}=0.194\frac{\rho_a}{\rho_w}\left(\frac{u_{\pi/k}\cos\varphi}{c(k)}-1\right)\left|\frac{u_{\pi/k}\cos\varphi}{c(k)}-1\right| \tag{5.3}$$

offers the weakest coupling between wind and low frequency waves among all formulations and for a mature wave field it approaches the energy input of the reference state. $u_{\pi/k}$ is the wind speed evaluated at a reference height corresponding to one half wave length and is calculated assuming a logarithmic wind profile

$$u_{\pi/k}=u_{10}\left(1+\frac{\ln\frac{\pi/k}{10}}{\ln\frac{10}{z_0}}\right) \tag{5.4}$$

The roughness length of the ocean surface relevant to the air flow is obtained from the empirical expression [Donelan, 1990]

$$z_0 = 1.38 \times 10^{-4}\, H_s \left(\frac{u_{10}}{c_p} \right)^{8/3} \tag{5.5}$$

rather than the classical Charnock relation [Charnock, 1955]

$$z_0 = \frac{m u_*^2}{g} \tag{5.6}$$

with the empirical constant $m = 0.0144$, which is correct only for developed seas.

Directional observations of the wave field were obtained only during the 25/02/92 deployment and a directional spreading of $\cosh^{-2}(\alpha\varphi)$ [Donelan *et al.*, 1985] was assumed for the other wave spectra, where α is a constant and φ is the wave direction relative to the wind direction. Furthermore, at frequencies above approximately 0.8 Hz the measured wave spectra become unreliable and hence a ω^{-5} tail [Banner, 1990] was added to the spectra from 0.6 Hz to 7.5 Hz.

The dependent parameter in the description of the breaking frequency will be defined as the energy input into the wave field F_w (Equation 2.16) normalized by the energy input into a mature wave field F_{GMP} (Equation 2.19)

$$\frac{F_W}{F_{GMP}} = \frac{g \int \beta S \, d\omega \, d\varphi}{u_*^2 \, c_{GMP}} \tag{5.7}$$

This parameter relates mostly to the conditions of wave components short compared to the peak of the wave spectrum, which account for most of the breaking. Similarly, a normalization time scale has to consider the scale of the breaking waves rather than the scale of the dominant waves. As seen in the analysis in section 5.1.4 this scale varies over a wide range and might depend on the wave field itself [Ding & Farmer, 1994]. Kitaigorodskii [1983] proposed the existence of a dissipative subrange at wave numbers larger than a transitional value of

$$k_\varepsilon = C \frac{g}{E_0^{2/3}} \tag{5.8}$$

where E_0 represents the energy flux from the region of energy input towards high wave numbers. Assuming a balance between energy input and dissipation [Gemmrich *et al.*, 1994] this energy flux E_0 is equal to F_W, and hence the time scale of dissipative waves can be estimated as

$$\tau_{diss} = C^{-1/2} \frac{2\pi \, F_W^{-1/3}}{g} \tag{5.9}$$

The constant C derived in Kitaigorodskii [1992] as $C = 1.6 \times 10^{-3}$ yields time scales for our data sets between 1 s and 3.5 s. However, we anticipate air entrainment is associated with larger waves in the dissipative range and adjust the constant to have the median value of τ_{diss} match the median value of τ_{brk} (Figure 5.4) for the 03/12/93 deployment. This results in a value of $C = 1 \times 10^{-4}$. The formulation of a time scale of breaking waves can also be obtained on purely dimensional grounds, which leads to the same formulation as given in Equation (5.9).

The above derived time scales serves as normalization of the breaking frequency:

$$\tilde{f}_b = f_{brk}\ \tau_{diss} \tag{5.10}$$

In Figure 5.8 this normalized breaking frequency is plotted against the normalized wave energy input F_W / F_{GMP}. Compared to the broad scatter in Figure 5.7 a much more pronounced relationship between the breaking frequency and the forcing parameter emerges, which collapses all four data sets. For energy input less than defined by the reference state only little breaking activity takes place with $\tilde{f}_b < 0.05$. When there is excess energy input, $F_W > F_{GMP}$, breaking waves occur more frequently and $\tilde{f}_b$ increases roughly linearly. The most frequent breaking occurs on 09/12/93 where about 40 % of waves with a size comparable to the median size of breaking waves break when the energy input reaches three times the energy input of the reference state.

There are limitations in the calculation of F_W and τ_{diss}, in particular the assumption of a universal directional spreading, which would clearly not be applicable for the 25/02/92 data set (see Figure 4.4) and the neglect of energy advection (see section 2.4).

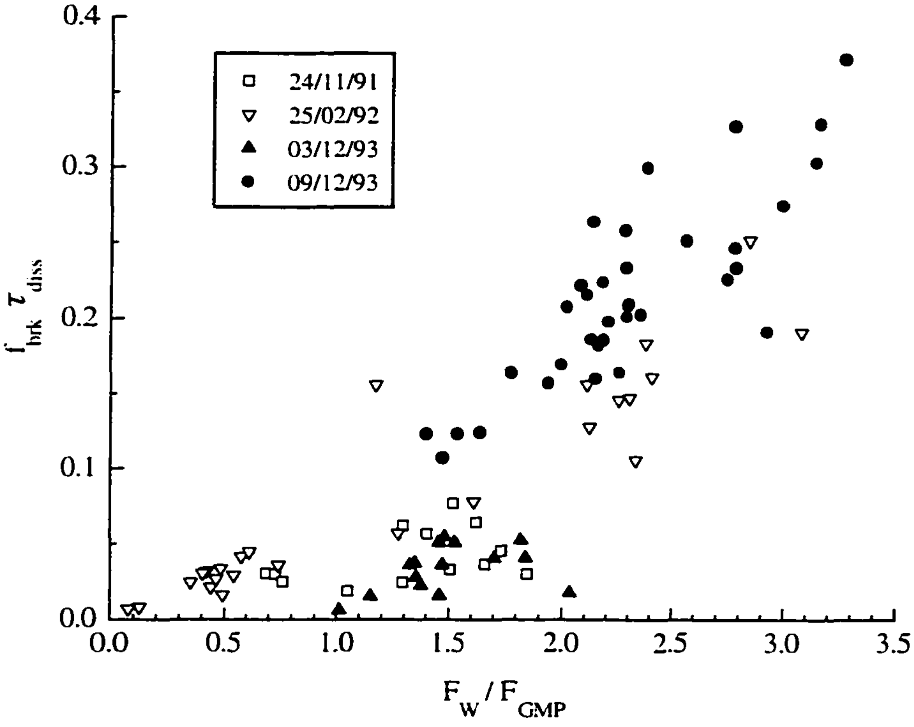

Figure 5.8: Normalized breaking frequency as function of scaled energy input into the wave field. Same data points shown as in Figure 5.7.

Nevertheless, data sets of such diverse conditions as measurements in a coastal strait and in fetch limited and fetch unlimited open ocean environments collapse under this scaling. This indicates that the interaction of wind and high frequency waves, as described by F_W / F_{GMP}, captures the physical processes leading to breaking adequately and a time scale τ_{diss} relating to this interaction provides an appropriate normalization of the frequency of occurrence of breaking waves.

5.2 Near surface temperature variability

For a given heat flux the near surface temperature structure is a direct manifestation of the underlying turbulence and advection field. The analysis of the temperature field can be divided into three sub-domains representing different aspects of the turbulence. Interpretation of these components is given in chapter 6.

Very near the surface the temperature structure of a wind driven sea seems to be dominated by brief fluctuations of roughly 20 mK to 100 mK coincident with wave breaking. The temperature signal of breaking waves diminishes with depth, and below 1 m fluctuations of time scale of the order of minutes prevail, which are believed to be caused by Langmuir circulation. The analysis of the temperature profile in the upper 2 m provides the link between deeper temperature structures and heat exchange across the air-sea interface. A preliminary account of near surface temperature fluctuations based on the initial instrument deployment on 24/11/91 together with an estimate of the contribution of breaking waves to the air-sea heat flux is reported by Farmer & Gemmrich [1996].

5.2.1 Temperature fluctuations within breaking waves

Figure 5.9 shows a short time series of air fraction and temperature at 0.12 m depth recorded on 18/04/95. A brief temperature anomaly of approximately -20 mK, associated with a breaking wave, exceeds the background fluctuations significantly. Air entrainment in this example lasts for 0.8 s and reaches a maximum of approximately 0.08. The sensor depth derived from the capacitance wire gauge varied by 15 mm (Figure 5.9 bottom) during this event and stayed well below the depth where surface proximity could bias the measurement (Appendix A). Although the start of the temperature anomalies cannot be defined unambiguously, it can be seen that the temperature drops prior to the entrainment of air and it recovers to the background level within 0.5 s after the decline in air fraction. The change in temperature occurs when water of anomalous temperature is mixed down by the action of breaking from the thermal boundary layer to the sensor depth.

During the breaking event the thermistor is surrounded by an air-water mixture with often more than 50 % air. Since the heat capacity per unit volume (ρc_p) of water is more than 3000 times that of air the heat content of bubbles is negligible, and the temperature of the air-water mixture is dominated by the temperature of the water. However, the time it takes for the air bubble temperature to equilibrate with the surrounding water depends on the bubble size. This equilibration time may exceed the time it takes for the bubble to reach the sensor. A lower bound on the bubble injection speed can be inferred from the delay of the onset of the conductivity signal between the two shallowest sensors and their spatial separation, under the assumption that the bubbles are traveling vertically with respect to the sensors. We inferred speeds varying from 0.4 m/s to 1.9 m/s with a median value of 0.9 m/s [Farmer & Gemmrich, 1996]. Koga [1982] measured the speed of bubble entrainment in a wave tank at a wind speed of 16 m/s and found values between 0.4 m/s and 1.2 m/s.

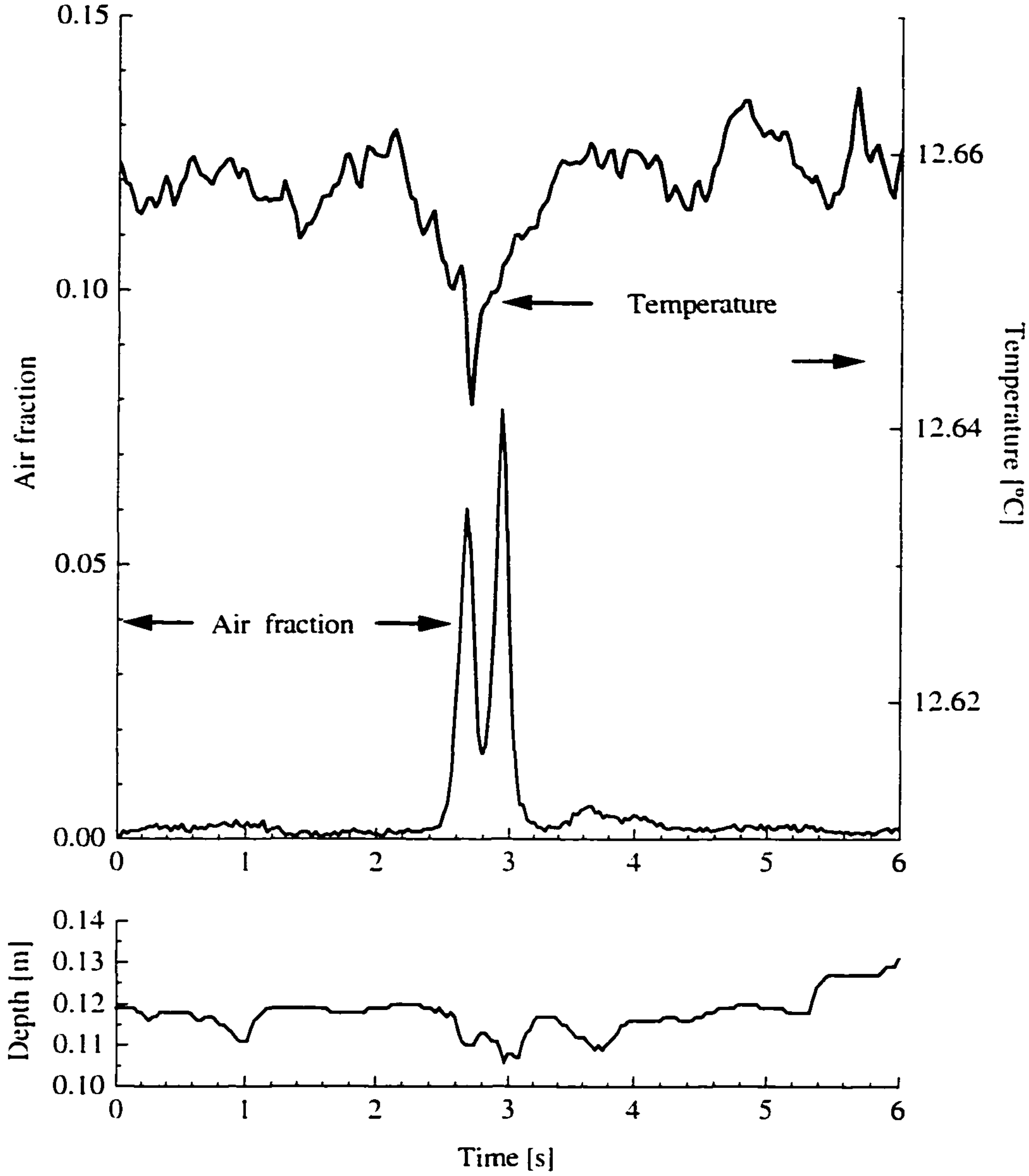

Figure 5.9: Temperature anomaly and air-fraction (above) and sensor depth (below) during a breaking event at 18/04/95, 01:13:26 PDT.

Thus we take 0.2 s as the minimum time bubbles need between their formation and their arrival at the thermistor depth. In Appendix B we model the equilibration process and show that only bubbles larger than 6 mm diameter will fail to equilibrate to the water temperature within this bubble transit time. For larger bubbles the thermistor response depends upon bubble sizes, flow speed and bubble separation. The model also illustrates the distinctive character of the signal from air temperature measurements in large air bubbles (diameter greater than approximately 15 mm). Those events are identified by their distinct sawtooth-like signal and are excluded from the data. For all other examples we conclude that the observed temperature signal is not significantly influenced by the temperature within the air bubbles.

The magnitude of temperature anomalies can be defined as the difference between the mean temperature value 2.5 s to 0.5 s prior to the onset of the air-fraction signal and the temperature during the breaking event. An individual breaking event will be characterized by the average temperature anomalies during the period of air-entrainment, which will in the following be called temperature anomaly. A summary of temperature anomalies for three experiments is given in Figure 5.10. Temperature anomalies associated with breaking waves occurred during all deployments, and both positive and negative anomalies were observed. The magnitude of individual events varied from the detection limit of roughly 5 mK up to 150 mK. Three main conclusions about temperature anomalies in breaking waves can be drawn.

As seen in all three deployments, the sign of the bulk of temperature anomalies is defined by the air-sea heat flux (Chapter 4). Note that there is some uncertainty in the

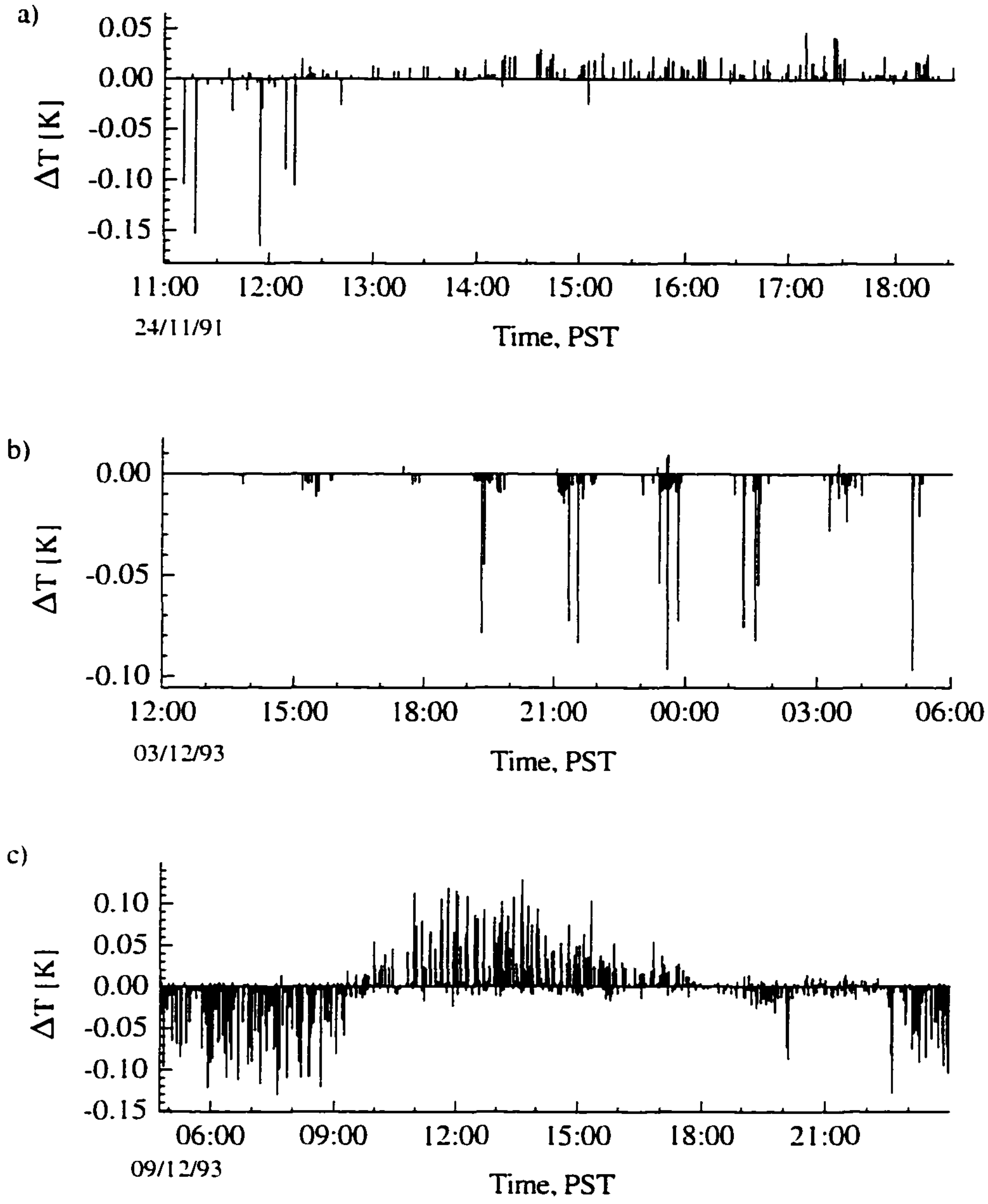

Figure 5.10: Time series of event-averaged temperature anomalies. a) 24/11/91 at 0.17 m depth, b) 03/12/93 at 0.21 m depth, c) 09/12/93 at 0.19 m depth

time the heat flux changes from negative to positive on 24/11/91 [Farmer & Gemmrich, 1996]. During all of the 03/12/93 deployment the ocean thermal boundary layer is losing heat (Figure 4.5) and only negative temperature anomalies are observed. On 09/12/93 the heat flux (Figure 4.8) is negative at the beginning, changes sign at 0920h, remains positive until 1730h and negative afterwards. The same pattern can be seen in temperature anomalies.

Most of the time total heat flux and sensible heat flux are of the same direction and it cannot be determined unambiguously whether temperature anomalies are linked to air-sea temperature differences (which define the sign of the sensible heat flux) or the heat budget of the thermal boundary layer. However, negative temperature anomalies occur during the first 90 minutes of the 24/11/91 deployment and between 1800h and 2300h on 09/12/93 - two periods with positive air-sea temperature differences. Hence, temperature anomalies are forced by the combined action of heat flux components and not only by air-sea temperature differences.

Generally, the magnitude of the largest temperature anomalies is related to the magnitude of the heat flux. One exception is the beginning of the 24/11/91 data set, where large anomalies occur which may result from the stabilizing effect of the rain [Katsaros, 1976], which would reduce vertical mixing between breaking events. However, no significant change of the magnitude of temperature anomalies is observed during periods of precipitation within the other data sets. Breaking might be too frequent during those periods to allow an enhanced gradient to build up, which could increase temperature anomalies.

Despite a significant heat loss of the thermal boundary layer of $-100\,\mathrm{Wm}^{-2}$ to $-150\,\mathrm{Wm}^{-2}$ maximum temperature anomalies of less than 15 mK were observed during the beginning of the 03/12/93 deployment. After 1900h the magnitude of the strongest temperature anomalies increased drastically to values up to 100 mK with a relatively small increase in thermal boundary layer heat loss. Similar heat flux values of $-100\,\mathrm{Wm}^{-2}$ during other deployments are related to temperature anomalies of 100 mK. The lack of strong temperature anomalies is attributed to the lack of Langmuir circulation during this time period (Figure 4.7). A strong drop in wind speed and a 150° change in direction which occurred around 1030h caused the wind and wave field to be misaligned, resulting in a suppression of Langmuir circulation [V. Polonichko, personal communication].

Simultaneous observations of temperature and bubble cloud structure on 24/11/91 and 18/04/95 reveal strong Langmuir circulation whenever temperature anomalies in breaking waves are observed. However, there are no further observations of poorly organized bubble clouds and simultaneous near surface temperature measurements to further strengthen the hypothesis that temperature anomalies in breaking waves are associated with the presence of Langmuir circulation.

Between 35 % to 65 % of breaking events exhibit measurable temperature anomalies. Figure 5.11 gives the distribution of the magnitude of temperature anomalies for all data sets. On 24/11/91 only 35 % of breaking events cause a temperature anomaly of 5 mK or more, with only a few events of $\Delta T > 30\,\mathrm{mK}$. (Data prior to 1500h are not included in this histogram due to uncertainties of heat flux and effects of rain). During the other deployments, when the heat flux is much more pronounced, the fraction of breaking waves with distinct temperature anomalies is around 60 %, the majority of events having a temperature anomaly between 5 mK and 50 mK.

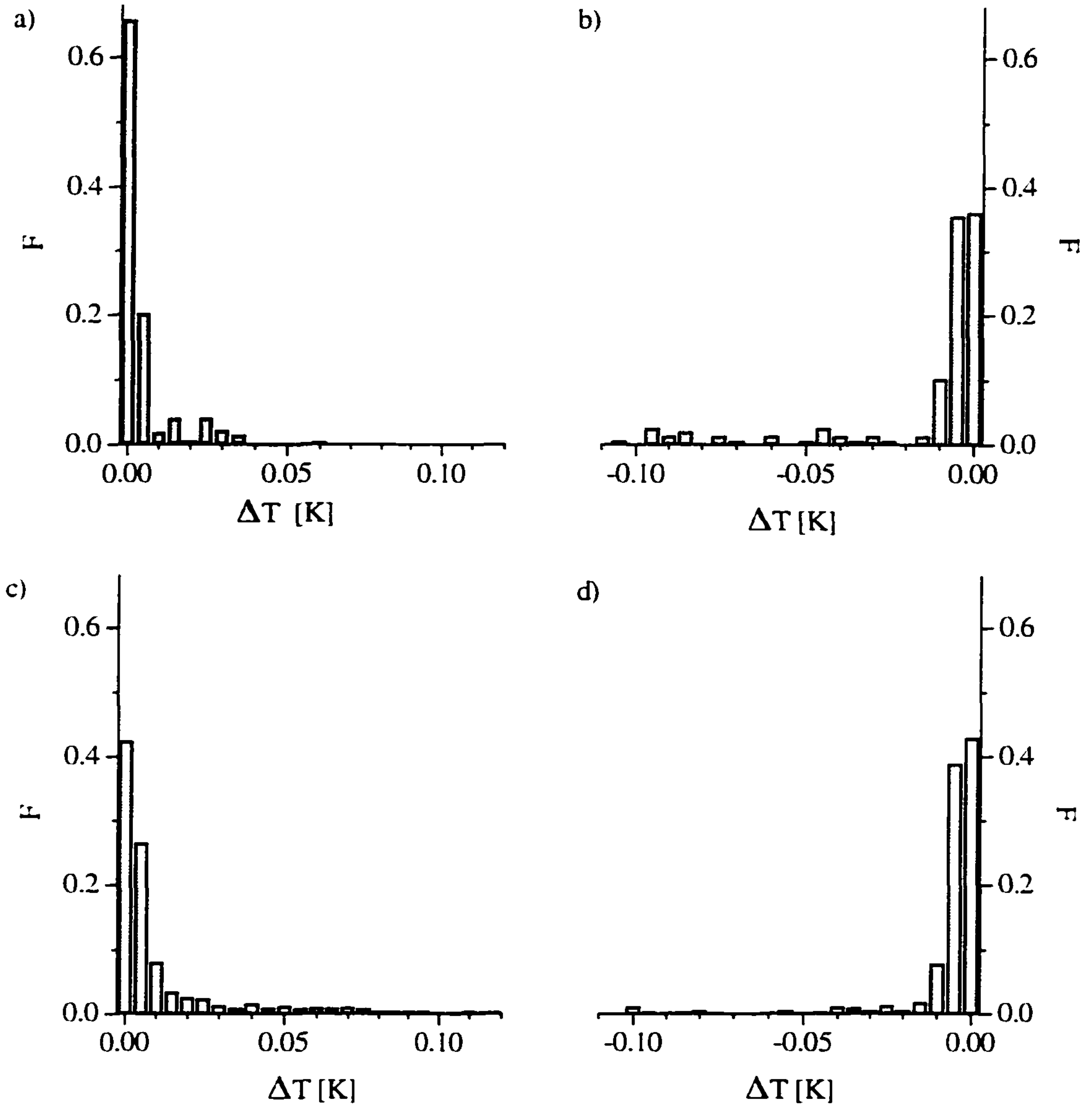

Figure 5.11: Histogram of event-averaged temperature anomalies for a) 24/11/91, 1500h to 1800h, b) 03/12/93, 1330h - 04/12/93, 0525h, c) 09/12/93, 0950h - 1750h, d) 18/04/95, 0115h - 0825h.

The surface shear and an average instrument drift of 0.3 m/s ensure that successive breaking waves do not mix the same area detected in the preceding event, if the time delay is more than approximately 7 s. Furthermore, the recovery time of the cool skin has been measured following its destruction by a breaking wave and found by infra-red imager to be approximately 1 s [Jessup, 1996], and by radiometer [Clauss et al. 1970] to be 10 s. This rapid recovery time shows that the thermal skin is only briefly interrupted by breaking. However, since measurable temperature anomalies are found in only a fraction of breaking events we infer that within one third to two thirds of the surface area the thermal boundary layer is too thin to be detected following mixing to the depths of our sensors. This will be discussed further in section 6.2.

A summary of the depth dependence of temperature anomalies is given in Figure 5.12 where the percentage of events with a certain temperature anomaly at four sensor depths is presented. At the shallowest sensor the fraction of events with $\Delta T > 5\,\mathrm{mK}$ is 30 %, 3 % at 0.26 m depth and less than 2 % at deeper sensors. While 13 % of the events exhibit a temperature anomaly of more than 10 mK at the top sensor, almost no event caused such an anomaly at any of the deeper thermistors. Two factors cause this rapid decline of temperature anomalies with depth: Mixing of the water of anomalous temperature with the surrounding water and the shallow penetration depth of breaking wave as seen in the air fraction (section 5.1.3).

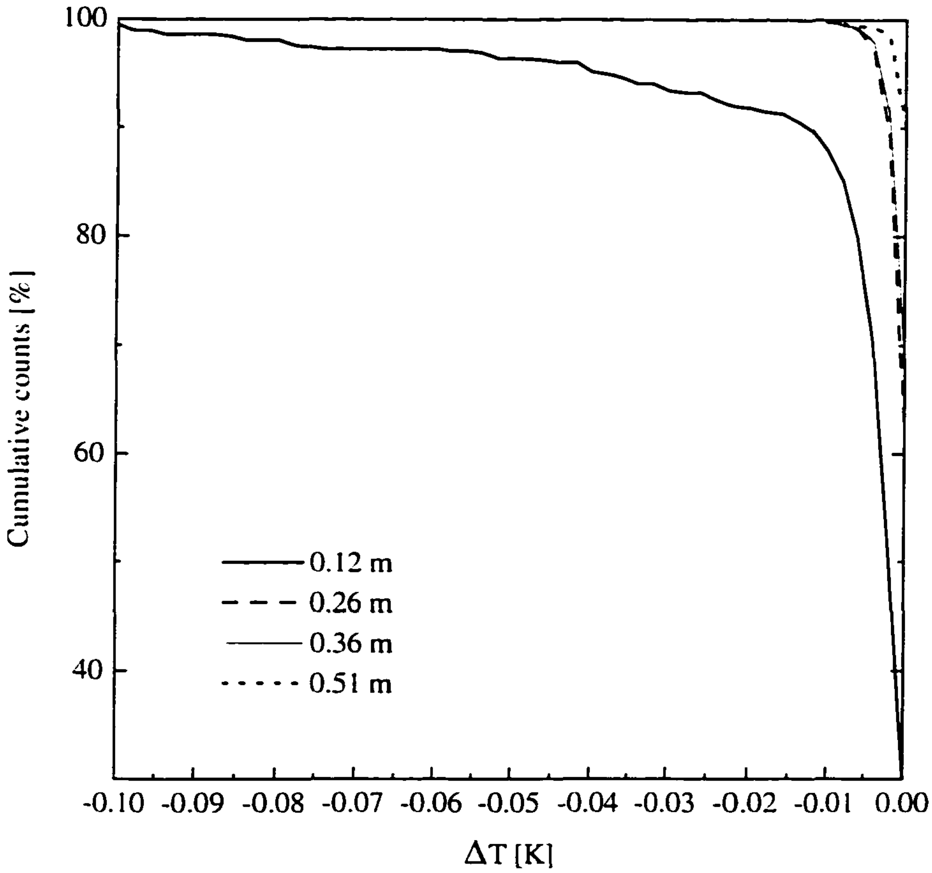

Figure 5.12: Distribution of temperature anomalies in breaking waves on 18/04/95 at four sensor depths.

5.2.2 Near surface temperature profile

The addition of the profiling thermistor prior to the MBL experiment provided a unique data set of 414 temperature profiles in the surface layer of a wind driven sea. The profiles reach from 1.8 m depth to well within the air and take about 4 s for one leg. In order to avoid distortion of the measured temperature field due to the structure of the profiling cart, which is located below the thermistor, only upward profiles are utilized in the subsequent analysis.

The given travel speed of the profiler and the temperature sampling rate of 34.375 Hz yield a spatial resolution of 14.4 mm. Depth is determined by the revolutions of a precise stepper motor. A complete revolution, involving 200 individual steps, takes 320 ms. The profiler position was calibrated by measuring the distance which the profiler travels per stepper motor revolution. This was done for six revolutions which covers approximately the total range of the profiling distance. The mean value obtained is 159.67 mm per revolution, providing a resolution for the profiler position of ~0.8 mm. All depths are referenced to the instantaneous surface height as recorded by the capacitance wire gauge. However, the separation between the wire gauge and the profiler introduces an uncertainty in the depth correction of up to 20 mm, depending on the slope of the water surface.

Individual profiles reveal the rich fine structure of the near surface temperature field with fluctuations of up to 30 mK. The two profiles in Figure 5.13 show the variability of the temperature structures observed. A more extensive set of profiles is provided for reference in Appendix C. All profiles analyzed have been referenced to the instantaneous surface detected via the capacitance wire gauge. In the first profile shown maximum deviations from the mean are less than 4 mK, whereas the second profile reveals a parcel of water between 0.2 m and 0.4 m depth approximately 12 mK warmer than the mean and a second disturbance of 5 mK between 1 m and 1.5 m depth. These disturbances are caused by water masses advected horizontally or from greater depth.

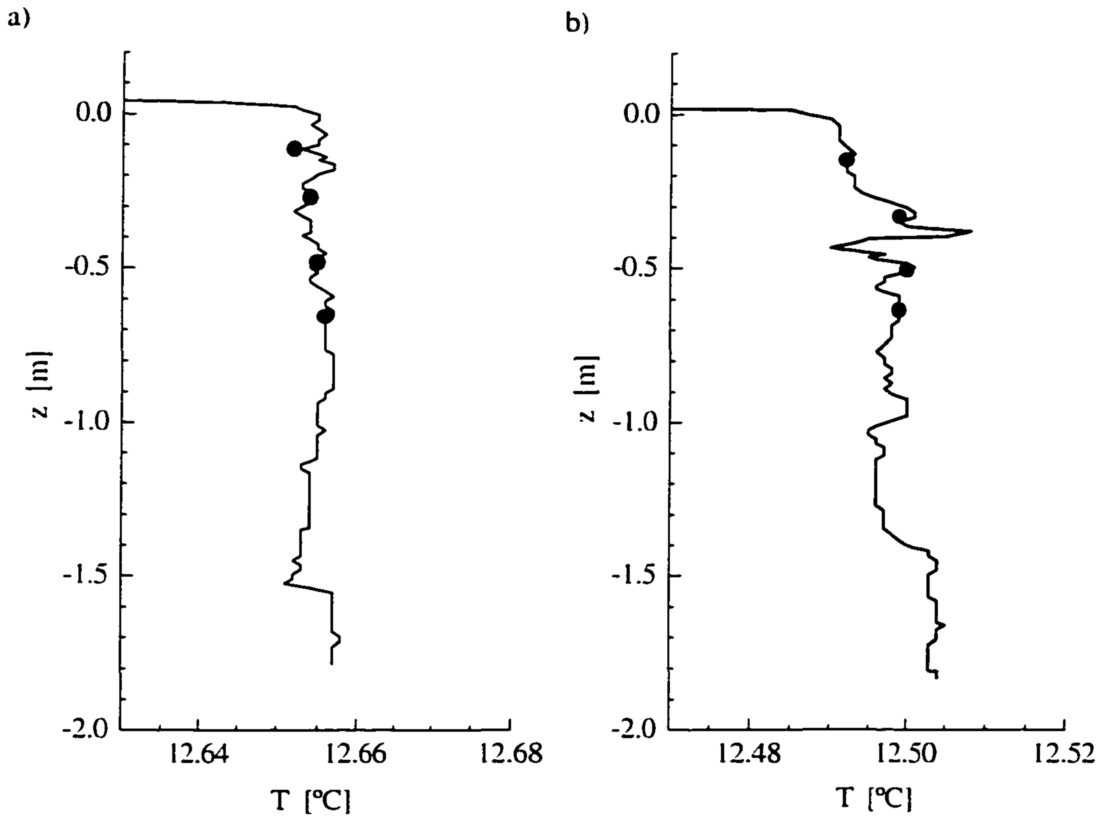

Figure 5.13: Near surface temperature profiles (line) on 18/04/95 at a) 0033h and b) 0448h. Circles give temperatures recorded with fixed depth thermistors.

Unfortunately, the severe conditions prohibited CTD (Conductivity, Temperature, Depth) casts on 18/04/95. However, a CTD profile at 17/04/95, 0846h shows a layer 0.2 K warmer than the mixed layer temperature at 37 m to 58 m depth. By the time of the following CTD cast on 19/04/95, 1016h the mixed layer, deepened to 45 m and cooled by

0.15 K, still rests atop this warmer layer. This indicates a source of water warmer than the mean near surface temperature is located in about 40 m depth.

The strong heat flux causes decreasing water temperature closer to the ocean surface. This temperature profile is modeled by integration of Equation 2.1, with the assumption of a wave enhanced diffusivity profile (which will be justified in section 6.1). For a heat flux of –250 W/m^2 a total temperature difference of 35 mK is predicted between the surface and 40 m depth, and a 20 mK deviation from the temperature value at 1 m depth is achieved at depths greater than 13 m.

As discussed in section 5.2.3 horizontal temperature fluctuations of 20 mK occur over a distance of tens of metres and are a further possible origin of the fluctuations observed in individual profiles.

The vertical extension δz of the disturbances in the near surface temperature profiles describes the scale of the turbulence elements responsible for the fluctuations. This extension is defined by the distance between two successive temperature minima or maxima. Disturbances of 2 mK or less neighboring a larger disturbance are thought to be part of this and their size is added to the size of the larger fluctuation. The magnitude δT of the disturbance is taken as the maximum temperature difference within the part of the profile defining the disturbance. The results for the two profiles given in Figure 5.13 are shown in Figure 5.14.

In total, 977 disturbances fitted this definition. Their magnitudes and sizes are given in Figure 5.15. Strongest fluctuations are observed close to the surface - the median value of the magnitude at 0.1 m depth being 11 mK and 5 mK at 1.5 m depth. Maximum values close to the surface are about 30 mK, but only 10 mK at the bottom of the profile.

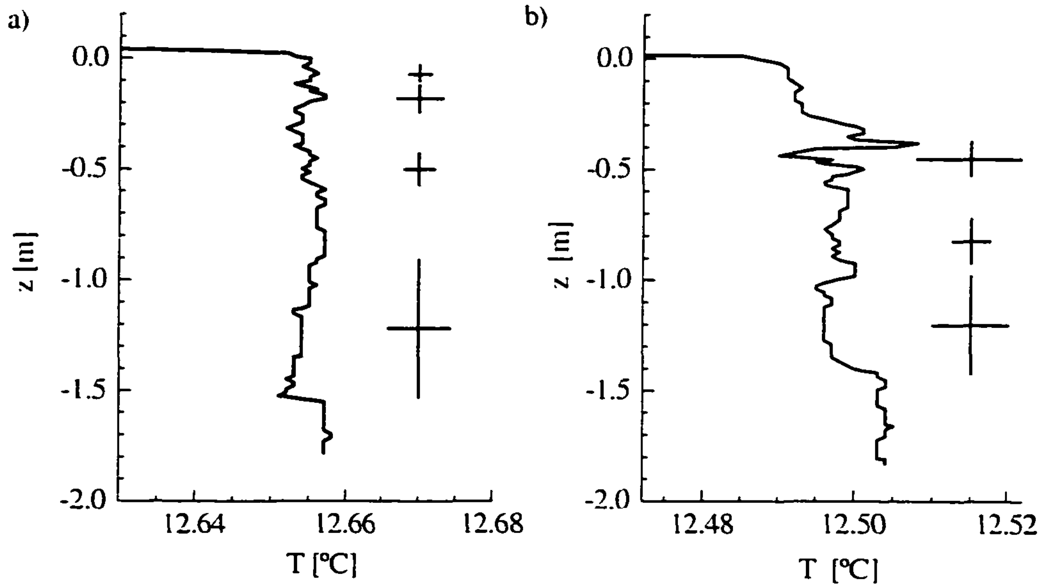

Figure 5.14: Scale of temperature fluctuations (same profiles as in Figure 5.13). Vertical bars depict vertical extensions δz of detected temperature disturbances and horizontal bars represent their magnitudes δT.

Diffusion increases with depth, which causes water parcels of anomalous temperature to equilibrate to the ambient temperature faster at greater depth than close to the surface. If the anomalous water originated from below, the temperature fluctuations would be expected to decrease towards the surface, which is clearly not the case in our data set. We therefore take strong vertical near surface temperature gradients as the most likely source of temperature fluctuations within the near surface profiles.

Our ability to determine the size of temperature disturbances is limited by the maximum

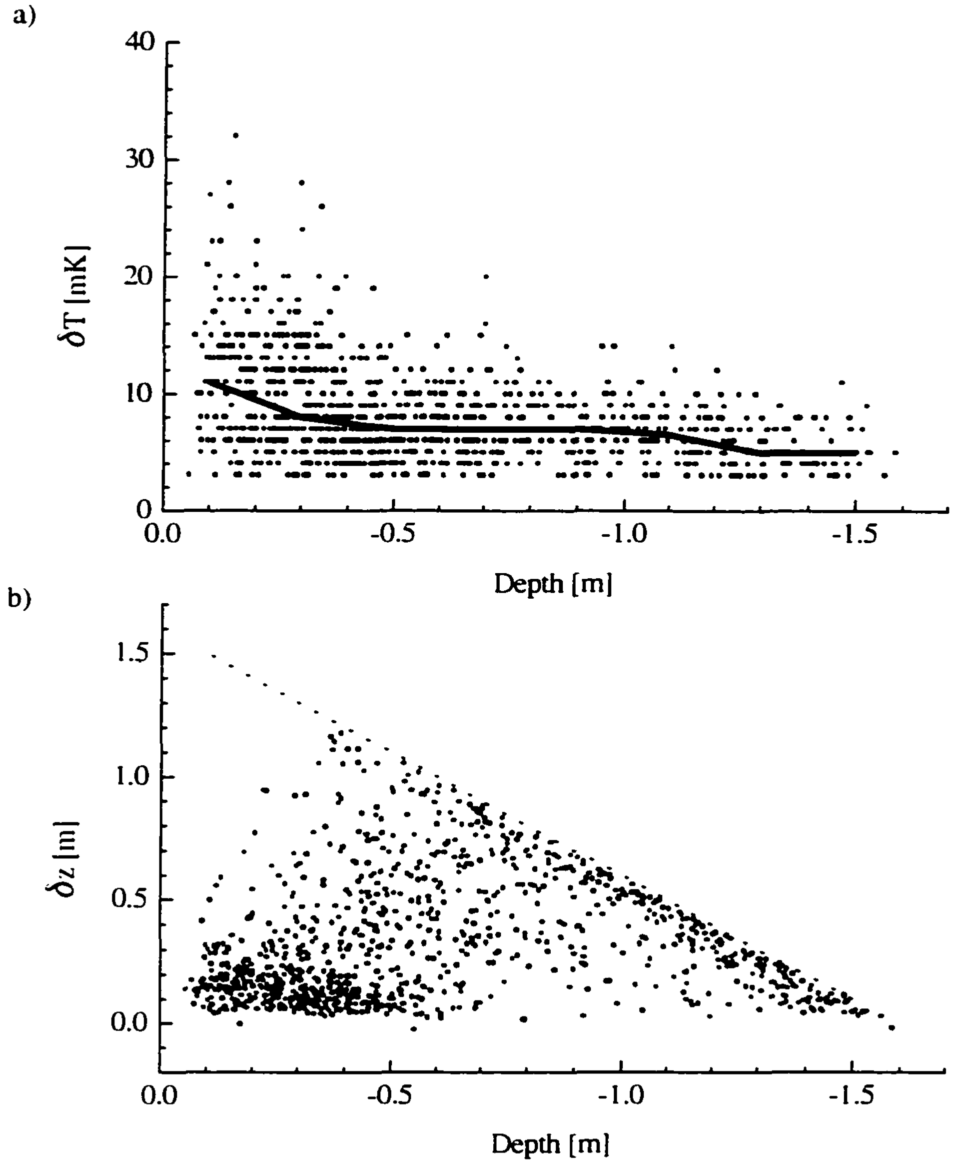

Figure 5.15: a) Magnitude of temperature disturbances in near surface profiles. Line represents median values in 0.05m depth bins. b) Vertical extension of temperature disturbances. The profiling depth of 1.8 m limits size estimation to values below the dotted line.

depth of the profile. Despite this limitation a tendency of the size of turbulence elements to increase with increasing depth can be seen in the upper 0.8 m, where the size estimate is not affected severely by the maximum profiler depth (Figure 5.15b). The median value within 0.05 m depth bins has a nearly constant value of 0.18 m within the top 0.3 m and increases linearly below. The cluster of data points in the vicinity of the measurement limit at depths greater than 0.8 m is an artifact of the size detection scheme. For further statistical analysis of the size estimates above 0.8 m depth the bootstrap method [Efron & Gong, 1983] is applied. The mean and standard deviation within 0.05 m depth bins is given in Figure 5.16.

Prandtl [1925] introduced a turbulent length scale , the so called mixing length, which increases linearly with depth and has a finite surface value

$$l_m = m(z + z_0), \qquad (5.11)$$

where z_0 is called roughness length. Close to the surface this concept is adopted in the widely used turbulence closure schemes by Mellor and Yamada [1974, 1982]. However the need to include a roughness length, which in general cannot be measured, introduces an arbitrariness to the application of such models.

A linear fit to the mean values obtained from the bootstrap method has a slope $m = 0.57$ and a roughness length $z_0 = 0.2\,\mathrm{m}$ (solid line in Figure 5.16). The regression coefficient is $r = 0.97$. The slope is slightly higher than the classical van Karman constant of $m = 0.4$ (dashed line in Figure 5.16), with one possible explanation being buoyancy due to sub-surface microbubbles suppressing the mixing length closer to the surface. We shall use this result subsequently in our comparison of the Craig & Banner [1994] model to our data.

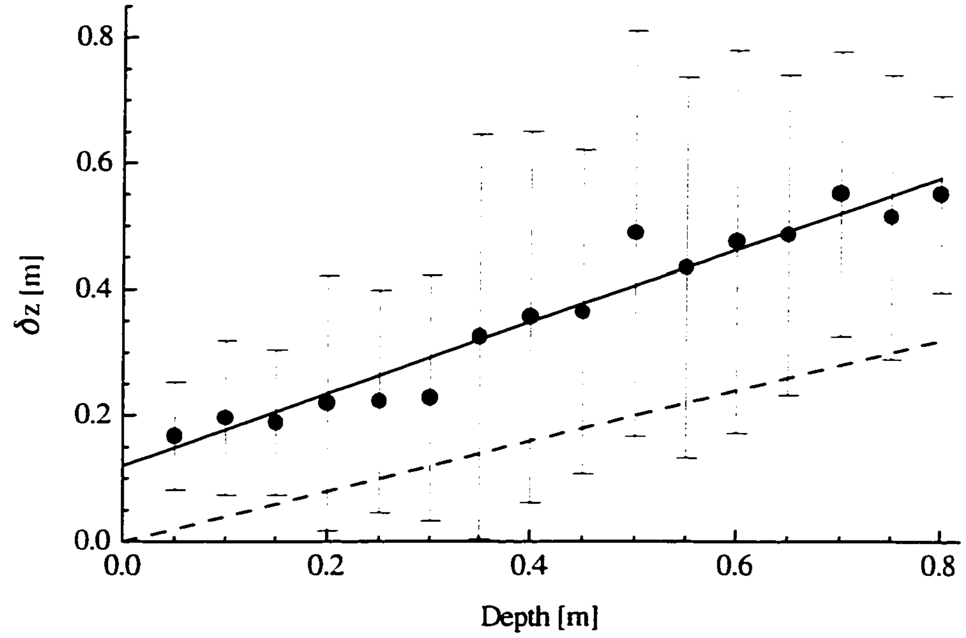

Figure 5.16: Mean values of vertical extension of temperature disturbances, obtained from 1000 bootstrap iterations of the data given in Figure 5.15b and linear fit (solid line). Wall layer mixing length is given by dashed line. Error bars represent one standard deviation.

In the case of an upward heat flux, temperatures close to the surface are lower than below. This is seen in the average temperature profile given in Figure 5.17. Prior to averaging the profiles were offset by the mean value of the deepest 0.1 m bin to adjust the cooling trend during the deployment. Vertical gradients increase gradually as the surface is approached with the temperature at 0.1 m depth being 3.2 mK colder than at 1.8 m depth. However, within the top 0.1 m the temperature drops at least 8 mK, confirming the presence of a cold surface layer (section 5.2.1). We limited the average of the near surface temperature profile to cases without detectable air entrainment measured by the conductivity sensors during the passage of the profiler to eliminate a potential bias due to temperature fluctuations within breaking waves. Furthermore, even for the shallowest depth of 0.05 m the thermistor is guaranteed to be completely immersed within the water. The measurement error of ±2 mK is estimated from the standard deviation of all values at one depth divided by the square root of the number of profiles. This mean temperature profile is the basis for the calculation of the diffusivity profile in section 6.1.

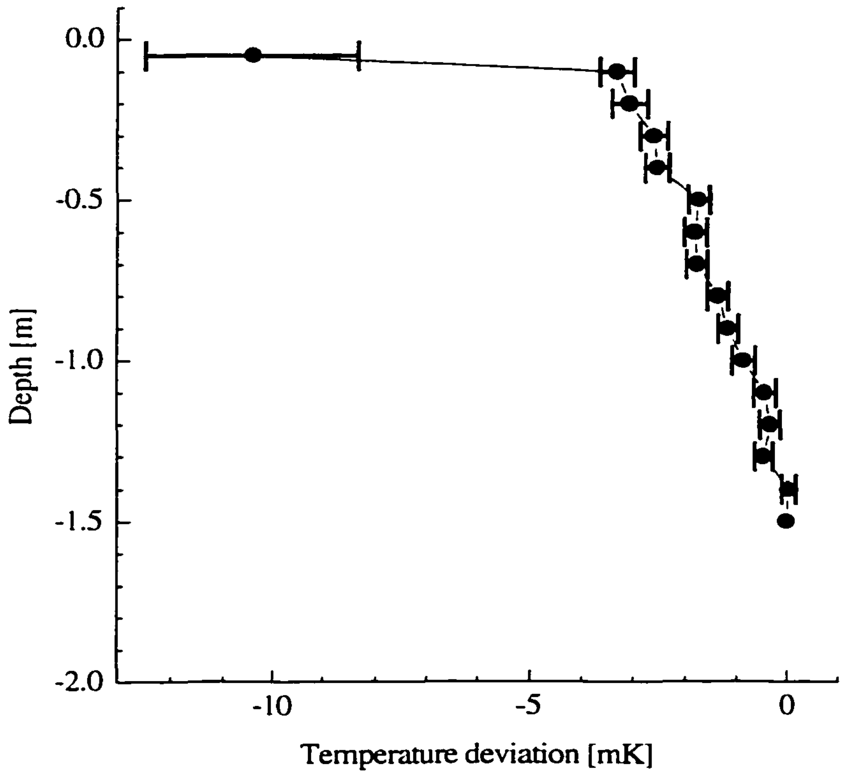

Figure 5.17: Average temperature profile during 18/04/95 deployment, expressed as deviation from mean value within the deepest 0.05m bin. Prior to averaging the profiles were sub-sampled to 0.1 m steps.

5.2.3 Temperature fluctuations associated with Langmuir circulation

The thermal structure of Langmuir circulation has been the subject of a few field observations in lakes [Myer, 1969; Thorpe & Hall, 1982] and the ocean [Thorpe & Hall, 1987] where under stable conditions on average warmer water was found within downwelling regions. During the early observations by Myer [1969], when stratification was strong with surface water up to 0.5 K warmer than water at 7 m depth, a temperature increase of more than 0.1 K was observed beneath wind streaks. Thorpe and Hall [1982, 1987] describe measurements made with a towed spar fitted with thermistors and sonars. They found temperature fluctuations of 10 mK to 20 mK coincident with bubble clouds, but report temperature and sonar data to be poorly correlated in detail.

Combined observations of the bubble field and temperature at 6.5 m depth made with upward looking sonars and a recording thermistor, respectively, clearly demonstrate the link between temperature fluctuations and Langmuir convergences with colder water within convergences and warmer water in between [Farmer *et al.*, 1997].

Time series of the instrument position (Figure 4.9) as well as visual observations reveal that our instrument is drifting roughly perpendicular to the wind direction, thus traversing adjacent Langmuir convergences. Therefore the array of fixed thermistors monitors potential temperature gradients across Langmuir cells.

The following analysis is based on data acquired during the 18/04/95 deployment. A very accurate calibration was achieved by adjusting offsets of the fixed thermistors relative to the temperatures observed with the profiling thermistor when passing an individual thermistor. The SeaBird thermometer at 1.8 m depth, with a typical drift of less than 4 mK/year, is used as an absolute reference.

A segment of the temperature record at 1.8 m is given in Figure 5.18a. Beside the cooling trend of approximately -40 mK/h several fluctuations of order 10 mK and a few minutes duration are seen. We anticipate these fluctuations occur when the instrument drifts through a Langmuir convergence zone. These fluctuations are extracted in the following manner: A time series of maximum temperature deviation between each data point and data within the previous 60 s is constructed. Temperature events are defined as deviations exceeding a threshold of three standard deviations within a 30 minutes bin, and time and magnitude of the events are recorded. The segment of maximum temperature deviation corresponding to data shown in Figure 5.18a is given in Figure 5.18b along with detected temperature events. This detection scheme not only determines times of large temperature fluctuations but also extracts their magnitudes accurately, and is therefore preferred over more common detection schemes utilizing high pass filtered time series.

Temperatures of all five thermistors of the event occurring at minute 25 in Figure 5.18a are shown in Figure 5.19. Time series of the top four sensors have been lowpass filtered and resampled to match the sampling frequency of 2 Hz of the deepest sensor. The temperature event can be seen at all five levels. The duration is approximately 90 s, which translates for a mean instrument drift speed of 0.05 m/s into 4.5 m width of the convergence zone. The magnitude of the temperature deviation decreases with depth from approximately 17 mK at the shallowest sensor to 11 mK at 1.8 m depth. Vertical

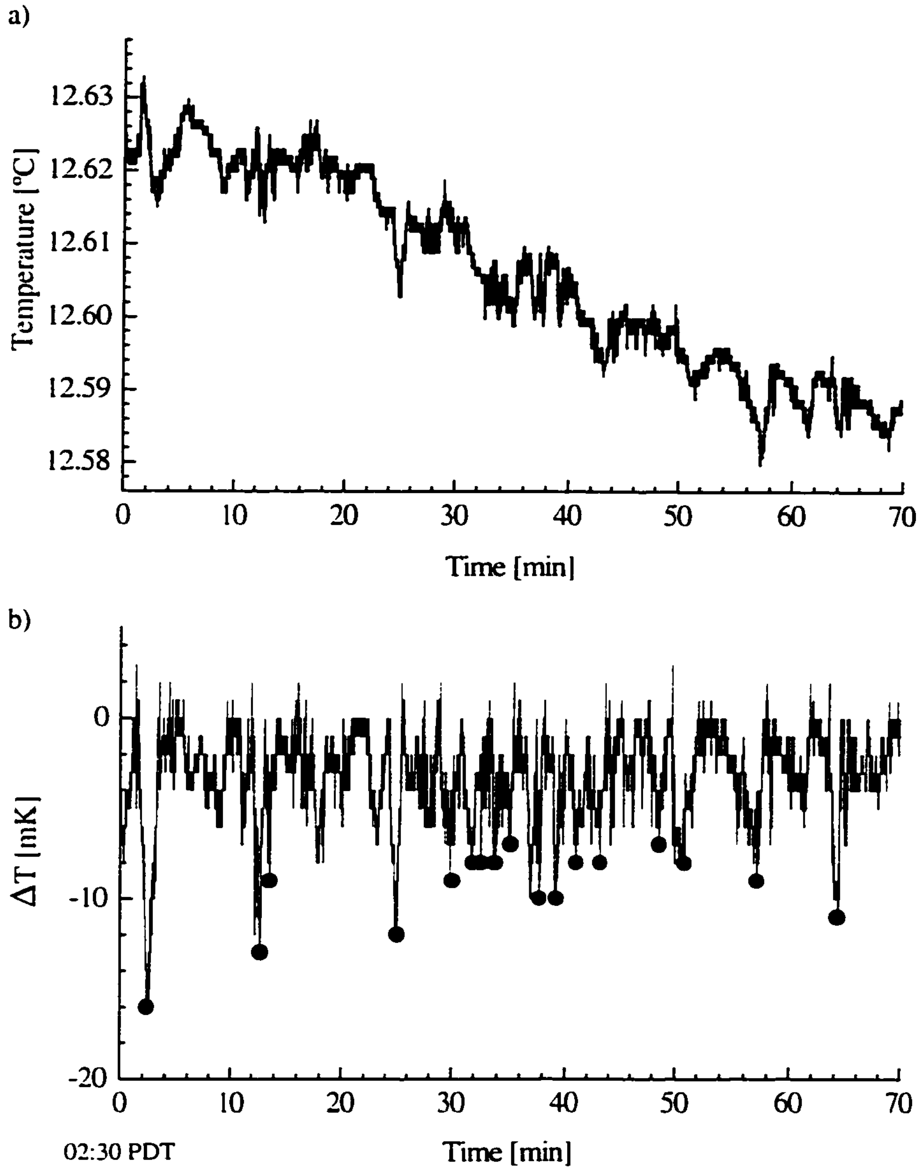

Figure 5.18: a) Temperature record at 1.8 m depth starting at 18/04/95, 0230h. b) Maximum temperature deviation within previous 60 s (line) illustrating detection scheme of temperature events and detected temperature events (circle). (Same time interval as in a)).

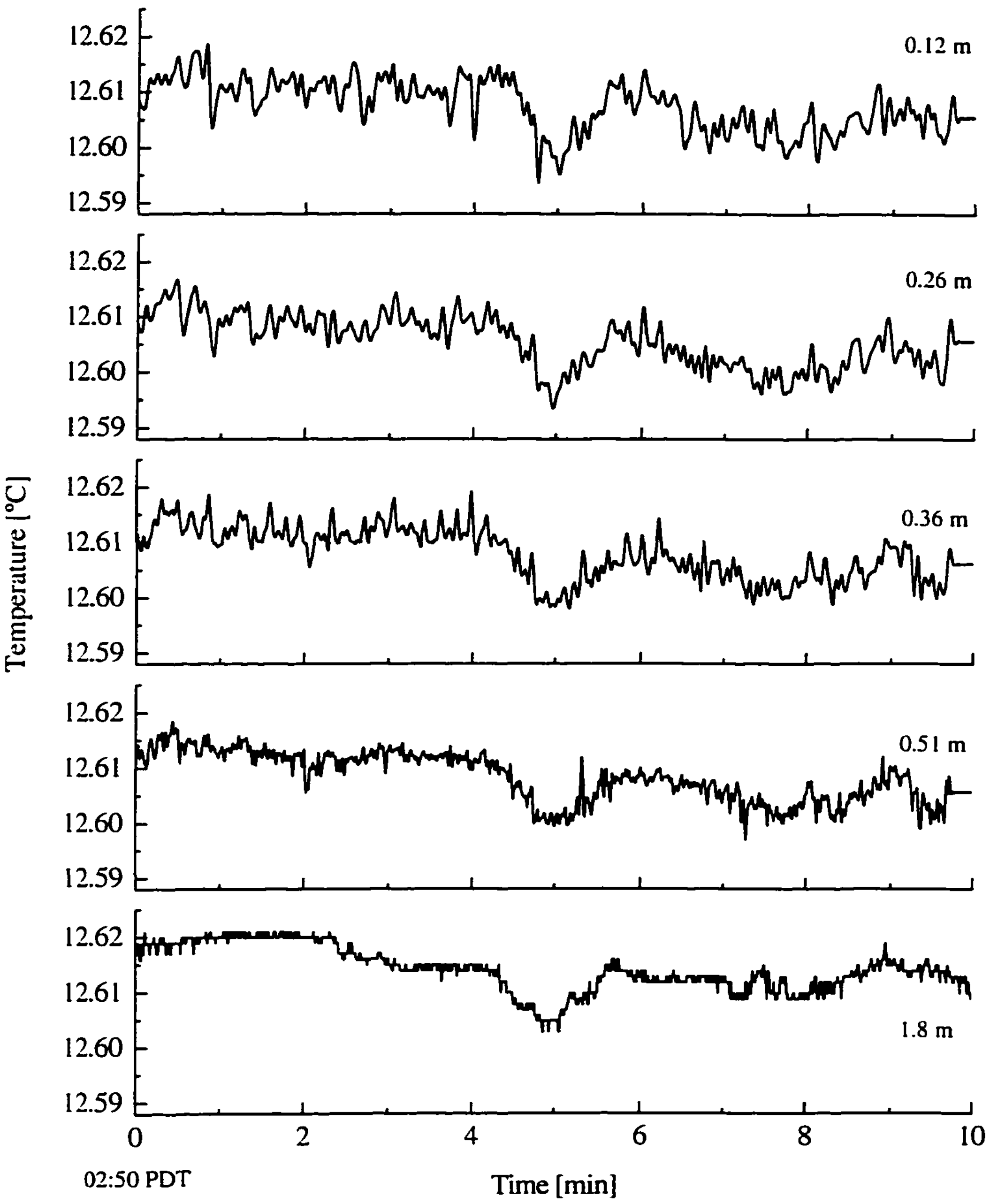

Figure 5.19: Temperature at five depths showing temperature fluctuation associated with Langmuir convergence zones.

temperature gradients are greatest close to the surface and a large temperature variability at the three shallowest sensors is obtained. Note that for this analysis the temperature record within breaking events, as defined by periods of air fraction greater than 0.08, is adjusted to values prior to the onset of breaking. The standard deviation of fluctuations with frequency higher than 0.05 Hz, thus excluding temperature fluctuations within Langmuir convergences, is 3.1 mK at 0.12 m depth but only 0.9 mK at 1.8 m depth.

Using the method described above 119 temperature events were detected within the temperature record at 1.8 m, and their magnitude was extracted at all five sensor depths in the same way. Generally, the average value over 60 minutes, shown in Figure 5.20, decreases with depth, although differences within the top 0.5 m are too small to distinguish between individual sensor depths. The record at 6.5 m depth was obtained with a self contained thermistor attached to the rubber cord of the acoustic package deployed in the vicinity and is therefore only suitable for stochastic comparisons. The time evolution of the magnitude of the temperature differences roughly follows the trend of the air-sea heat flux. Magnitude and depth dependence of these temperature signals are subject to further analysis in section 6.3.

To test the hypothesis that these temperature events occur within Langmuir convergence zones, the spatial separation of bubble clouds along the instrument drift path and the corresponding spatial separation of temperature events are compared. Since observations of the bubble field and observations of the temperature field are obtained with two separate instruments at slightly different locations the comparison can be only of statistical nature.

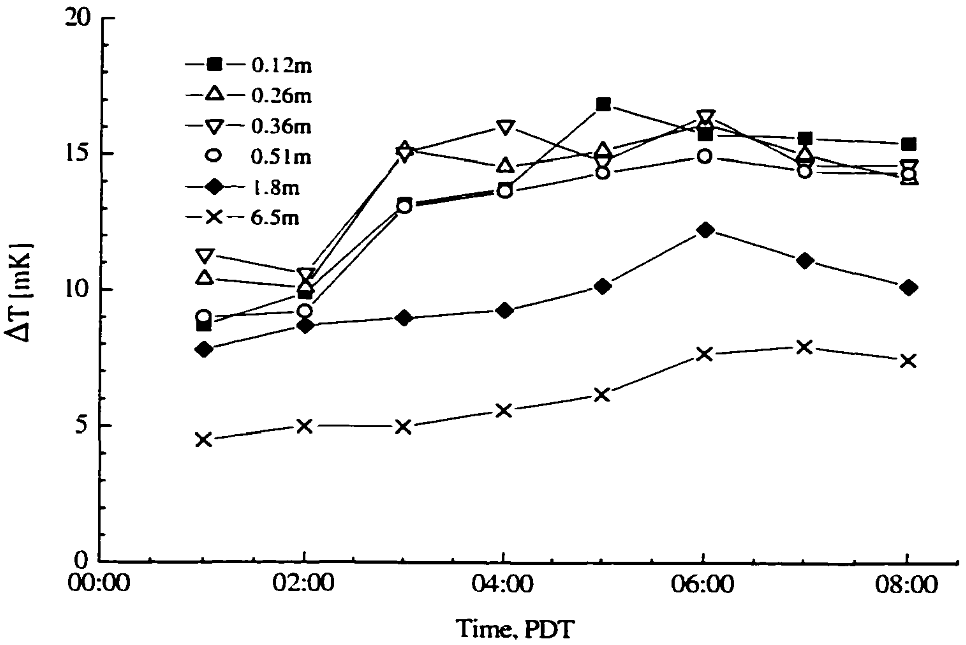

Figure 5.20: Mean magnitude of temperature fluctuations associated with Langmuir convergence zones.

On 18/04/95 sonar sidescan images were collected with the acoustic platform for a one hour period every four hours, and overlapping observation periods of bubble clouds and temperature field are 0007h - 0107h, 0407h - 0507h and 0808h - 0825h.

Langmuir cells are observed by SeaScan, which drifts with a speed of 0.02 m/s to 0.08 m/s through the mixed layer, and hence across individual Langmuir cells. This drift speed, evaluated from horizontal Doppler measurements, was provided as hourly averages by V. Polonichko (IOS, UVic). In order to translate these measurements into a drift between our surface drifter and Langmuir cells the relative motion between the drifter and SeaScan has to be accounted for. Drift paths of the two instruments are known from the ARGOS positioning system (Figure 5.21). For each instrument these positions are converted into a time series of E-W and N-S components of the instrument drift. Hence, the sum of the drift velocities of SeaScan relative to the mixed layer and the earth-referenced drift velocity of SeaScan yields the earth referenced motion of Langmuir cells. The drift velocity of our surface drifter relative to Langmuir cells is then given as the difference between earth-referenced drift velocities of our instrument and earth-referenced velocities of the mixed layer drift. Calculations are done separately for the $E-W$ component u and the $N-S$ component v for hourly values. The results are 0.02 m/s< u < 0.06 m/s and 0.06 m/s < v < 0.13 m/s.

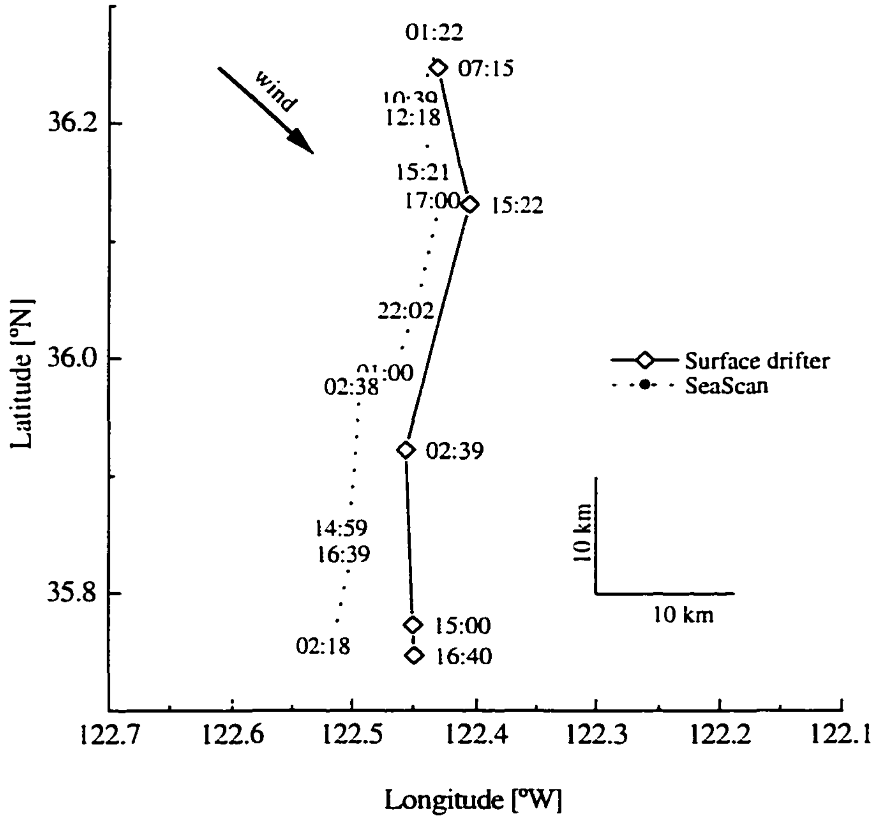

Figure 5.21: ARGOS positions of the surface drifter (solid line) and the acoustical platform SeaScan (dotted line) for 18/04/95 - 19/04/95. Times are in UTC.

Under the assumption that individual sidescan images are representative of the bubble cloud, seven images are chosen for simulation of the instrument drift across the bubble field. These images were collected from the beginning, middle and end of each overlapping recording hour and were provided by V. Polonichko (IOS, UVic).

For each image 10000 realizations of the instrument drift with random starting locations are obtained, and the time intervals between crossings of Langmuir convergences are recorded. Langmuir convergences are defined as locations with backscatter intensities above a certain threshold. Since the distribution of the background backscatter intensity can be assumed to be gaussian, but non-gaussian within convergence zones, the threshold is equal to the intensity value where the distribution of the observed backscatter intensity deviates from a normal distribution (V. Polonichko, personal communication).

The comparison of the distribution of periods between successive temperature events at 1.8 m depth and periods of successive encounters of Langmuir convergence zones along simulated drift paths is given in Figure 5.22. Beside a higher frequency of occurrence of periods less than 90 s in the temperature record, which results most likely from the instrument drifting into a single convergence zone several times, a good agreement between the two distributions exists. This confirms our detection scheme of temperature events and the interpretation of these events occurring within Langmuir convergence zones.

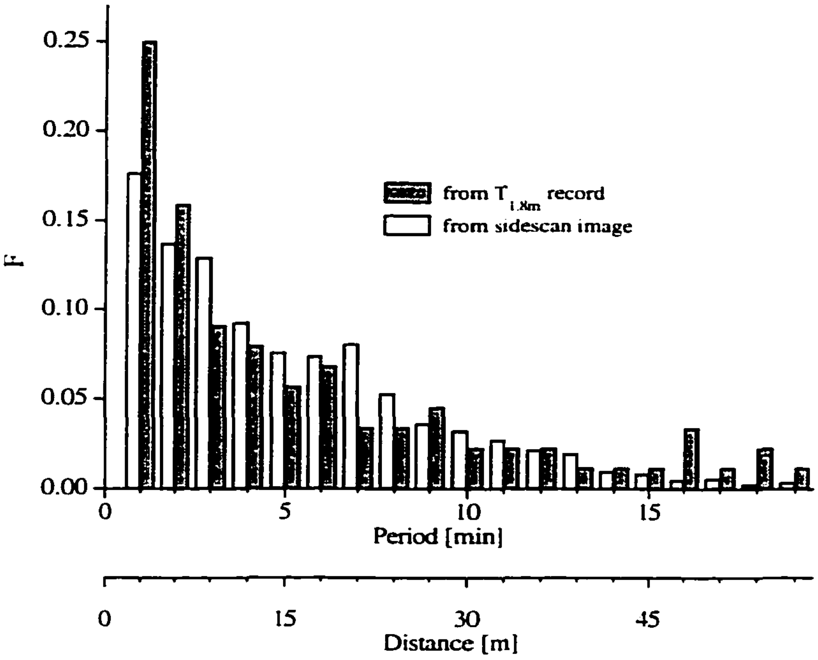

Figure 5.22: Distribution of time periods between successive temperature events (gray) and time periods between crossings of Langmuir convergences as obtained from simulated drift paths through observed bubble fields (open bars). Second axis indicates distances according to a mean instrument drift speed of 0.05 m/s.

6. Discussion

Our data analysis given in chapter 5 identifies diffusion, which is governed by wind stress and breaking wave activity, and advection due to Langmuir circulation as the two dominant processes determining the near surface temperature structure. For the small temperature fluctuations encountered, heat is essentially a passive tracer. (The Monin-Obukhov length for the 18/04/95 deployment is of order 100 m and the Hoenikker number ranges between 2×10^{-3} and 8×10^{-3}, which is well below the critical value for convection playing a significant role in Langmuir circulation generation). Hence, the temperature field is specified by the advective diffusion equation

$$\frac{\partial \tilde{\theta}}{\partial t} + \tilde{V} \cdot \tilde{\nabla} \tilde{\theta} - \tilde{\nabla} \cdot (\tilde{k}_T \tilde{\nabla} \tilde{\theta}) = 0 \tag{6.1}$$

where $\tilde{V} = (\tilde{u}, \tilde{v}, \tilde{w})$ describes the three-dimensional flow field, $\tilde{k}_T(z,t)$ is the thermal diffusivity and $\tilde{\theta}$ is the potential temperature. The boundary conditions are a prescribed heat flux Q at the surface and a given temperature $\tilde{\theta}$ at the bottom of the mixed layer of depth H

$$\frac{\partial \tilde{\theta}}{\partial \tilde{z}} = \frac{Q}{\rho c_p \tilde{k}_T}, \quad \tilde{z} = 0; \qquad \tilde{\theta} = \tilde{\theta}, \quad \tilde{z} = H \tag{6.2}$$

The flow field can be specified based on observations and the air-sea heat flux is measured independently. The diffusivity profile $\tilde{k}_T(z,t)$, which is the only unknown quantity, describes the turbulence field. This is the main focus of this section.

Calculation of the diffusivity field involves inverting the advective diffusion model, a rather complicated procedure. The alternative approach, which is taken in this thesis, is to apply existing models for the diffusivity and evaluate results of the modeled temperature field against our observations. Inherent in this trial and error process is the assumption that the turbulence field, as expressed in the diffusivity profile, and the flow field are separable. Laboratory experiments [Rapp & Melville, 1990] showed that high turbulence levels introduced by wave breaking decay within approximately two wave periods, which yields for our conditions a decay time of 20 s to 30 s. Maximum horizontal velocities in Langmuir circulation are of order 0.05 m/s [V. Polonichko, personal communication] and cell widths are of order 10 m. Therefore, the advective time scale is at least one order of magnitude larger than the diffusive time scale allowing for a separate assessment of the two individual processes.

Measurements of the vertical fine structure of the temperature field (Figure 5.15) motivate the use of a mixing length type model to evaluate near surface diffusion. The simplest mixing length model was developed for the flow along a solid wall and is given in Equations 2.3 and 2.4. However, recent measurements of energy dissipation in the surface layer [Drennan *et al.*, 1992; Agrawal *et al.*, 1992; Anis & Moum, 1992; Osborn *et al.*, 1992; Anis & Moum, 1995] indicate enhanced turbulence levels close to the surface, attributed to wave breaking [Drennan *et al.*, 1992], which also implies a larger near surface diffusivity. In an attempt to model the wave stirred surface layer Craig & Banner [1994] modified a conventional 1-dimensional turbulence closure model to incorporate a boundary layer of wave-breaking enhanced turbulence matched to a law of the wall layer beneath. This model will be utilized in estimating the diffusivity profile.

Individual windrows can be traced for up to 30 minutes on successive sonar side scan images, a time long compared to the time needed for the surface water to be advected into the downwelling region (see section 6.3.2). We therefore eliminate the time dependence in Equation 6.1 to calculate a mean steady state temperature field. However, temperature fluctuations associated with breaking waves are far from steady state and time dependence of diffusivity and temperature will be included in their interpretation.

6.1 Mean diffusivity profile in a wind driven sea

Direct measurements of the turbulent transports in the ocean surface layer are commonly acquired with rising turbulence-profilers, resulting in intermittent sampling with poor horizontal and temporal resolution. Analysis of these measurements could not reliably quantify the structure of the turbulence in the near surface layer at high sea states. In this project we take the alternative approach, relating the turbulent flux Q_C to the bulk quantity C via the eddy exchange coefficient K_C.

$$Q_C = K_C \frac{dC}{dz} \tag{6.3}$$

The main advantages are high spatial and temporal resolution. However, measurement uncertainties can introduce large errors for very small gradients, and the concept fails for counter gradient mixing. Moreover, in the presence of advection the profile of the quantity C is affected by diffusion and the advective motion, and the coefficient K_C is more appropriately called an *apparent* eddy exchange coefficient.

In the case of vertical heat transport the apparent eddy diffusivity k_T is given by

$$k_T(z) = \frac{Q(z)}{\rho c_p} \left(\frac{dT}{dz} \right)^{-1} \tag{6.4}$$

which can readily be evaluated if heat flux and temperature profiles are known. This is done for all complete upward profiles, with the gradient estimated as temperature differences over 0.1 m and between 0.05 m and 0.1 m depth as the uppermost value. Since all profiles were taken during night no depth dependence of the heat flux has to be considered, which would be introduced by penetrating solar radiation. The apparent diffusivity profiles for measurements within Langmuir convergence zones, as defined by the presence of low frequency temperature fluctuations (section 5.2.3), and in between convergences are given in Figure 6.1. The diffusivity increases by a factor of 10 within the top 1.6 m, with a near surface value of roughly 2×10^{-3} m^2/s. As water at the surface is advected by Langmuir circulation it is exposed to the heat flux, and hence greatest temperature anomalies are found within the upper part of the convergence regions. Since downwelling velocities are small near the surface, this yields large vertical gradients, and the apparent diffusivity is smallest in the near surface region of the downwelling zones. Only 15% of the profiles were taken within ±10 s of the instrument passing through the maximum of a temperature fluctuation, resulting in a wide scatter of the apparent diffusivity in convergence zones. Nevertheless, the general tendency of smaller apparent diffusivities in convergences can be seen. Furthermore, apparent diffusivities outside convergences are larger than predicted by wall layer scaling, with increasing discrepancy closer to the surface.

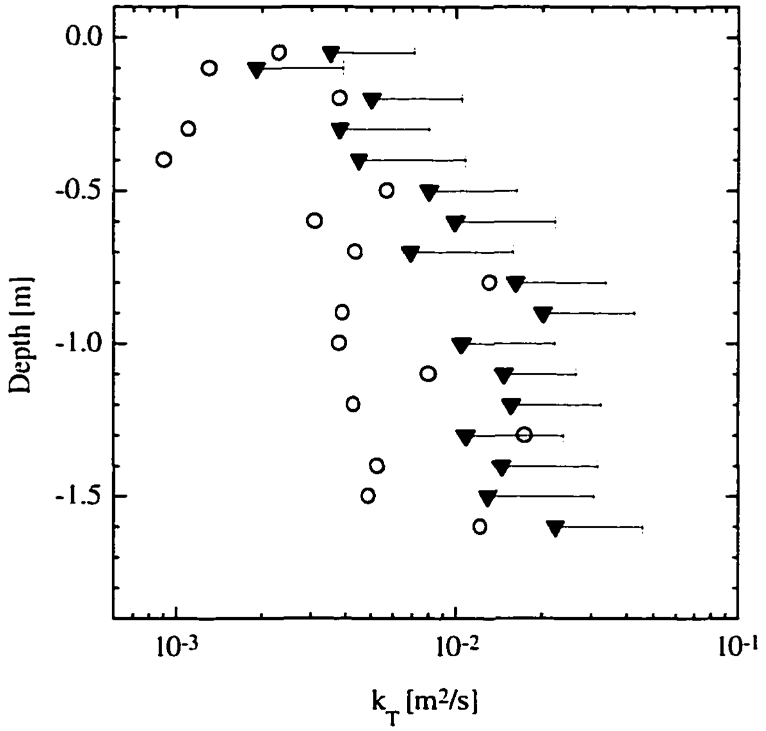

Figure 6.1: Profiles of apparent diffusivities inferred from temperature profiles in the vicinity of Langmuir convergence zones (open circle) and in between (triangle).

The Craig & Banner [1994] model of a wave stirred near surface turbulence field is described by the following model equations

$$\begin{aligned} \frac{\partial u}{\partial t}-\frac{\partial}{\partial z}\left(A\frac{\partial u}{\partial z}\right)&=f\,v \\ \frac{\partial v}{\partial t}-\frac{\partial}{\partial z}\left(A\frac{\partial v}{\partial z}\right)&=-f\,u \end{aligned} \tag{6.5}$$

The boundary conditions are

$$\begin{aligned} &A\frac{\partial u}{\partial z}=u_*^2\,;\ \frac{\partial v}{\partial z}=0; && \text{at } z=0 \\ &u=0;\ v=0; && \text{at } z=-H \end{aligned} \tag{6.6}$$

where u, v are horizontal velocity components, f the coriolis parameter, H is the depth of the model and A is the eddy viscosity, which has to be determined by the turbulence closure model.

The boundary conditions describe a stress at the water surface equal to the wind stress, which is assumed to be in the same direction as u, and no slip at the seabed. The eddy viscosity has the form

$$A=l\,q\,S_M \tag{6.7}$$

where q is the turbulent velocity, S_M is a constant and l is the mixing length, defined as

$$\begin{aligned} l &= \kappa (z_0 - z) \quad \text{in the surface layer} \\ l &= \kappa (H + z + z_0) \quad \text{in the bottom layer} \end{aligned} \tag{6.8}$$

Here $\kappa = 0.4$ is the von Karman constant and z_0 the roughness length, which is a free parameter in the turbulence closure scheme. However, as shown in section 5.2.2 the measured temperature profiles provide a direct estimate of the roughness length, which in the present case is of order 0.2 m.

The turbulent velocity is given by the turbulent kinetic energy equation

$$\frac{1}{2}\frac{\partial q^2}{\partial t} - \frac{\partial}{\partial z}\left(l q S_q \frac{1}{2}\frac{\partial q^2}{\partial z} \right) = l q S_M \left[\left(\frac{\partial u}{\partial z} \right)^2 + \left(\frac{\partial v}{\partial z} \right)^2 \right] - \frac{q^3}{B l} \tag{6.9}$$

where $S_q = 0.2$ and $B = 16.6$ are further constants. The surface boundary condition incorporates the influence of breaking waves as it imposes a flux of the turbulent kinetic energy through the surface, and no energy flux is assumed at the bottom

$$\begin{aligned} &\frac{1}{2} l q S_q \frac{\partial q^2}{\partial z} = \bar{c}_p u_*^2 \quad && \text{at } z = 0 \\ &\frac{\partial q^2}{\partial z} = 0 && \text{at } z = -H \end{aligned} \tag{6.10}$$

where $\bar{c}_p = 0.7$ m/s is the effective phase speed of waves acquiring energy from the wind [Gemmrich, *et al.*, 1994].

In Craig & Banner's [1994] original formulation the surface flux of the turbulent kinetic energy is taken to be proportional to the cube of the friction velocity. However, the energy from the wind enters the ocean surface layer via the wave field and is appropriately expressed as $\bar{c}_p u_*^2$ (see section 2.4). The additional kinetic energy input $\tau_s u_s$ due to skin friction τ_s and surface drift u_s is of secondary importance [Craig & Banner, 1994].

The model is solved numerically by finite differences in space and time, where the space coordinate first gets converted as $y = \int_0^z l(z')^{-1}\, dz'$ to increase the resolution close to the boundaries. The code for this numerical solution was kindly provided by Dr. P. Craig (CSIRO, Division of Oceanography, Hobart, Tasmania) and only the above mentioned modifications to the model had to be incorporated. More details on the implementation of the numerical scheme can be found in Craig & Banner [1994].

The constants S_M, S_q and B are set at the same values as specified by Mellor & Yamada [1982], which assures the model to collapse onto the classical wall layer scaling in the limiting case of steady state and shear production balancing dissipation (*i.e.* left hand side of Equation 6.9 is equal to zero). There is no influence of the presence of the bottom on the surface layer for a model depth of H = -200 m or deeper, and H is set to be -200 m. This leaves the roughness length z_0 as the only free model parameter.

In the following, this model is used to calculate the eddy diffusivity profile $k_T(z)$, with the assumption of a turbulent Prandtl number $\mathrm{Pr}_t = A\, k_T^{-1} = 1$, *i.e.* $k_T(z)$ is calculated according to Equation 6.7.

Figure 6.2 gives a comparison of diffusivity profiles for different roughness lengths. The profiles, computed for a friction velocity of 0.02 m/s , are nondimensionalized and are presented in wall layer coordinates [Soloviev, *et al.*, 1988], which emphasizes the presence of a wave stirred surface layer. Close to the surface the model diffusivity for $z_0 = 0.05\,m$ is approximately 40 times larger than predicted by wall layer scaling; this ratio increases to over 500 for $z_0 = 0.8\,m$. Similarly, the wave enhanced layer deepens by a factor of 8 over this range of roughness lengths.

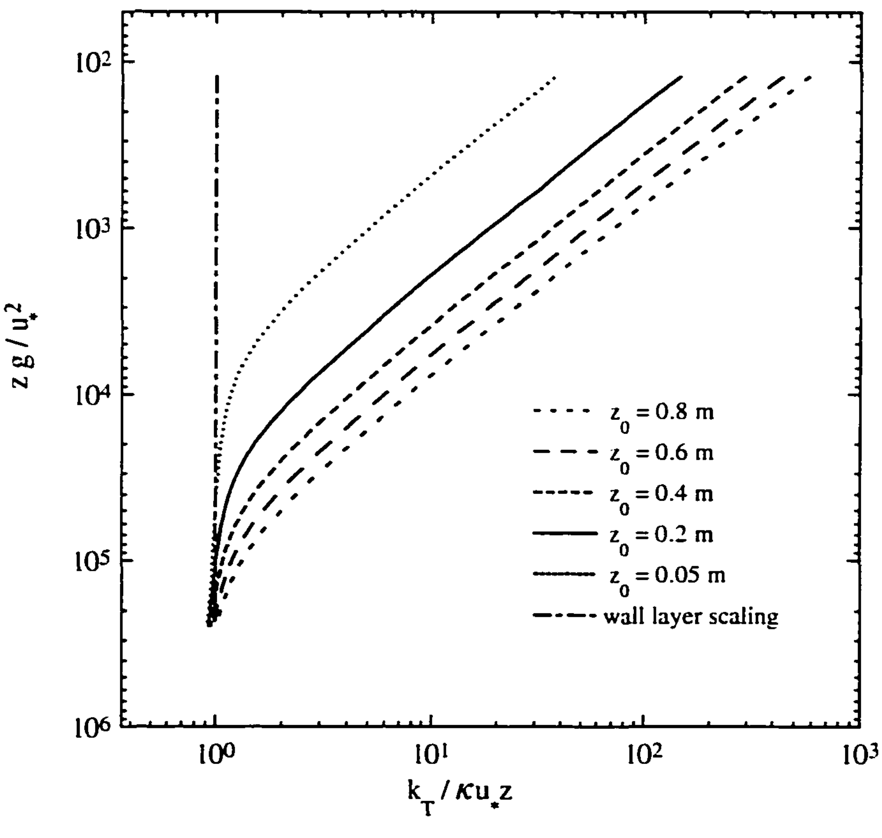

Figure 6.2: Diffusivity profiles obtained from Craig & Banner [1994] model, and their dependence on surface roughness length.

The *ad hoc* formulation of the roughness length is rather arbitrary. However, the analysis of the temperature profiles provide an estimate of $z_0 = 0.2$ m. Furthermore, the energy dissipation specified by the model depends on the roughness length, and hence the energy budget can be used as a criteria for determining z_0. The model specifies the turbulent kinetic energy input by breaking waves as the major energy source, which has to balance the depth integrated dissipation D.

$$D = E_{in} \tag{6.11}$$

The dissipation profile (Figure 6.3) is given by the second term on the right of Equation 6.9

$$\varepsilon = \frac{q(z)^3}{B\,l(z)} \qquad (6.12).$$

Dissipation rates fall off very rapidly with depth. Approximately 88% of the total dissipation occurs within the upper two metres. The total dissipation in the mixed layer

$$D = \int_0^{H_{ML}} \varepsilon(z)\,dz\,, \tag{6.13}$$

where H_{ML} is the mixed layer depth, is calculated for several mixing lengths by trapezoidal integration. The near surface dissipation grows for increasing mixing lengths, and the ratio between energy input and total dissipation $R = E_{in} / D$ decreases. For

$z_0 = 0.3$ m this ratio is $R = 0.39$. Decreasing the roughness length to $z_0 = 0.25$ m yields $R = 0.58$. The closest balance between energy input and dissipation is achieved for a roughness length $z_0 = 0.2$ m where 94% of the total dissipation is accounted for by the energy transfer from the wind to the waves. This constraint on the roughness length is not part of the model formulation, but it should be used as a consistency check and allows for a first estimate for z_0.

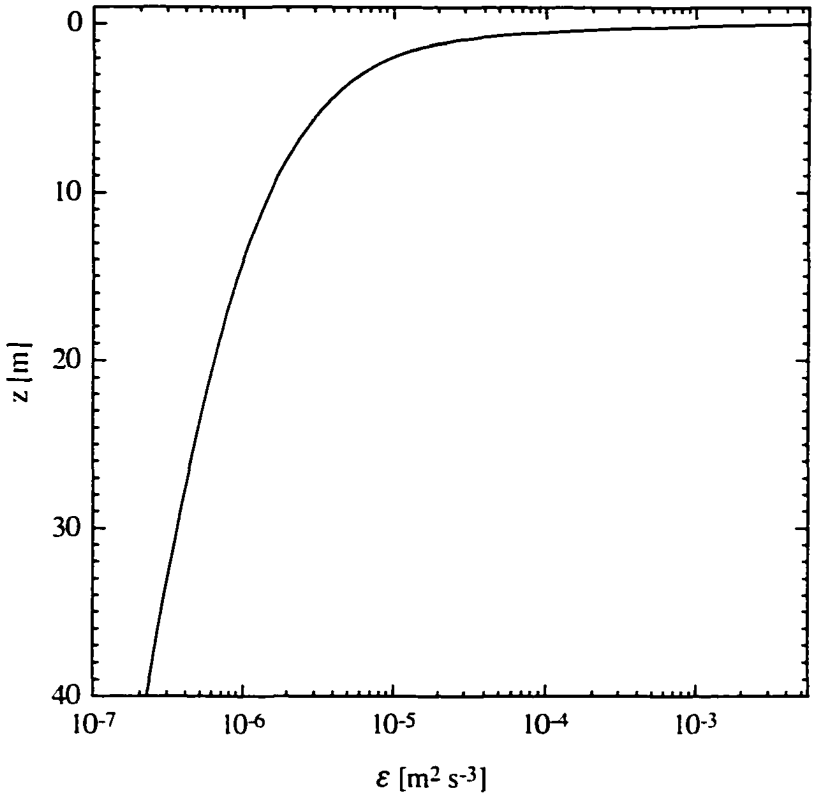

Figure 6.3: Dissipation profile according to Craig & Banner [1994] model, for $z_0 = 0.2$ m and $u_* = 0.02$ m/s

A further estimate of z_0 can be obtained from a comparison of the modeled diffusivity profiles with the diffusivities inferred from the temperature profiles. However, as pointed out earlier our measurements yield only an apparent eddy diffusivity, which is composed of a diffusive and an advective component. Therefore, a valid comparison has either to remove the advective component from the measured data or include advection in the model. In order to account for advection the near surface temperature field is computed with the steady state advective-diffusion model from which a profile of the apparent model diffusivity is calculated according to Equation 6.4. This apparent model diffusivity can then be compared to the apparent diffusivity inferred from the temperature profiles.

As will be discussed in more detail in section 6.3.3, the advective diffusion model was run for representative model parameters and an average apparent diffusivity profile for different input diffusivity profiles, relating to various roughness lengths, is computed. The comparison is given in Figure 6.4. Again, the observations, *i.e.* the mean of all diffusivity profiles between 0200h and 0800h, exhibit a wave enhanced surface layer with diffusivities up to 20 times larger than wall layer scaling predicts. This feature is also well captured by the Craig & Banner [1994] model diffusivities.

The above discussed energy balance criteria as well as our analysis of the temperature profiles (section 5.2.2) indicate a roughness length of order 0.2 m. Hence, we evaluate model outputs for roughness lengths varying from 0.1 m to 0.4 m against our observations. The mean relative error is defined as (Schönwiese, 1985)

$$\delta = \left[\frac{1}{N(N-1)} \left(\sum_{n=1}^{N} \frac{X_i - M_i}{M_i} \right)^2 \right]^{1/2} \tag{6.14}$$

where in our cases X_i stands for the mean observed apparent diffusivity at a given depth, M_i is the corresponding apparent model diffusivity and $N = 17$ is the number of depth bins. Similarly, a mean absolute error is defined as (Schönwiese, 1985)

$$\Delta = \left[\frac{1}{N(N-1)} \left(\sum_{n=1}^{N} X_i - M_i \right)^2 \right]^{1/2} \tag{6.15}$$

The error estimates of the normalized apparent diffusivity for four different roughness lengths are given in Table 6.1

z_0 [m]	δk_T	Δk_T
0.1	0.13	0.61
0.2	0.09	0.25
0.3	0.10	0.52
0.4	0.13	1.12

Table 6.1: Relative and absolute error of mean apparent model diffusivity normalized by law of the wall scaling for different roughness lengths.

A roughness length of 0.2 m provides the best fit , *i.e.* least mean relative error and smallest mean absolute error, between apparent model diffusivities and our observations (Table 6.1). For this roughness length the advective component is insignificant in the upper 0.5 m, however at the bottom of the profile the apparent diffusivity is roughly twice as large as would be the case if no advection was present. This result is in agreement with the roughness length derived from the fluctuations of the measured temperature profiles and provides a consistent description of the model energy balance.

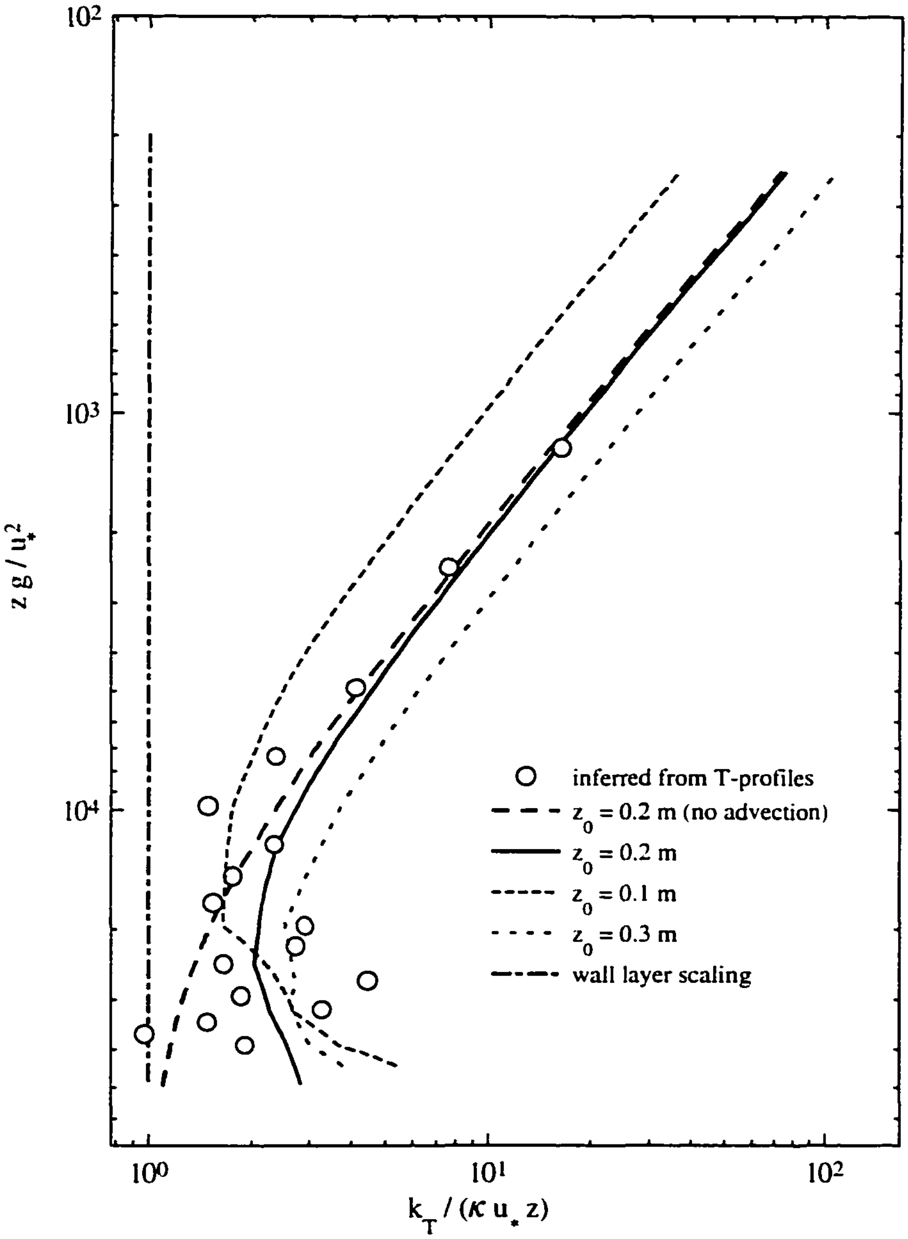

Figure 6.4: Comparison between observations and model diffusivity profiles. Also shown is the modification of the diffusivity profile due to the advective component in Langmuir circulation (for z_0 = 0.2 m only).

If it is accepted that the near surface enhanced turbulence is generated by breaking waves, the length scale of this turbulence has to be related to the wave properties. Craig & Banner [1994] suggest the roughness length to be comparable to the wave amplitude, and by analyzing wave tank data Craig [1996] concludes tentatively the magnitude of the roughness length being approximately one sixth of the wave length, or roughly the inverse of the wave number.

Even by accounting for the size of breaking waves being less than the size of the dominant wave (section 5.1.4) these estimates predict a roughness length of several metres. However, as noted by Craig & Banner [1994], comparison between their scaling and the empirical dissipation law by Drennan *et al.* [1992] for the Lake Ontario data leads to values of z_0 between 0.1 m and 1.0 m.

The motivation for the roughness length, although on a purely mathematical basis, is to provide a minimum value of the mixing length. From a physics point of view the minimum mixing length is introduced by the size of the actively stirred surface layer. In analogy to the case of grid stirred turbulence, where this length scale would be the stroke of the grid motion, the oceanic length scale is the distance large air bubbles move through the water column, and hence the depth of large fractional air entrainment. Comparison with our conductivity measurements (section 5.1.3) shows the assumed roughness length of $z_0 = 0.2$ m agrees remarkably well with the depth of air entrainment. and the observed vertical temperature fluctuation

We therefore conclude the Craig & Banner [1994] model with a roughness length of 0.2 m and a surface energy flux according to Equation 6.10 predicts the near surface diffusivity profile correctly, and this model with the specified parameters serves as a basis for further model analysis of the near surface temperature field.

6.2 Evolution of temperature and diffusivity profile beneath breaking waves

In a first order estimate a breaking wave can be assumed to homogenize the temperature in the surface layer almost instantaneously, at least to the depth L_w of observed large fractional air entrainment. In the presence of a surface heat flux a near surface temperature gradient will evolve with time. A spilling breaker entrains water from a thin surface layer into its whitecap. It is this accumulation of water of anomalous temperature occurring during this process which results in the observed strong temperature signal within breaking waves.

The evolution of the temperature gradient in the top few centimetres is governed by the time scale of the periods between breaking events and to a first approximation advection due to Langmuir circulation can be neglected. Hence, this process is described by the time dependent diffusion equation

$$\frac{\partial T}{\partial t}-\frac{\partial}{\partial z}k_T(t,z)\frac{\partial T}{\partial z}=0 \qquad (6.16)$$

with the boundary conditions

$$\frac{\partial T}{\partial z}=\frac{Q}{\rho c_p\, k_T(t,0)}\,, \quad z=0$$

$$T=T_0\ ,\ z=L_w \tag{6.17}$$

where the diffusivity is a function of depth and time. While the depth dependence is well represented by the mean diffusivity profile as specified in the model in section 6.1, the temporal evolution has still to be quantified. Any specified time dependence of the diffusivity can then be tested by comparing modeled temperature gradients and observed temperature anomalies within breaking waves.

Initially, the bubble injection and subsequent rising of bubbles cause a large diffusivity. The duration of this first stage is roughly 3 seconds, estimated from an injection speed of 0.3 m/s, a bubble rise speed of 0.1 m/s, corresponding to a bubble diameter of 1 mm [Cliff *et al.*, 1978] and an injection depth of 0.25 m. Following this active stage of generation the turbulent kinetic energy decays rapidly. For isotropic turbulence the decay of the variance of velocity fluctuations $\overline{u'^2}$ is given by the following power law

$$\overline{u'^2} \propto t^{-5/2} \tag{6.18}$$

[e.g. Hinze, 1975] and the spatial scale increases as

$$\Lambda \propto t^{1/2} \tag{6.19}$$

[e.g. Hinze, 1975]. Hence, the diffusivity $k_T \propto u\,\Lambda$ scales as

$$k_T \propto t^{-3/4} \tag{6.20}$$

Accumulation of small bubbles in the top few centimetres of the ocean surface layer can amount to air fractions as much as 10^{-4} to 10^{-3} [Monahan, 1993]. The stable stratification resulting from this bubble layer, with a Brunt-Vaisala period between 28 s and 90 s, will dampen the vertical turbulent velocity fluctuations, which will result in a faster decay than for isotropic turbulence (Equation 6.18).

In a series of wind tunnel experiments Lienhard & van Atta [1990] studied the influence of stratification on the decay of grid generated turbulence. They specify the time evolution of the ratio of the measured turbulence intensity to that which would occur at the same time if no stratification was present, which we approximate by the following least square fit

$$\left(\frac{w_0}{w'}\right)^2 \propto t^{2.2} \tag{6.21}$$

Hence, the vertical turbulent velocity component in a stable stratified flow decays as

$$w' \propto t^{-2.35} \tag{6.22}$$

and, assuming the spatial evolution of the turbulence being independent of stratification, the turbulent diffusivity in the presence of a near surface bubble layer scales as

$$k_T \propto t^{-1.85} \tag{6.23}$$

The evolving structure of the eddy diffusivity in the top few centimetres of a wind driven sea can now be composed as follows. Beneath a breaking wave injection of the turbulent kinetic energy, air entrainment and subsequent rising of bubbles cause an initially high diffusivity which persists for roughly three seconds. After this active part the wave induced turbulence decays, and the diffusivity in the upper few centimetres scales according to Equation 6.23. In the absence of a subsequent breaking event the diffusivity would relax to the background value $\kappa u_* z$, which is sustained by the shear flow. This behaviour is repeated for each breaking wave with any remaining diffusivities added to the initial value. Hence, the diffusivity beneath a breaking wave can be described by

$$\begin{aligned} &k_T(t,z) = k_0(z)\,, \quad t < 3s \\ &k_T(t,z) = \max\left(k_0(z)(t-2)^{-1.85}, \kappa u_* z\right), \quad t \geq 3s \end{aligned} \tag{6.24}$$

Data by Lienhard & van Atta [1990] support a scaling according to Equation 6.23 only for $t < 0.45\tau_{BV}$, where τ_{BV} is the Brunt-Vaisala period. However, for typical stratification values considered the diffusivity decays to wall layer scaling, which we consider as a lower bound, even for times $t < 0.4\tau_{BV}$, leaving this limitation irrelevant in our case.

The initial value $k_0(z)$ can be estimated by matching the mean value of a diffusivity time series, which incorporates diffusivities of individual breaking waves as modeled by Equation 6.24 and are spaced by the observed periods between breaking waves, to the diffusivity value $k(z)$ of the time independent model (section 6.1). This calculation is performed iteratively for 20 depth values ranging from the surface to 0.2 m depth, utilizing data from the 18/04/95 deployment.

$$k(z) = \frac{1}{N}\sum_{1}^{N}\frac{1}{\tau_b}\int_{0}^{\tau_b} k_T(t,z)\,dt \tag{6.25}$$

where τ_b is the period between breaking events and N is the total number of breaking events.

The result, normalized by the time independent diffusivity at 0.2 m depth, is shown in Figure 6.5. The diffusivity during the active part of a breaking wave is fairly uniform within the top 0.2 m and between 3.2 and 3.6 times larger than the mean diffusivity at the depth of significant air entrainment. This supports the interpretation of the surface layer being mixed vigorously to the depth of significant air entrainment, which according to our observations is limited to approximately the top 0.2 m.

Knowing the time and depth dependence of the diffusivity together with the heat flux, the evolution of the near surface temperature field can be calculated by solving Equations 6.16 and 6.17 numerically.

In order to avoid large diffusivity gradients and small values of the diffusivity, which causes irregularities in the finite element scheme, the following nondimensionalization is introduced.

$$
\begin{aligned}
T &= \frac{\tilde{T}\rho c_p \tilde{k}_{\max}}{Q L_w} \\
z &= \frac{\tilde{z}}{L_w} \\
k_T &= \frac{\tilde{k}_T}{\tilde{k}_{\max}} \\
t &= \frac{\tilde{k}_{\max}}{L_w^{\,2}}\tilde{t}
\end{aligned}
\tag{6.26}
$$

which leads to

$$
\frac{\partial T}{\partial t} - \frac{\partial}{\partial z} k_T(t,z) \frac{\partial T}{\partial z} = 0 \tag{6.27}
$$

$$
\begin{aligned}
&\frac{\partial T}{\partial z} = \frac{1}{k_T(t{,}0)}\,, \quad z=0 \\
&T = 0\,, \quad z=1
\end{aligned}
\tag{6.28}
$$

where L_w is the depth of the layer, *i.e.* $L_w = 0.2$ m and $\tilde{k}_{\max}$ the time independent diffusivity value at depth L_w.

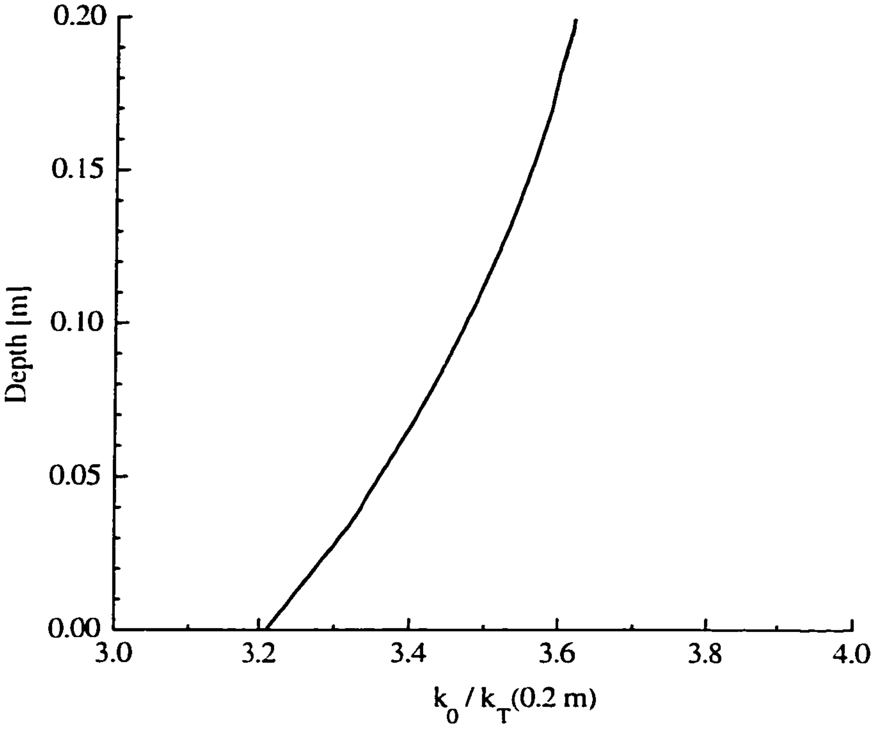

Figure 6.5: Initial diffusivity profile, normalized by mean value at 0.2 m depth, beneath a breaking wave

Temperature profiles evolving after a breaking event are calculated for a duration of 120 s in 2 s intervals. From these profiles temperature differences between a thin surface layer of thickness z_m and 0.2 m depth are calculated in order to simulate the mixing of heat in a breaking wave, as indicated by the temperature fluctuations observed beneath breaking waves. Evolution of these temperature differences for different thicknesses of the surface layer is given in Figure 6.6. The temperature difference between the surface layer and 0.2 m depth increases with time, with little temperature difference for $t < 3$. Furthermore, especially for large times the dependence on the thickness of the surface layer becomes significant.

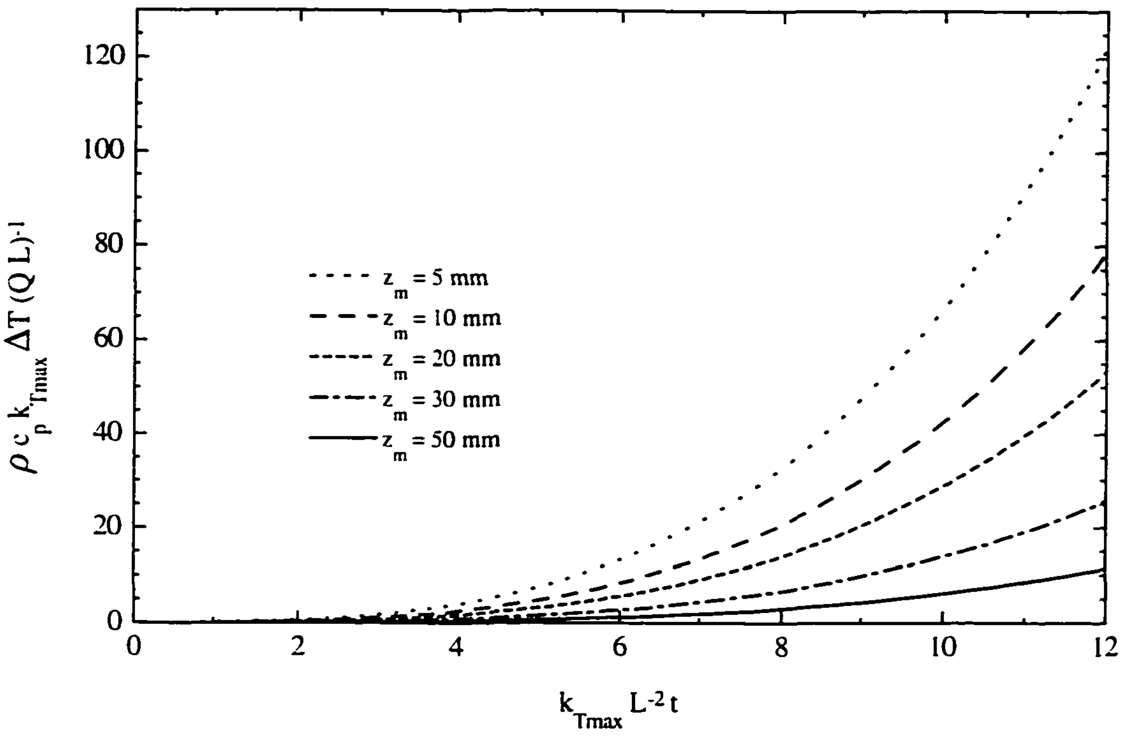

Figure 6.6: Evolution of temperature difference between mean temperature within a surface layer of thickness z_m and 0.2 m depth.

We hypothesized that a breaking wave mixes heat, which is stored within a thin surface layer of thickness z_m , down to the depth of our sensor, a process which is observed as a temperature anomaly. We emphasize here the distinction between heat stored within the molecular boundary layer, which is negligible, and the heat storage in the upper few centimetres, which is of interest here. According to the discussion above this temperature anomaly will be a function of the time elapsed since the last breaking event and the thickness of the layer which gets injected.

By mapping the temporal evolution of the vertical temperature difference on the distribution of periods of breaking events a modeled distribution of temperature anomalies within breaking waves can be obtained. Temperature anomalies are simulated for 1000 breaking events. Each event is associated with an evolution time of the near surface temperature gradient, which is calculated according to the observed distribution of periods between breaking waves. The vertical temperature difference occurring at this particular evolution time is then interpreted as the modeled temperature anomaly of this breaking wave. Comparison of the distribution of the modeled and observed temperature anomalies is given in Figure 6.7. Generally, good agreement between modeled and observed temperature anomalies is achieved. Data from the 09/12/93 deployment suggest the thickness of the surface layer which gets injected past our sensor is approximately 30 mm, whereas for the 18/04/95 deployment model results for z_m = 50 mm provide the best fit to our data. Nevertheless, both data sets support our interpretation of strong near surface gradients evolving following the homogenization of the temperature profile within a breaking wave and of breaking waves injecting water from within a thin surface layer of 30 mm to 50 mm thickness to the depth of significant air entrainment. This layer lies close to the depth resolution of our sensor, but there are indications of its presence in several of our profiles.

A necessary assumption in this model interpretation is the suppression of turbulence due to a stable stratification in the top few centimetres of the ocean surface layer, presumably provided by a layer of microbubbles. Persistent air fractions of 10^{-5} have been observed at 0.5 m depth in bubble plumes (S. Vagle, personal communication), however, no information on values in the top few centimetres is available. Still, high air fractions can only be sustained if the rising motion of the bubbles, which in the case of

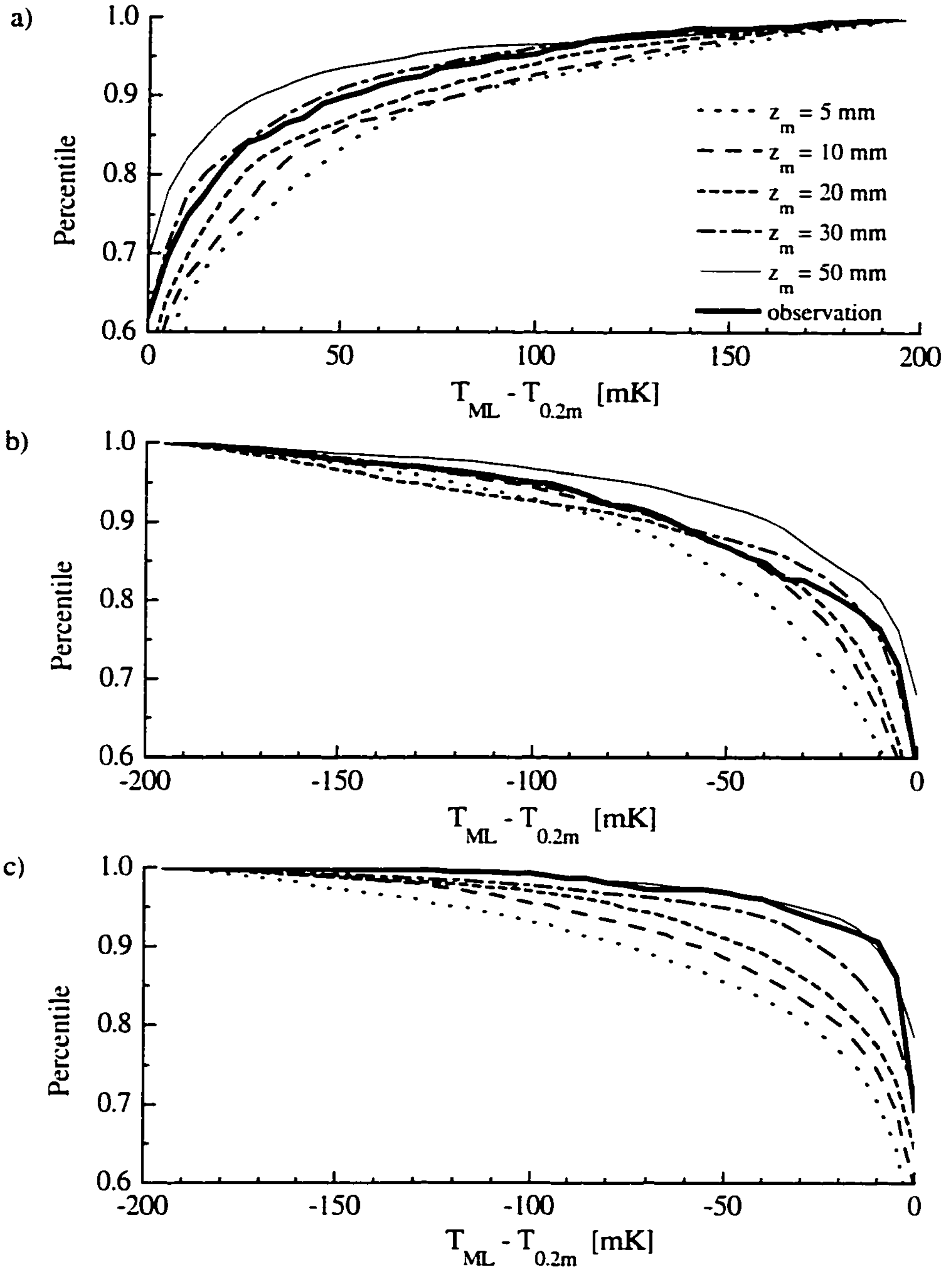

Figure 6.7: Distribution of modeled temperature differences between a surface layer of thickness z_m and 0.2 m depth and distribution of observed temperature anomalies within breaking waves. a) 09/12/93 0945h - 1745h, b) 09/12/93, 0448h - 0900h and 1900h - 2357h, c) 18/04/95, 0011h - 0820h

microbubbles of order 100 μm diameter is several mm/s [Thorpe, 1982], can be balanced by a downward motion of similar or greater magnitude. The turbulent motion itself provides downward motions larger than the rise speed of bubbles and assists in sustaining a near surface bubble layer. Furthermore, Langmuir convergences accumulate bubbles, and the strongest stratification is expected in these regions. The lack of temperature anomalies in the beginning of the 03/12/93 deployment, when no Langmuir circulation was observed, suggests the accumulation of microbubbles due to Langmuir circulation is an important mechanism in generating a pronounced thermal boundary layer.

In the case of the ocean losing heat the thermal boundary layer might become unstable, resulting in small-scale convective motions. Thermal instabilities are predicted if the Rayleigh number

$$Ra = \frac{g \alpha d^4}{\kappa \nu} \frac{dT}{dz} \tag{6.29}$$

exceeds the critical value of 657. Here α is the thermal expansion coefficient, d is the thickness of the cool layer, κ is the molecular thermal diffusivity and ν the kinematic viscosity. For the above specified cool layer of 0.03 m thickness and a temperature difference of 0.1 K the Rayleigh number takes a value of approximately 2.7×10^4, and hence, thermal convection is expected. However, the negative buoyancy of the cool layer $b_H = g \Delta\rho_H$ can be offset by the buoyancy of the microbubbles $b_B = -g \Delta\rho_B$, where $\Delta\rho_H = \alpha \Delta T \rho$ is the density difference between bulk water and the surface layer and

$\Delta\rho_B = \gamma\,\rho$ is the density perturbation resulting from an air fraction γ. For $|b_B| > |b_H|$ the stratification is stable, which yields a minimum air fraction $\gamma_{cr} = \alpha\,\Delta T$ to overcome the destabilizing effect of the cool layer. Taking 0.1 K as an upper bound of the temperature difference within the boundary layer we obtain that a near surface air fraction of 1.6×10^{-5} is sufficient to support a stable stratification even in the presence of a cool surface layer. As discussed above persistent air fractions of order 10^{-5} are expected at high sea states, and a cool thermal boundary layer can be sustained.

6.3 A steady state model of the temperature field within Langmuir circulation

As discussed in section 6.1 the turbulence model proposed by Craig & Banner [1994] provides a reasonable description of the diffusivity profile, which now can be incorporated in a simplified version of the advective diffusion model given by Equations 6.1, 6.2. While it is recognized that the pattern of Langmuir circulation includes 3-dimensional features [Farmer & Li, 1995] the basic structure is that of counter-rotating parallel vortices. Therefore, the model will be reduced to a two-dimensional description of the temperature field, and a circular flow as inferred from observations is assumed.

6.3.1 Model description

The advective diffusion equation for heat in a 2-dimensional domain is given by the following elliptic partial differential equation

$$\tilde{\nabla}\cdot(\tilde{k}_T\tilde{\nabla}\tilde{\theta})-\tilde{U}\cdot\tilde{\nabla}\tilde{\theta} = 0 \tag{6.30}$$

where $\tilde{U} = (\tilde{u},\tilde{w})$ describes the flow field, $\tilde{k}_T$ is the thermal diffusivity, $\tilde{\theta}$ is the potential temperature and $\tilde{\nabla}$ is the 2-dimensional nabla operator $\left(\frac{\partial}{\partial\tilde{x}},\frac{\partial}{\partial\tilde{y}}\right)$.

In the case of Langmuir circulation in the ocean surface layer we orient the domain so that the horizontal coordinate x is perpendicular to the direction of the windrow and the second coordinate z is vertical, increasing from the surface downwards. The boundary conditions are a prescribed surface heat flux and no flux across the bottom and side boundaries.

The equations are nondimensionalized in the following way

$$\begin{aligned}
x &= \frac{\tilde{x}}{L},\quad z=\frac{\tilde{z}}{L} \\
\theta &= \frac{\tilde{\theta}\,\rho\, c_p \tilde{k}_T(\gamma L)}{Q\,L}, \\
U &= \frac{\tilde{U}L}{\tilde{k}_T(\gamma L)}, \\
k_T(z) &= \frac{\tilde{k}_T(z)}{\tilde{k}_T(\gamma L)}
\end{aligned} \tag{6.31}$$

where L, γ are cell width and cell aspect ratio, respectively.

After applying this nondimensionalization the model is given by

$$\nabla \cdot (k_T \nabla\theta) - U \cdot \nabla\theta = 0 \tag{6.32}$$

with following boundary conditions:

$$\begin{gathered}\frac{\partial\theta}{\partial z} = \frac{1}{k_T}, \quad z = 0; \qquad \theta = 0, \quad z = \gamma, \\ \frac{\partial\theta}{\partial x} = 0, \quad x = \pm 1.\end{gathered} \tag{6.33}$$

The diffusivity profile $k_T(z)$ and velocity field $U = (u, w)$ have to be prescribed.

The flow field is specified by a streamfunction ψ and consists of a circular flow pattern which allows for asymmetry in strength of upwelling and downwelling:

$$\begin{gathered}u = -\frac{\partial\psi}{\partial z}; \; w = \frac{\partial\psi}{\partial x}; \\ \psi = u_0 \sin(\pi x')\sin(\pi z/\gamma)\end{gathered} \tag{6.34}$$

The horizontal coordinate is transformed into x' to accommodate the flow asymmetry:

$$\begin{gathered}x' = \frac{1-|x|}{2-2\alpha} \text{ for } |x| \geq \alpha; \\ x' = \frac{|x|}{2\alpha} \text{ for } |x| < \alpha;\end{gathered} \tag{6.35}$$

where the asymmetry factor α ($0 < \alpha < 1$) describes the centre of the cell. The strength of the circulation is defined by the maximum horizontal velocity u_0. The maximum vertical velocities evaluate as $\frac{-u_0}{2-2\alpha}$ and $\frac{u_0}{2\alpha}$ for upwelling and downwelling regions, respectively.

Hence, the flow pattern is set by four parameters. Cell width L and aspect ratio γ define the geometry of the model domain, and the velocity parameter u_0 and the asymmetry factor α specify the strength of the circulation. These model parameters are evaluated utilizing observations of Langmuir circulation in the open ocean (section 6.3.2).

The full model, given by Equations 6.32 to 6.35, has to be solved numerically. We use a finite element collocation software package by Houstis *et al* [1985a]. The algorithm is provided as FORTRAN code [Houstis *et al.*, 1985b], which is readily adapted to the above specified model.

Initially, the domain contained two counter-rotating vortices with upwelling at $x = \pm 1$ and downwelling at $x = 0$. However, the solution is axisymmetric and runs for $-1 \le x \le 0$ are identical to the full domain solution, if mirrored at $x = 0$. Therefore, the model domain taken is $-1 \le x \le 0;\ 0 \le z \le \gamma$. Anticipating largest gradients in the surface boundary layer as well as the centres of downwelling and upwelling regions an unevenly spaced finite element mesh is generated, as given in Figure 6.8. Test runs with additional grid points in the centre between horizontal grid points and in the centre between vertical grid points for $z > 0.1$, thus increasing the number of finite elements by more than three times, show less than 1% deviation from the result obtained for larger grid spacing. This provides confidence in the selected finite element mesh.

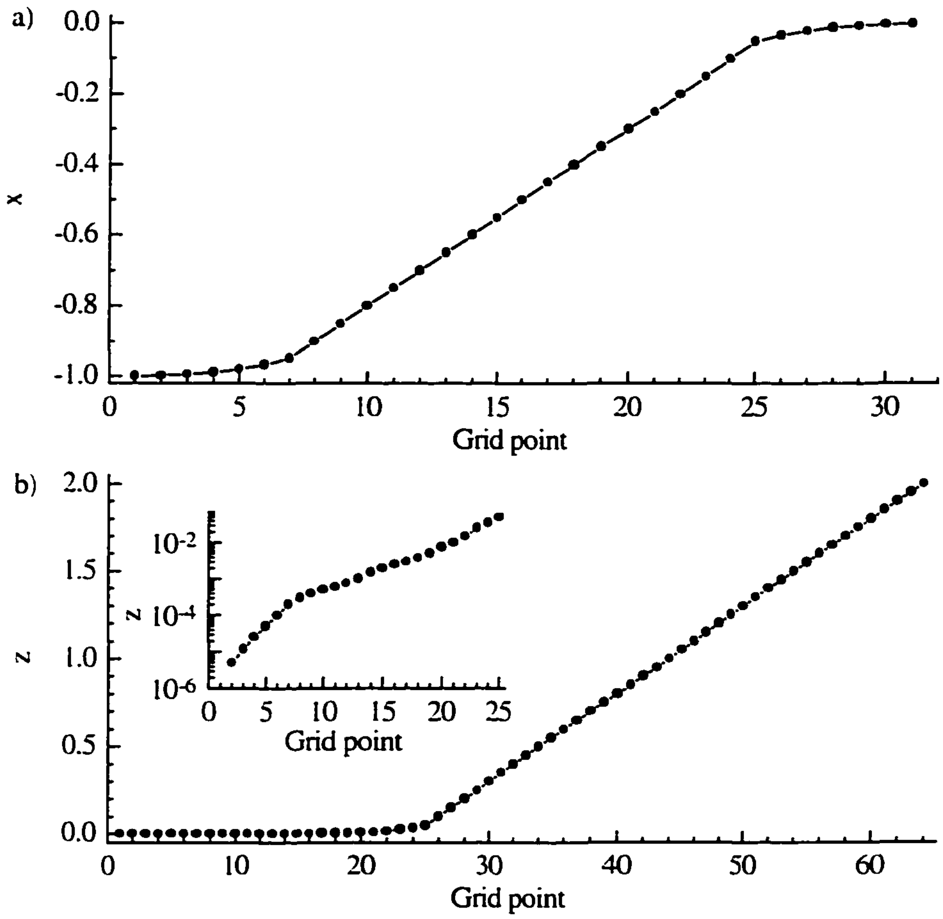

Figure 6.8: Nondimensional model grid spacing in a) horizontal and b) vertical direction. Insert in b) shows the vertical grid spacing close to the surface.

6.3.2 Model parameters

The underlying flow field has to match the flow field within the ocean surface layer so as to allow meaningful comparisons between modeled temperature fields for various diffusivity profiles and the observed temperature structure. As stated above, the flow within Langmuir circulation can be approximated by Equation 6.34 with four parameters, which distributions have to be taken from observations.

Utilizing tracks of neutrally buoyant mixed layer floats, a joint project by E. D'Asaro (APL, University of Washington) and D. Farmer (IOS), cell aspect ratio γ and flow asymmetry α are estimated. These floats, approximately 1.5 m long with 0.15 m diameter and equipped with a large metal screen to increase drag, serve as Lagrangian drifters, thus revealing the flow within Langmuir circulation. Their depth is recorded internally, whereas the horizontal position is determined acoustically relative to a set of interrogation surface buoys, which in turn are monitored by DGPS (Differential Global Positioning System). Mixed layer floats were not part of the MBL experiment, but an extensive data set of float tracks during an experiment in January 1995 off the cost of Oregon is available, with well developed Langmuir circulation on 17/01/95. Assuming similarity of Langmuir circulation, such that the aspect ratio and ratio between upwelling and downwelling velocities are preserved for different sizes and strengths of the circulation, these parameters are evaluated from the 17/01/95 mixed layer float tracks. Conversion from raw data into a time series of 3-dimensional float positions was carried out by D. Veenstra (IOS).

To evaluate cell aspect ratios and asymmetry factors the coordinate system is rotated to align with the mean wind direction and individual cells are extracted. A cell is defined from the track between two successive surface encounters. A surface encounter is defined as an approach to 4 m followed by descent to a minimum of 10 m depth. The aspect ratio of the cell is than given by the ratio of the maximum depth to the maximum cross wind displacement.

Differentiating the depth record yields the vertical velocity, and the asymmetry factor α is given by

$$\alpha = \frac{w_{\max}}{w_{\max} + |w_{\min}|} \tag{6.36}$$

where $w_{\max}$, $w_{\min}$ are maximum float speed in upwelling and downwelling regions, respectively.

The width of individual cells is estimated as half the distance between locations of maximum acoustical backscatter within bubble plumes as observed by the sidescan sonars on the acoustical platform (section 3.2.2). Vertical velocities within Langmuir convergence zones are estimated by the Doppler velocity of the upward looking sonars, with the assumption of microbubbles of approximately 10 μm radius being passive tracers. Both type of measurements were made simultaneously to our observations of the near surface temperature field on 18/04/95, and cell widths and vertical velocities were calculated by V. Polonichko (IOS, UVic).

The distributions of the four relevant flow parameters applicable to conditions during the 18/04/95 deployment are given in Figure 6.9. The distribution of cell aspect ratios γ (Figure 6.9a) peaks at values between 1 and 2. Cells deeper than they are wide are much more common than shallow cells. The median value for the aspect ratio is 1.38.

The actual width of the cells derived from sonar data (Figure 6.9b) ranges from less than 5 m up to 45 m with 25% of the cells being narrower than 10 m. Since Langmuir circulation is assumed to penetrate throughout the whole depth of the actively mixing layer, this indicates the presence of shallower layers within the mean mixed layer, which has an estimated depth of approximately 35 m.

Only 20 estimates of vertical velocities are available for the time coincident with our temperature observations. The values range from 0.031 m/s to 0.11 m/s, with a median value of 0.08 m/s (Figure 6.9c).

The distribution of the parameter α clearly shows a preference for stronger downwelling than upwelling ($\alpha < 0.5$) with less than 15 % of the observed cells having a slightly stronger upwelling, but 67% show stronger downwelling, and 18% of the cells are fairly symmetrical. The median value of the asymmetry parameter is 0.44, corresponding to the magnitude of the maximum upwelling velocity being 81% of the magnitude of the maximum downwelling velocity.

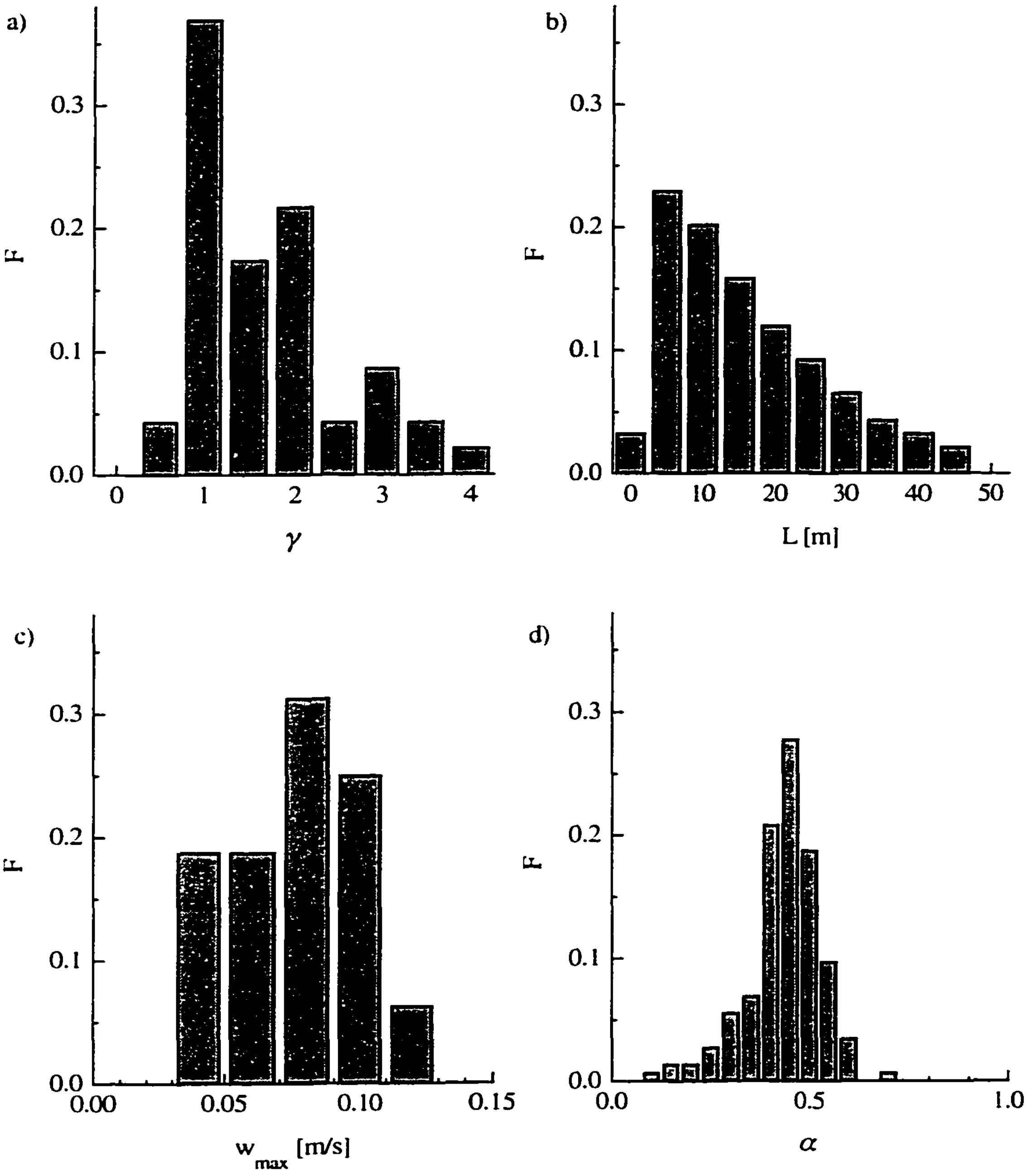

Figure 6.9: Distribution of a) cell aspect ratio, b) cell width, c) downwelling velocities and d) cell aspect ratio.

6.3.3 Model results and comparison with observations

Figure 6.10 gives an example of the modeled temperature and velocity field. Parameters for this particular run are: cell width $L = 10$ m, cell aspect ratio $\gamma = 1.5$, maximum horizontal velocity $u = 0.08$ m/s and asymmetry factor $\alpha = 0.4$. The diffusivity includes a near surface wave enhanced turbulence corresponding to the Craig & Banner [1994] model (section 6.1) with $z_0 = 0.2$ m and is shown in the right panel of Figure 6.10.

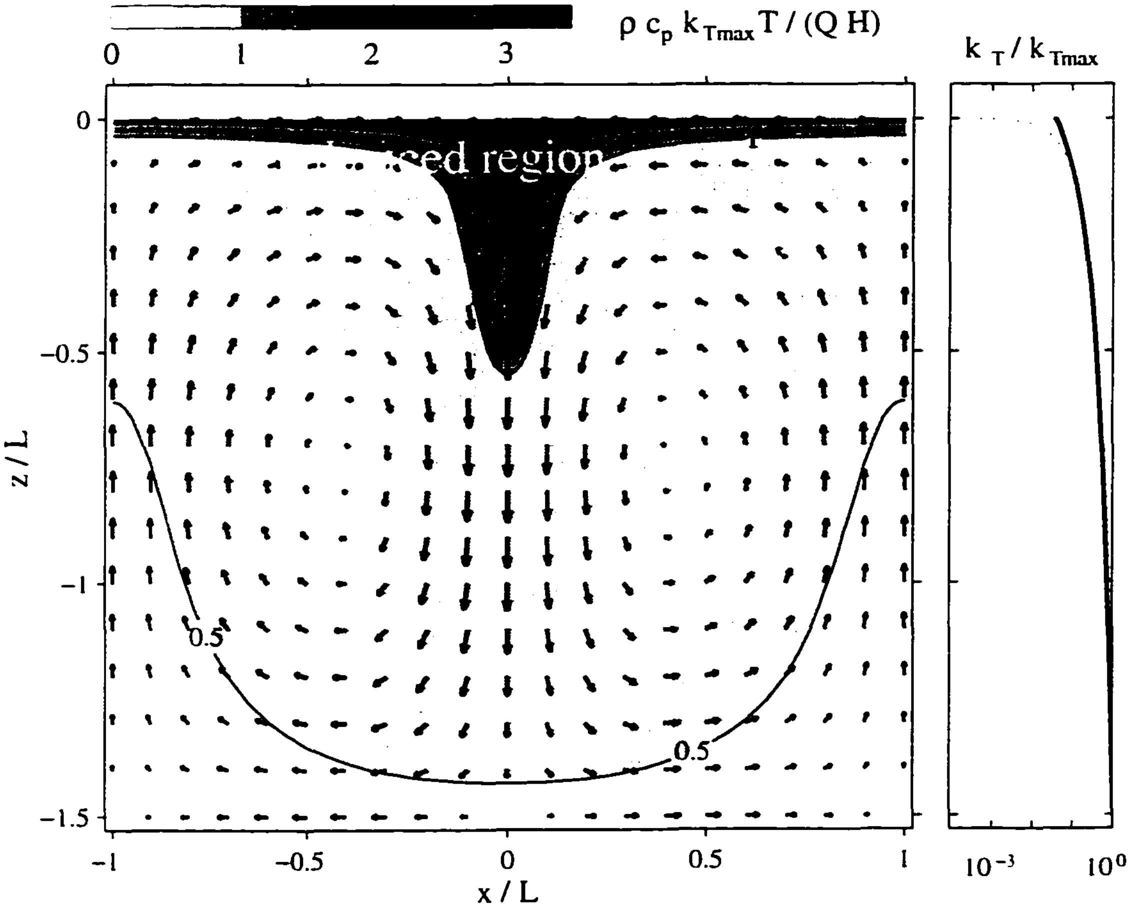

Figure 6.10: Modeled temperature and velocity field ($L = 20$ m, $\alpha = 0.4$, $\gamma = 1.5$, $u_{max} = 0.08$ m/s). The selected diffusivity profile (right panel) is obtained from the Craig & Banner [1994] model for $z_0 = 0.2$ m with near surface turbulence enhanced over wall layer scaling (dashed line).

As water reaches the surface in the upwelling region it gets exposed to the air-sea heat flux, generating a thermal boundary layer. Since heat acts as passive tracer the thermal boundary layer thickens and intensifies in the convergence region as water of anomalous temperature accumulates and gets drawn deeper. Diffusion, which increases with depth, diminishes local temperature gradients, leaving the lower part of the cell and the upwelling region nearly isothermal. In the case of surface heat loss this results in a tongue of cold water centered around the maximum downwelling.

As stated in Li & Garrett [1995], the temperature θ at any given point results from a combination of heat advection and diffusion and can be split into a conduction reference temperature θ_d and the perturbation temperature θ' due to advection

$$\theta = \theta_d + \theta' \tag{6.37}$$

Li & Garrett [1995] analyzed the cross-cell average of these quantities and found the average advective component $\langle \theta' \rangle$ to offset the gradient of the diffusive component, leading to an isothermal average cell temperature $\langle \theta \rangle$, except in the top 10% of the cell, where a cold boundary layer gets established. A very similar decomposition is obtained for our modeled average temperature profile (Figure 6.11). Results are given for the temperature field shown in Figure 6.10. The total temperature is an average across the cell, the diffusive component θ_d is calculated by integrating the flux gradient relation (Equation 2.1), which in nondimensional form reduces to

$$\frac{dT}{dz}=\frac{1}{k_T(z)} \tag{6.38}$$

and the advective component θ' results as the difference between θ and θ_d.

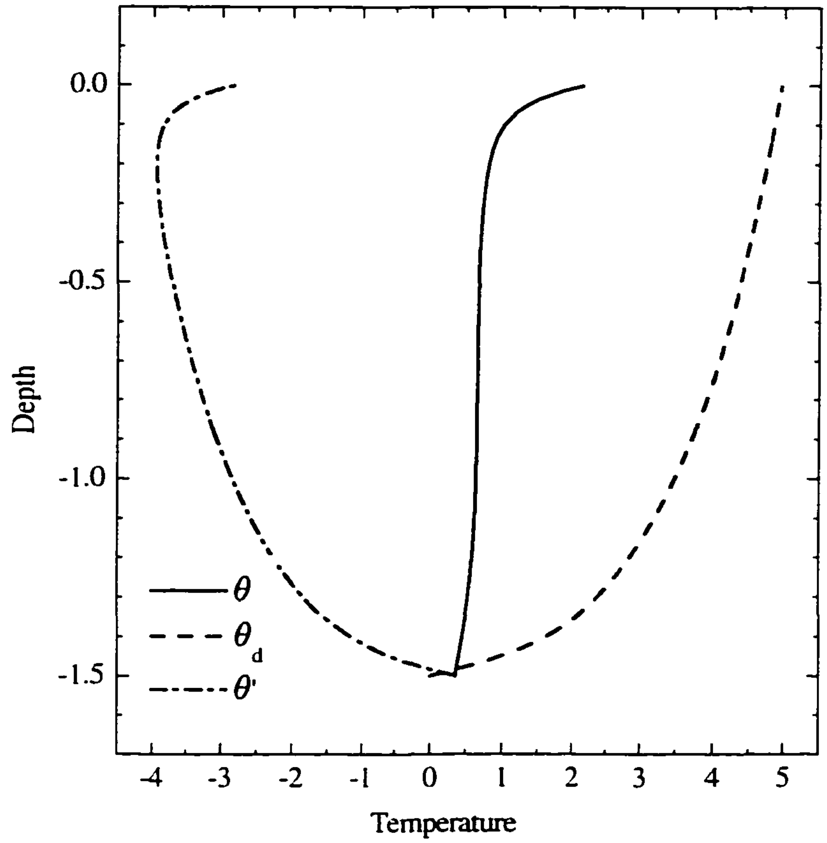

Figure 6.11: Profiles of temperature components averaged across a cell for the temperature field given in Figure 6.10: total (solid), advective (dot-dash) and diffusive (dashed).

The gradient of the mean total temperature in the top few metres of the cell converts for a typical heat loss of -250 W/m^2 to approximately -5 mK difference between the surface value and 2 m depth. This is comparable to the mean observed temperature profile (Figure 5.17). The model does not resolve the strong temperature gradient in the top few centimetres, which has to be explained by a time dependent turbulence model (section 6.2).

The horizontal variability of the turbulence field can be analyzed in terms of eddy diffusivities. In the concept of eddy exchange coefficients an apparent vertical diffusivity can be defined as

$$k(z)=\left(\frac{dT}{dz}\right)^{-1}\Bigg|_{x=const.} \tag{6.39}$$

which is composed of a contribution by eddy diffusion $k_d(z)$ plus an advective component $k'(z)$.

The apparent vertical diffusivity for the top 2 m of the temperature field of Figure 6.10 is represented in Figure 6.12. Diffusivities are normalized by the value of the diffusive component at 2 m depth, $k_d = 1.8 \times 10^{-2}\ \mathrm{m}^2/\mathrm{s}$. In the top few metres the apparent diffusivity increases compared to the diffusive case. At depths greater approximately 4 m the vertical gradient of the average perturbation temperature becomes negative and advection reduces the apparent diffusivity.

For comparison with the apparent diffusivity profiles inferred from the temperature measurements (section 6.1) the following analysis of the modeled apparent diffusivity will be limited to the upper 2 m. In the convergence region the advection of heat causes largest vertical gradients, which in turn means smallest apparent diffusivities, with a 30% increase at 2 m over the truly diffusive reference stage. This amplification increases to

150% in the divergence zone. Closer to the surface, where vertical velocities are small, the contrast between upwelling and downwelling regions decreases, with fairly uniform apparent diffusivities above 1 m depth.

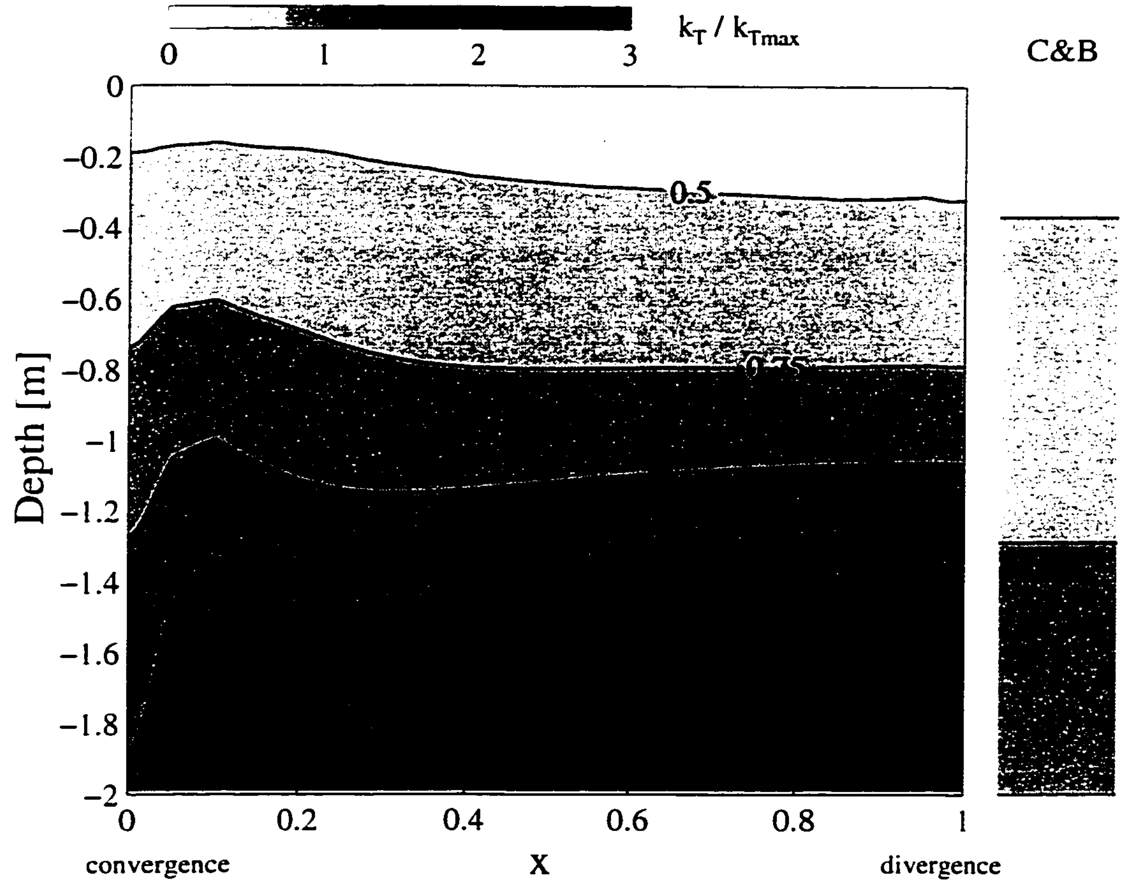

Figure 6.12: Apparent diffusivity in the top of a Langmuir cell (left) and truly diffusive component (right) normalized by the pure diffusion at 2 m depth.

The magnitude of the perturbation temperature, and hence the advective component of the diffusivity, are a function of cell geometry and flow strength. Since the mean observed diffusivity profile consists of contributions from random locations within cells with a wide variety of cell shapes, comparison with the model has also to include the same cell parameters. Therefore, the model is run for a range of cell parameters. The maximum horizontal velocity ranges from 0.02 m/s to 0.14 m/s in 0.02 m/s increments, the cell width from 10 m to 40 m in 10 m steps, the aspect ratio from 0.5 to 2.5 in steps of 0.5 and the asymmetry factor varies from 0.2 to 0.7 with step size 0.1. Temperature fields are calculated for this set of model parameters with a Craig & Banner [1994] type diffusivity (section 6.1) for 3 different roughness lengths, $z_0 = 0.1$ m, $z_0 = 0.2$ m, $z_0 = 0.3$ m and $z_0 = 0.4$ m, and an average apparent diffusivity across the cell is obtained for each temperature field.

A mean apparent model diffusivity profile, composed of 1000 simulations, which utilize the distributions of the observed flow parameters (Figure 6.9), provides a suitable comparison with the observations. Since no information on dependencies between different flow parameters is available the only restriction on combinations between them included in this simulation is that of the maximum depth γL being less than the mixed layer depth. The best agreement between the mean apparent model diffusivity profile and observations is achieved for $z_0 = 0.2$ m (see section 6.1), and in the following the roughness length will be set to this value whenever a Craig & Banner type diffusivity profile is used.

As discussed above the temperature field is a function of the flow parameters. This dependence will be analyzed in the following. For reasons of comparison with the observations we choose to characterize the model temperature field by horizontal temperature differences between the centre of downwelling and upwelling, corresponding to temperature fluctuations as described in section 5.2.3,

$$\Delta T(z) = T(z,0) - T(z,1)) \tag{6.40}$$

This parameter is evaluated at four levels (0.2 m, 0.5 m, 1.8 m and 6.5 m), corresponding to our mean sensor depths.

Figure 6.13 shows the dependence of the horizontal temperature difference on cell depth and flow speed. Cell depth is normalized by the depth of the wave enhanced layer, which we define as the depth where wall layer scaling matches the Craig & Banner type diffusivity and which in our case has a value of 5 m. Aspect ratios are held at 1.0 and asymmetry factors at 0.5. At any depth the horizontal temperature difference increases as cells deepen, due to larger overall temperatures, and decreases for stronger flow speeds. Horizontal temperature gradients are comparable within the top 2 m, but decrease at 6.5 m to values between 25% and 50%, where the ratio is largest for small cells with a fast flow and smallest for a deep cell and slow circulation.

The dependence of the horizontal gradient on the cell aspect ratio is given in Figure 6.14 for symmetrical cells of width 20 m. The temperature difference for cells twice as deep as wide is roughly three times larger than for a shallow cell of inverse aspect ratio, but same cell width. There are two main processes causing this dependency. First, for very shallow cells overturning times are small enough to transport water from the downwelling region into the upwelling region before its temperature equilibrates to the reference temperature, thereby increasing the (nondimensional) temperature in the upwelling region and decreasing the horizontal variability. The second and most likely more important reason is that the aspect ratio also determines the ratio between vertical

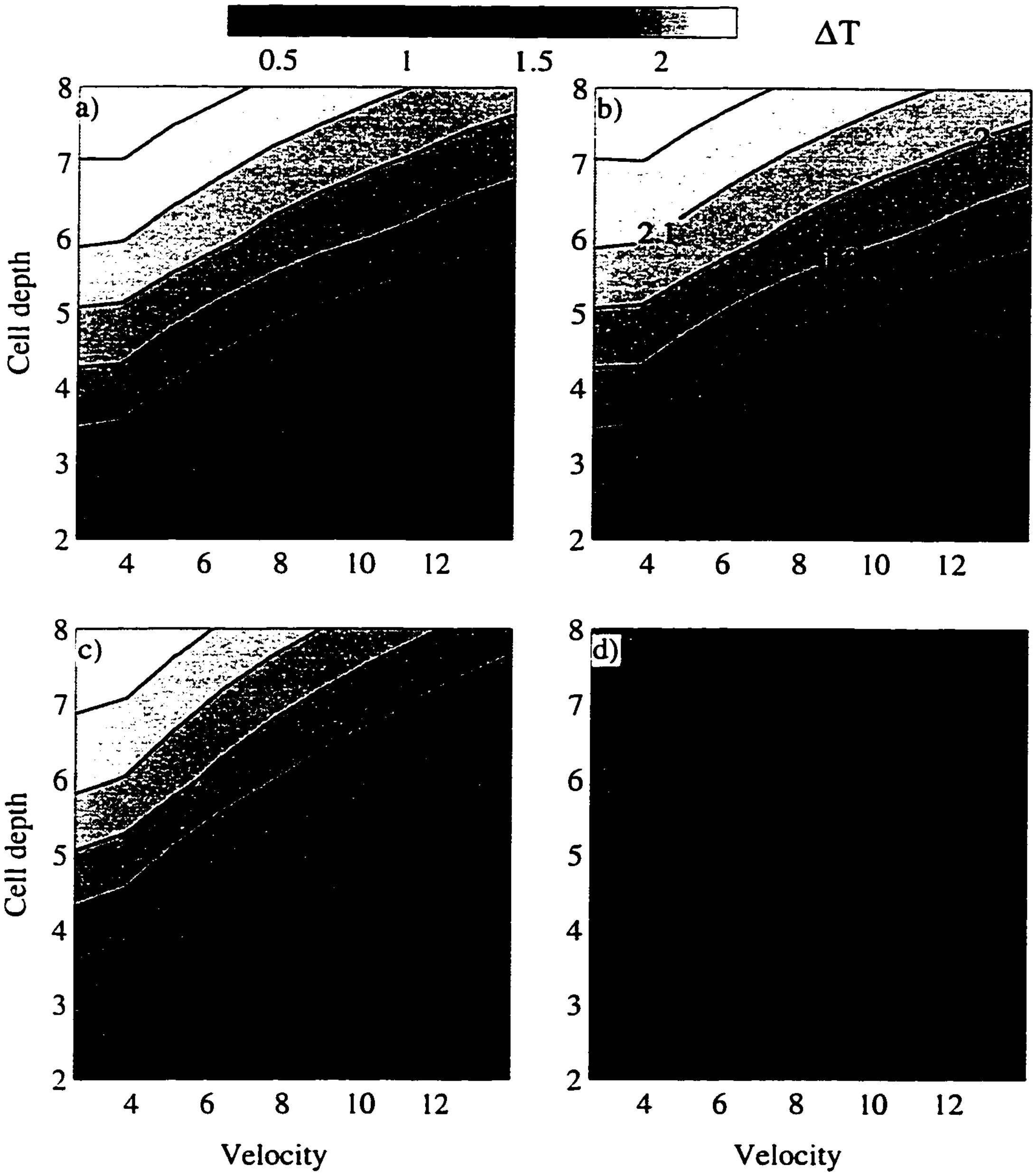

Figure 6.13: Dependence of horizontal non-dimensional temperature difference on cell depth and flow speed at a) 0.2 m, b) 0.5 m, c) 1.8 m and d) 6.5 m. For $\alpha = 0.5$, $\gamma = 1$.

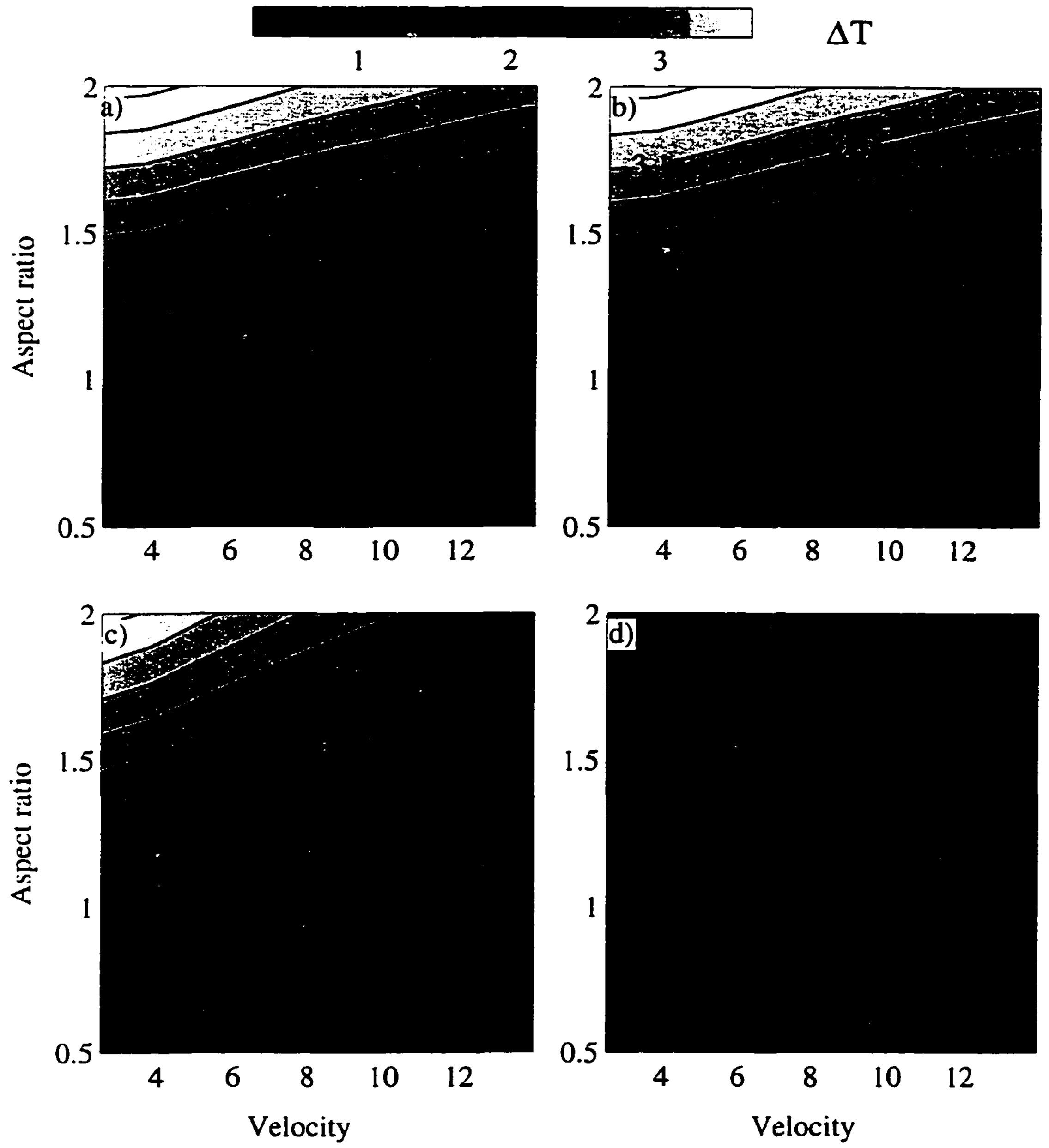

Figure 6.14: Dependence of horizontal non-dimensional temperature difference on cell aspect ratio and flow speed at a) 0.2 m, b) 0.5 m, c) 1.8 m and d) 6.5 m. For $L = 20$ m, $\alpha = 0.5$.

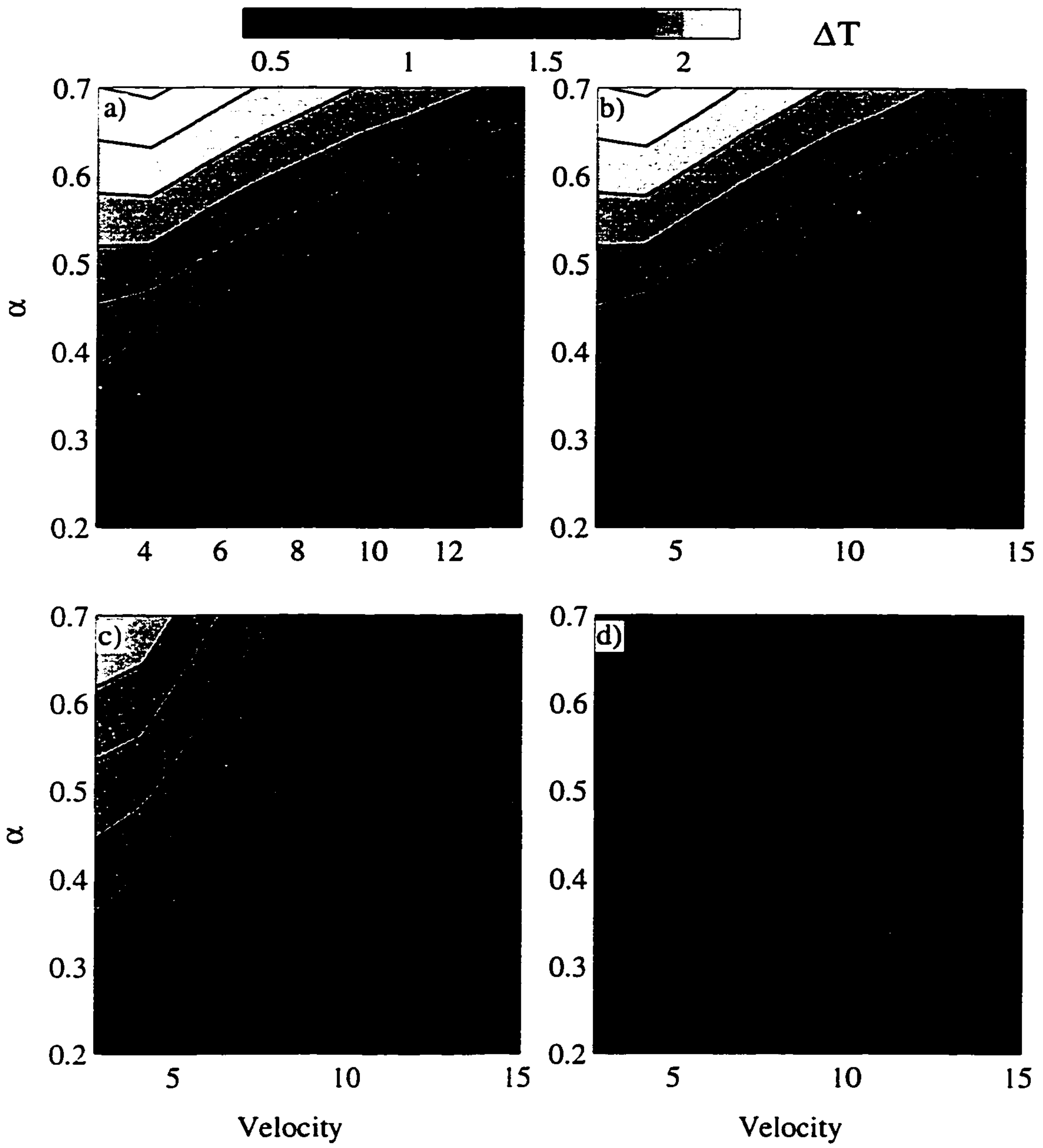

Figure 6.15: Dependence of horizontal non-dimensional temperature difference on flow asymmetry and flow speed at a) 0.2 m, b) 0.5 m, c) 1.8 m and d) 6.5 m. For L = 20 m, $\gamma = 1$.

and horizontal velocities. For $\gamma > 1$ downwelling velocities are greater than horizontal advection, allowing for greater overall temperature anomalies, which in turn allows for larger horizontal temperature differences. Close to the surface the horizontal temperature difference is almost independent of the flow speed for any aspect ratio and the given cell width and flow asymmetry. However, at 6.5 m depth values decrease for increasing flow speeds, especially for narrow cells.

For the observed range of flow asymmetries the horizontal temperature difference in the top of the cell changes by approximately 50%, with larger values expected for weaker downwelling, which also implies a wider downwelling region (Figure 6.15). However, at 6.5 m depth the value is nearly independent of the asymmetry parameter. Cell width and cell depth were held at 20 m.

The dependence of the horizontal temperature difference on model parameters are summarized as follows. For the observed range of the parameters the aspect ratio has the strongest influence and the flow asymmetry factor the weakest. Generally, ΔT decreases for increasing velocities. Narrow and deep cells generate a larger horizontal variability than shallow or wide cells, and ΔT is larger for cells with a wider downwelling than upwelling region.

The comparison between the apparent model diffusivity and the diffusivity profile inferred from the observed temperature profiles and heat fluxes shows, as discussed above, good agreement between model and observations, but is limited to the upper 2 m of the ocean surface layer. As foreshadowed in the above discussion of the model dependency on cell parameters a further parameter suitable for evaluating the model is the horizontal temperature variability. In section 5.2.3 we show temperature fluctuations with periods of several minutes are associated with the instrument drifting into downwelling regions of Langmuir cells. Hence, the difference between the model temperature at the lines of maximum upwelling and downwelling can be compared with the magnitude of these observed fluctuations.

Similar to the comparison of the diffusivity profiles, the horizontal temperature differences are calculated at the depth of our sensors (0.12 m, 0.26 m, 0.36 m, 0.51 m, 1.8 m, 6.5 m) for all above described model temperature fields with a diffusivity profile according to the Craig & Banner [1994] model for $z_0 = 0.2$ m. The distribution of the model temperature differences (Figure 6.16) is calculated from 1000 simulations, which again incorporate the distributions of the observed values of the model parameters (Figure 6.9). Good agreement between model and observations is found at all levels, however at 1.8 m depth observed values are somewhat smaller than the model predicts.

Nevertheless, the overall depth dependence of the horizontal gradient is well reproduced in the model, with the median value close to the surface being 2.4 times the median value at 6.5 m depth.

Generally, observations have a slightly narrower distribution than the model. The observations are best reconciled at 6.5 m depth, where the median values of observations and model agree within 1%. At 1.8 m the discrepancy of the median values is 20%, 14% at 0.51 depth, 2% at 0.36 m depth, 4% at 0.26 m depth and 8% at the shallowest sensor.

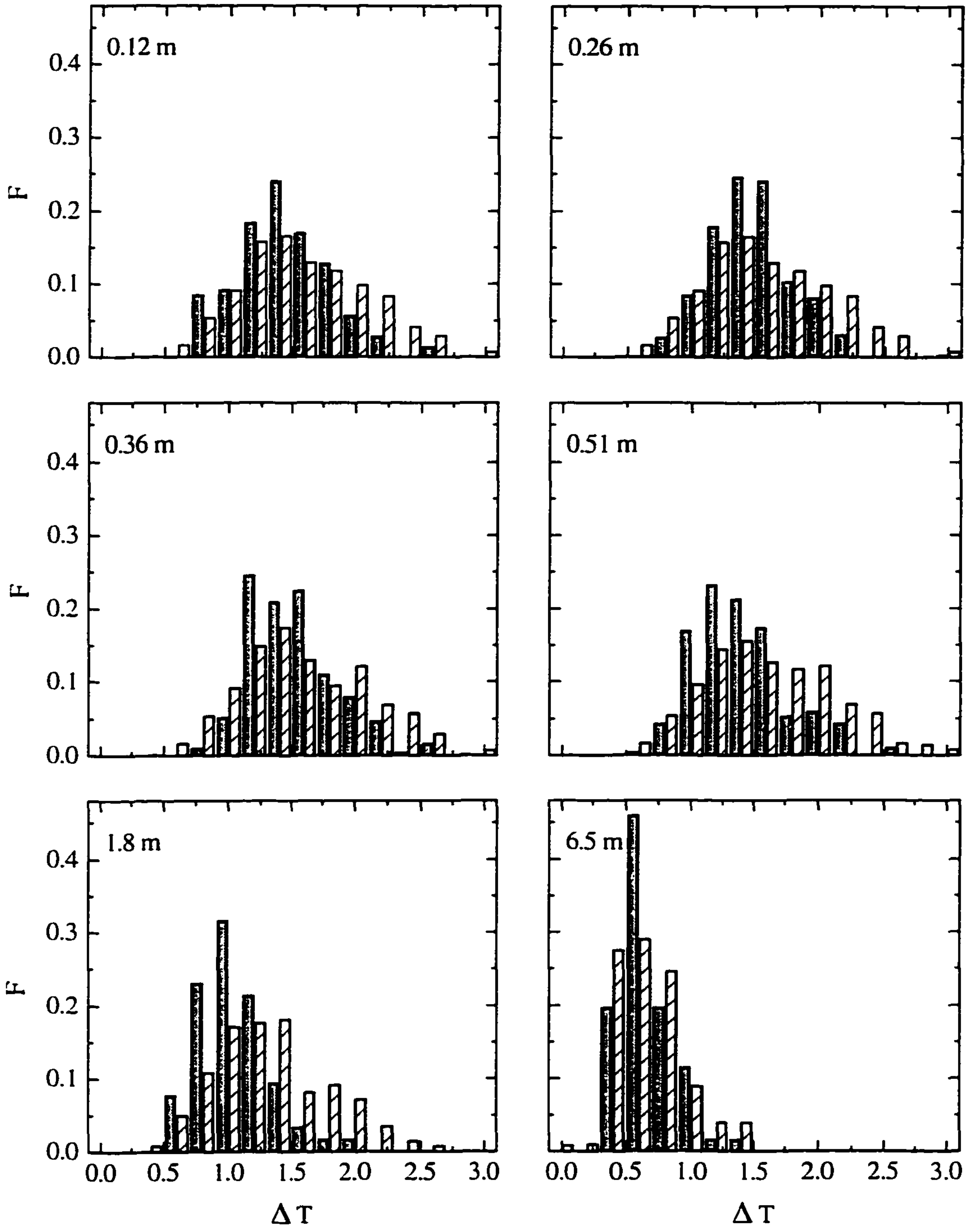

Figure 6.16: Distribution of observed (solid) and modeled (pattern) temperature fluctuations at all sensor depths.

The depth dependence of the temperature difference between upwelling and downwelling regions is the striking difference between temperature fields obtained for various diffusivity profiles. Figure 6.17 shows profiles of temperature differences for wave enhanced diffusivities, wall layer scaling and a constant diffusivity

$$k_T = 2.6\times 10^{-5}\frac{u_{10}^3}{g} \tag{6.41}$$

suggested in Li & Garrett [1995]. Profiles of a particular run with $L = 20$ m, $\gamma = 1.4$, $\alpha = 0.4$, $u_0 = 0.08$ m/s, which closely matches the median values of the observations, are shown. However, differences in the shape of the profiles are well presented in any model run with cell parameters within the range of the observation. Under wall layer scaling large temperature anomalies are generated close to the surface due to small diffusivities, and unrealistically high horizontal temperature differences are predicted in the upper 5 m of the cell. In the lower half of the cell the temperature variability follows closely the profile of the wave enhanced case. In the case of a constant diffusivity the horizontal temperature difference matches the wave enhanced case in the upper 1 m, where diffusivities are comparable between the two scenarios, however less than 20% variation is found to within 1 m to the bottom of the cell. Since neither wall layer scaling nor a constant diffusivity can match the observations, this supports the evidence of a depth variable diffusivity profile with a wave enhanced turbulent surface layer.

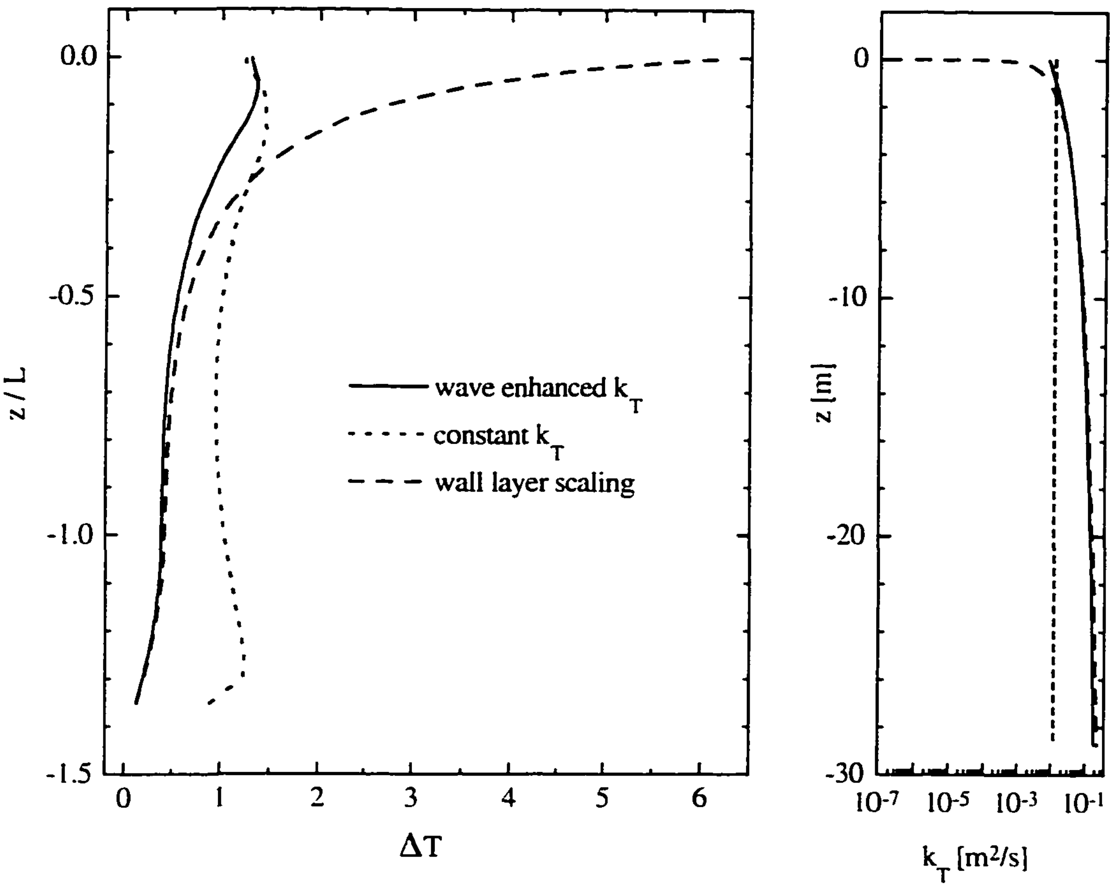

Figure 6.17: Left panel: Profile of temperature difference between upwelling and downwelling regions of modeled temperature fields for wave enhanced turbulence near the surface (solid), depth independent diffusivity (dots) and wall layer scaling (dashes). Right panel shows corresponding diffusivity profiles.

The lack of depth variability of the horizontal temperature difference is also inherent in Li & Garrett's [1995] scale analysis, which predicts the temperature difference within the boundary layer in the top of the cell, and is given in Equation 2.14. For comparison with our data we normalize the Li & Garrett [1995] estimate of the horizontal temperature difference in the following way

$$\delta\theta = \frac{\delta\tilde{\theta}\,\rho\, c_p\, \kappa_T\, \beta_s}{Q} \tag{6.42}$$

where β_s is the e-folding depth of the Stokes drift and κ_T is the eddy diffusivity estimated from the Langmuir number La with the assumption of a turbulent Prandtl number $\mathrm{Pr}_t = 1$. Langmuir number and Stokes drift were provided by V. Polonichko (IOS, UVic); a description of the calculation is given in Farmer *et al.* [1997]. The normalized data are compared in Figure 6.18. For the particular choice of the proportionality factor *C* in Equation 2.14 observations and model agree well at 6.5m. Since no depth dependence is included in the scaling in Equation 2.14 the temperature differences across the cells exceed the prediction at shallower depths, a result attributed to low turbulence levels in the Li & Garrett [1995] model at greater depth.

6.4 Energy balance

If breaking waves are a major source of the turbulent kinetic energy in the near surface layer the dissipation has to account for the energy flux into the wave field. Hence, the evaluation of these two terms can serve as a consistency check of this assumption. While the energy input was specified by $\overline{E}_{in} = \bar{c}_p\, u_*^2$ (see Equation 6.10) the dissipation can be estimated as the total contributed by individual breaking waves or from a mean dissipation profile given by the turbulence model.

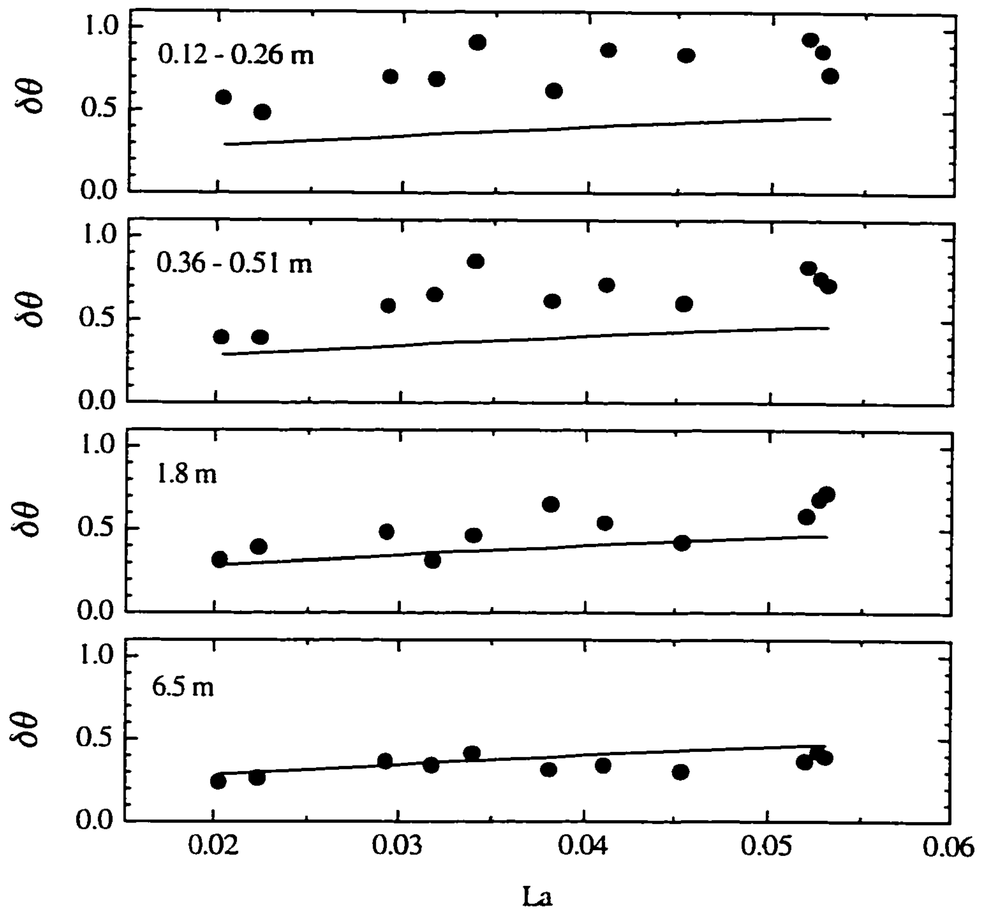

Figure 6.18: Normalized temperature difference between convergent and divergent regions of Langmuir cells, for different depths, expressed as a function of Langmuir number (circles) and Li & Garrett's [1995] model predictions (line).

In the first method we scale dissipation rates obtained in laboratory experiments by size and frequency of breaking waves observed in the open ocean. Following Thorpe [1993] we assume a simplistic wave field consisting of a uniform two-dimensional array of waves with parallel wave crests and wave length λ. The rate of energy loss from the waves per unit surface area is then given as

$$E_w = \frac{E_L f}{\lambda} \tag{6.43}$$

where E_L is the rate of energy loss per unit crest length and f is the frequency of breaking per wave [Thorpe, 1993]. Melville [1994] estimated the energy loss per unit crest length E_L based on the deepening of a turbulent patch beneath breaking waves in a wave tank [Rapp & Melville, 1990]. He found for unsteady spilling waves

$$E_L = 3.2 \times 10^{-3} \frac{c^5}{g} \tag{6.44}$$

where c is the wave phase speed. However, it should be pointed out that this should only be considered as an order of magnitude estimate [Melville, 1994]. We choose the wave length in Thorpe's [1993] model (Equation 6.43) to be the size which is associated with breaking and E_L given by Melville [1994] (Equation 6.44). Then,

$$E_w = 8 \times 10^{-5} c_b f_b \tag{6.45}$$

where c_b is the phase speed of breaking waves, f_b is the frequency of breaking per dissipating wave (Equation 5.10) and we use the dispersion relation for deep water gravity waves

$$\lambda = 2\pi \frac{c^2}{g} \tag{6.46}$$

We infer the phase speed of breaking waves c_b from measurements $c_b = 0.56\,c_p$ (section 5.1.4) which gives for the 18/04/95 data set 7 m/s. The breaking frequency f_b can be estimated from our scaling presented in Figure 5.8. For the 18/04/95 data set the normalized wave energy input F_w / F_{GMP} increases from 1.7 at the beginning of the deployment to 2.2 at 800h. Hence, the normalized breaking frequency is expected to range from roughly 0.07 to 0.15. For the above specified range of breaking frequencies and phase speed, the ratio between the energy loss of the waves due to breaking and the energy input into the wave field $R_w = E_{in} / E_w$ lies between 0.12 and 0.26. Given the order of magnitude estimate of the dissipation of individual breaking waves, the rather simplistic wave field model and the crude approximation of the range of breaking wave scales by their median value, we conclude that the estimate of the wave energy dissipation is broadly consistent with the energy input.

Alternatively, as discussed in section 6.1, the Craig & Banner [1994] turbulence closure model predicts for a roughness length $z_0 = 0.2$ m, which is in agreement with our data, that 94% of the total dissipation is accounted for by the energy flux from the wind into the waves. This supports the interpretation of enhanced near surface turbulence levels being attributed to wave breaking.

7. Conclusions and summary

This work provides the first coherent account of the complex oceanic near surface turbulence field created by breaking waves, shear stress and the advective field of Langmuir circulation and shows the feasibility of inferring near surface turbulence in the ocean surface layer under severe wind and wave conditions, by utilizing heat as a passive tracer. In particular a near surface layer of enhanced turbulence in the open ocean at storm conditions was identified and could be linked to breaking wave activity. Our findings are consistent with results of previous studies [Agrawal *et al.*, 1992; Anis & Moum, 1992, 1995] and extend the concept of enhanced turbulence levels from extremely fetch limited limnological observations under waves of 0.3 m wave height [Agrawal *et al.*, 1992] and oceanic observations under moderate wind conditions [Anis & Moum, 1992, 1995] to open ocean storm conditions with typical significant wave heights of order 5 m. Injection of the turbulent kinetic energy as well as the decay of turbulence can be inferred from the fine scale temperature structure, but the interpretation needs to include enhanced diffusion and the advective field of Langmuir circulation. A simple turbulence closure model which accounts for injection of energy into the surface layer [Craig & Banner, 1994] is supported by our measurements. Comparison between the modeled dissipation within the mixed layer and the energy input into the wave field identifies breaking waves as the major source of the turbulent kinetic energy in the ocean surface layer. Furthermore, by applying a two-dimensional advective diffusion model which incorporates the turbulence characteristics defined within this thesis, it could be possible to make inferences about the strength and size of Langmuir circulation, requiring only accurate temperature measurements within the top few metres of the ocean. The model also shows that it is unlikely to detect a temperature signal associated with Langmuir circulation below approximately half the cell depth, which might be the reason for little evidence of a thermal signature in previous investigations of Langmuir circulation and has to be considered in the design of future experiments.

Incorporated within this account are several key findings, which are summarized as follows. A self contained instrument was developed, which due to its surface following properties of the sensor boom allows for continuous monitoring of the fine scale variability of the near surface temperature field, even under breaking waves. Profiling the upper 2 m of the surface layer with a thermistor mounted on a mechanically driven cart proved especially valuable. Conductivity cells, although not an entirely new application to breaking wave studies, were tested and calibrated to provide reliable estimates of air entrainment beneath breaking waves. Generation of turbulence depends on the strength, scale and frequency of breaking events, and the conductivity measurements not only provided insight into the process of air entrainment, but also allows one to establish a well defined breaking criterion, consistent with theoretical predictions. The lack of a uniform criterion for the detection of wave breaking might be one reason for the wide range of frequencies of occurrence of breaking waves given by different authors (see Holthuijsen & Herbers [1986]). However, even if restricted to our measurements obtained with a single instrument employing a single breaking criterion, the fraction of breaking waves per dominant wave does not scale with wind speed or wave age as suggested previously [Thorpe, 1993]. Our analysis of breaking frequencies observed under a wide variety of fetch and wave age conditions identifies the energy transfer from the wind to the wave field as the driving parameter for breaking. Furthermore, normalization of the breaking frequency by the frequency of waves associated with dissipation of wave energy reduces the scatter of the data points over the scaling by the frequency of the dominant waves. This is also of great significance for scaling laboratory results of processes associated with breaking waves to natural conditions.

It was found that all wave scales larger than approximately one tenth of the dominant wave length exhibit breaking with significant air entrainment. In terms of wave period the median value of the observed breaking waves is 0.56 times the period of the dominant waves, which compares favourably with the very limited published results of other investigators, but the range of scales is much wider than that of the literature values. Exploiting the height information of the breaking waves revealed waves which break are generally not the highest waves, but on average only approximately 0.7 times the significant wave height.

Air entrainment, as detected at a single point, often reaches values of volumetric fractions more than 60%. These high values however are restricted to approximately the top 0.2 m depth and last on average less than 1 s. In the open ocean approximately 3% of breaking events show deeper penetrating large air fractions, leading to the conclusion of them being plunging breakers, and 97% of breaking waves being of spilling type. For a young wave field in a fetch limited coastal environment the number of plunging breakers increased to 10% of the total number of breaking waves.

Both the temperature profile and the time series at fixed depths revealed a rich fine scale variability. Individual temperature profiles within the top 2 m of the ocean show fluctuations of order 10 - 20 mK, with their magnitude decreasing with depth. Their vertical extension is an estimate of the size of the turbulence elements. This size has a near surface value of 0.2 m and increases approximately linearly below. Notwithstanding the limitations imposed by a relatively short profiling depth, this supports the concept of a depth dependent mixing length with a minimum near surface value often referred to as roughness length. The gradient of the average profile is roughly 5 mK between 0.1 m depth and 1.8 m depth. However, 8 mK difference from 0.05 m to 0.1 m depth indicates the presence of a surface layer with strong temperature gradients.

The ratio of the air-sea heat flux and the vertical temperature gradient defines the eddy diffusivity. Comparison with wall layer scaling confirms the existence of wave enhanced turbulence in the upper 2 m. The apparent diffusivity, which consists of a diffusive and advective component, depends on the location relative to Langmuir circulation. The apparent diffusivity in the convergence zone at 1.5 m depth is roughly 40% smaller than the corresponding value in divergent regions. The cross cell average of the diffusivity profile is well represented by a conventional turbulence closure model modified to account for the input of the turbulent kinetic energy due to breaking waves

[Craig & Banner, 1994] under inclusion of an improved parameterization of the wave energy input [Gemmrich *et al.*, 1994]. The consistency of this application of the Craig & Banner [1994] model is supported by the fact that our independent estimate of the roughness length is essentially identical with the best fit of the model of $z_0 = 0.2$ m. This roughness length also compares favourably with the scale of the layer of active turbulence as established by the air entrainment depth.

Beneath approximately 30% of breaking waves brief temperature fluctuations of typically 20 mK coincident with the air entrainment were observed. These temperature signals are consequences of mixing of a surface layer of anomalous temperature, approximately 30 mm - 50 mm thick, to the depth of the shallowest sensor. Following a breaking event the thermal boundary layer reestablishes and for a given heat flux the evolution of its intensity is only a function of (time dependent) turbulence levels. Initially high turbulence levels, fairly constant within the layer of air entrainment, decay rapidly following a power law. The exponent of decay of the turbulent kinetic energy in the isotropic case is -2.5; however, we hypothesize the presence of microbubbles, abundant in the top few centimetres of the ocean in Langmuir convergence zones, reduces the exponent to -4.7, a value based on wind tunnel experiments. This rapid decay preserves a mean wave enhanced near surface turbulence field, but also allows for the development of temperature gradients in the upper few centimetres increasing with time. Combining the modeled evolution of the temperature gradient with the observed periods between breaking waves the distribution of the observed temperature anomalies are reconciled under the assumption of vertical mixing of a surface layer of 30 mm to 50 mm thickness.

The initial diffusivity within breaking waves, for a particular friction velocity of 0.02 m/s, was found to be 3×10^{-2} m^2/s, or approximately 40 times the mean diffusivity according to the wall layer scaling.

Low frequency temperature fluctuations with duration of order one minute were observed at all fixed depth thermistors (0.12 m to 6.5 m) and are caused by the instrument drifting into Langmuir convergence zones. Advection of surface water, which is exposed to the air sea heat flux, accumulates water of anomalous temperature within the downwelling region of Langmuir circulation, which results in significant horizontal temperature gradients. The magnitude of these fluctuations decreases with depth from typically (for our data set) 15 mK in the upper 0.5 m to 5 mK at 6.5 m depth.

This phenomenon was successfully modeled by employing a steady state two-dimensional advective-diffusion model to the temperature field. Driving it with observed distributions of cell geometry and flow parameters allows evaluation of the effects of various turbulence fields as expressed in the diffusivity profiles. Wall layer scaling predicts a realistic temperature field at depths below roughly 5 m, however the surface region is marked by a strong temperature gradient resulting in a horizontal temperature variability more than 5 times larger than observed. On the other hand a diffusivity taken as constant throughout the depth of the mixed layer, as assumed in two-dimensional modeling of Langmuir circulation [Li & Garrett, 1993], reconciles the near surface temperature field reasonably well but fails at depths greater than approximately 2 m. Applying a diffusivity profile which incorporates a boundary layer of a wave-breaking enhanced turbulence matched to a 'law of the wall layer' below, as suggested by Craig &

Banner [1994] and supported by our temperature profiles, predicts horizontal temperature variabilities in close agreement with the observed temperature fluctuations at all sensor depths. The combined action of the shear stress turbulence, wave stirring and the advective field of Langmuir circulation results in tongues of colder water (in the case of an outgoing heat flux) centered at the downwelling region and fairly isothermal conditions in the lower part and the upwelling region of Langmuir cells.

Although this work leads to important results on near surface turbulence and wave breaking there are certain limitations which it is recommended be addressed in future. The steady state model fails to predict temperature gradients in the upper few centimetres consistent with the observations of temperature fluctuations beneath breaking waves, most likely due to the inherent restriction of time averaged diffusivities. Combining the advective diffusion model with the model of decaying turbulence beneath breaking waves is therefore desirable.

Our proposed scaling of the breaking frequency includes energy transfer from the wind to waves, which is based on integration of the directional wave spectrum weighted towards high frequencies. In most of our cases information on directionality was lacking and had to be modeled. Inclusion of measured high resolution directional wave spectra is expected to improve the scaling of breaking frequencies even further.

Recommended modifications of the measurement approach include a horizontal array of conductivity cells in addition to the vertical arrangement to help determine the instrument position relative to the breaking wave. The extension of the profiling depth would provide valuable insight in the proposed matching of the wave enhanced layer to the wall layer, an unresolved topic in upper ocean turbulence studies [Thorpe, 1984, 1992; Drennan *et al.*, 1992; Craig, 1996], and would help to clarify the depth dependence of size and magnitude of the turbulence elements. Although the capacitance wire gauge, which provides precise measurements of the relative water surface height, is only 20 mm from the profiling thermistor, it would be desirable to bring it even closer to improve the interpretation of the temperature structure in the top few centimetres.

Bibliography

Agrawal, Y. C., E. A. Terray, M. A. Donelan, P. A. Hwang, A. J. Williams III, W. M. Drennan, K. K. Kahma and S. A. Kitaigorodskii, 1992: Enhanced dissipation of kinetic energy beneath surface waves. *Nature*, **359**, 219 - 220.

Anis, A. and J. N. Moum, 1992: The superadiabatic surface layer of the ocean during convection. *Journal of Physical Oceanography* **22**, 1221 - 1227.

Anis, A. and J. N. Moum, 1995: Surface wave-turbulence interactions: scaling $\varepsilon(z)$ near the sea surface. *Journal of Physical Oceanography* **25**, 2025 - 2045.

Apel, J. R., 1987: Principles of ocean physics. *Academic Press.* 634 pp.

Banner, M. L., 1990: Equilibrium spectra of wind waves. *Journal of Physical Oceanography*, **20**, 966 - 984.

Banner, M. L. and M. A. Donelan, 1992: The physical consequences of wave breaking in deep water. In: Banner, M. L. and R. H. J. Grimshaw (Eds.) *Breaking waves IUTAM Symposium* Sydney, Australia, 1991, *Springer Verlag*, 3 - 20.

Banner, M. L. and D. H. Peregrine, 1993: Wave breaking in deep water. *Annual Reviews of Fluid Mechanics*, **25**, 373 - 397.

Bernier, R. J. N., 1982: Unsteady two-phase flow instrumentation and measurement. *Ph.D. Thesis, California Institute of Technology.* 152 pp.

Bortkovskii, R. S., 1987: Air-sea exchange of heat and moisture during storms. *D. Reidel Publishing Company*, 194 pp.

Bruch, H., 1940: Die vertikale Verteilung von Windgeschwindigkeit und Temperatur in den untersten Metern über der Wasseroberfläche. *Veröffentlichungen des Institutes für Meereskunde Berlin. Neue Folge* **A 38**

Carslaw, H. S. and J. C. Jaeger, 1959: Conduction of heat in solids. Second edition. *Oxford Press*, 510 pp.

Caudal, G., 1993: Self-consistency between wind stress, wave spectrum, and wind-induced wave growth for fully rough air-sea interface. *Journal of Geophysical Research*, **98**, 22743 - 22752.

Charnock, H., 1955: Wind stress on a water surface. *Quarterly Journal of the Royal Meteorological Society*, **81**, 639 - 640.

Churchill, J. H. and G. T. Csanady, 1983: Near-surface measurements of quasi-Lagrangian velocities in open waters. *Journal of Physical Oceanography*, **13**, 1669 - 1680.

Clauss, E., H. Hinzpeter and J. Müller-Glewe, 1970: Messungen zur Temperaturstruktur im Wasser an der Grenzfläche Ozean-Atmosphäre. *"Meteor" Forschungs-Ergebnisse*, **B5**, 90 - 94.

Cliff, R., J. R. Grace and M. E. Weber, 1978: Bubbles, drops and particles. *Academic Press*, 380 pp.

Craig, P. D., 1996: Velocity profile and surface roughness under breaking waves. *Journal of Geophysical Research*, **101**, 1265 - 1277.

Craig, P. D. and M. L. Banner, 1994: Modeling wave-enhanced turbulence in the ocean surface layer. *Journal of Physical Oceanography*, **24**, 2546 - 2559.

Craik, A. D. D., 1977: The generation of Langmuir circulations by an instability mechanism. *Journal of Fluid Mechanics*, **81**, 209 - 223.

D'Asaro, E. A. and G. T. Dairiki, 1996: Turbulence measurements in a wind driven mixed layer. *Journal of Physical Oceanography*, submitted.

Denman, K. L. and A. E. Gargett, 1995: Biological-physical interaction in the upper ocean: The role of vertical and small scale transport processes. *Annual Review of Fluid Mechanics*, **27**, 225 - 255.

Ding, L. and D. M. Farmer, 1992: A signal processing scheme for passive acoustical mapping of breaking surface waves. *Journal of Atmospheric and Oceanic Technology*, **9**, 484 - 494.

Ding, L. and D. M. Farmer, 1994: Observations of breaking wave statistics. *Journal of Physical Oceanography*, **24**, 1368 - 1387.

Dold, J. W. and D. P. Peregrine, 1986: Numerical methods for fluid dynamics 2. K. W. Morton and M. J. Baines (Eds.), *Oxford University press*, pp. 671 - 679.

Donelan, M., 1990: Air-sea interaction. In: LeMehaute, B. and D. M. Hanes (Eds.), *The Sea: Ocean Engineering Sciences* **9A**, 239 - 292.

Donelan, M. A. and W. J. Pierson, 1987: Radar scattering and equilibrium ranges in wind generated waves with applications to scatterometry. *Journal of Geophysical Research*, **92**, 4971 - 5029.

Donelan, M. A., J. Hamilton and W. H. Hui, 1985: Directional spectra of wind generated waves. *Philosophical Transactions of the Royal Society of London, Series A*, **315**, 509 - 562.

Drennan, W. M., K. K. Kahma, E. A. Terray, M. A. Donelan and S. A. Kitaigorodskii, 1992: Observations of the enhanced of the kinetic energy dissipation beneath breaking wind waves. In: Banner, M. L. and R. H. J. Grimshaw (Eds.) *Breaking waves IUTAM Symposium* Sydney, Australia, 1991, *Springer Verlag*, 95 - 101.

Duncan, J. H., 1981: An investigation of breaking waves produced by a towed hydrofoil. *Proceedings of the Royal Society of London, Series A*, **337**, 331 - 348.

Efimova, N. A., 1961: On methods of calculating monthly values of net long wave radiation. *Meteorology and Hydrology,* **10**, 28 - 33.

Efron, B. and G. Gong, 1983: A leisurely look at bootstrap, the jackknife, and cross-validation. *The American Statistician,* **37**, 36 - 48.

Farmer, D. M. and J. R. Gemmrich, 1996: Measurements of temperature fluctuations in breaking surface waves. *Journal of Physical Oceanography,* **5**, 816 - 825.

Farmer, D., J. Gemmrich and V. Polonichko, 1997: Velocity, temperature and spatial structure of Langmuir circulation. *Coastal and estuarine studies,* in press.

Farmer, D. and M. Li, 1995: Patterns of bubble clouds organized by Langmuir circulation. *Journal of Physical Oceanography,* **25**, 1426 - 1440.

Farmer, D. M., C. L. McNeil and B. D. Johnson, 1993: Evidence for the importance of bubbles in increasing air-sea gas flux. *Nature,* **361**, 620 - 623.

Farmer, D. M., S. Vagle and A. D. Booth, 1997: A free flooding acoustical resonator for measurements of bubble size distributions. *Journal of Atmospheric and Oceanic Technology,* submitted.

Farmer, D. M. and S. Vagle, 1988: On the determination of breaking surface wave distributions using ambient sound. *Journal of Geophysical Research,* **93**, 3591 - 3600.

Gemmrich, J. and L. Hasse, 1992: Small-scale surface streaming under natural conditions as effective in air-sea gas exchange. *Tellus* **44B**, 150 - 159.

Gemmrich, J. R., T. D. Mudge and V. D. Polonichko, 1994: On the energy input from wind to surface waves. *Journal of Physical Oceanography,* **24**, 2413 - 2417.

Gill, A. E., 1982: Atmosphere-ocean dynamics. *Academic Press,* 662 pp.

Gower, J. and D. Jones, 1994: Canadian West Coast giant waves. *Mariners Weather Log (NOAA)*, **Vol. 38 No. 2**, 4-8.

Graßl, H., 1976: The dependence of the measured cool skin of the ocean on wind stress and total heat flux. *Boundary Layer Meteorology*, **10**, 465 - 474

Hasse, L., 1971: The sea surface temperature deviation and the heat flow at the sea-air interface. *Boundary Layer Meteorology*, **1**, 368 - 379

Hinze, J. O., 1975: Turbulence, Second Edition. *McGraw-Hill series in mechanical engineering*. 790 pp.

Holthuijsen, L. H. and T. H. C. Herbers, 1986: Statistics of breaking waves observed as whitecaps in the open sea. *Journal of Physical Oceanography.*, **16**, 290 - 297.

Houstis, E. N., W. F. Mitchell and J. R. Rice, 1985a: Collocation software for second-order elliptic partial differential equations. *Association for Computing Machinery, Transaction on Mathematical Software*, **11**, 379 - 412.

Houstis, E. N., W. F. Mitchell and J. R. Rice, 1985b: Algorithm 638 INTCOL and HERMCOL: Collocation on rectangular domains with bicubic hermite polynomials. *Association for Computing Machinery, Transaction on Mathematical Software*, **11**, 416 - 418. Code at: http://www.netlib.org/toms/638

Hsiao, S. V. and O. H. Shemdin, 1983: Measurements of wind velocity and pressure with a wave follower during MARSEN. *Journal of Geophysical Research*, **88**, 9841 - 9849.

Jähne, B., 1990: New experimental results influencing air-sea gas exchange. In: Wilhelms, S. C. and J. S. Gulliver (Eds.). *Proceedings of the Second International Symposium on Air-Water Mass Transfer*, Us Army waterways experimental station / ASCE, Minneapolis. 582 - 592.

Jessup, A. T., 1996: The infrared signature of breaking waves. In: Donelan M. A., W. H. Hui and W. J. Plant (Eds.). The air-sea interface. *University of Toronto Press*, in press.

Katsaros, K. B., 1976: Effects of precipitation on the eddy exchange in a wind driven sea. *Dynamics of Atmospheres and Oceans,* **1**, 99-126.

Katsaros, K. B., 1980: The aqueous thermal boundary layer. *Boundary Layer Meteorology,* **18**, 107 - 127.

Katsaros, K. B. and S. S. Atatürk, 1992: Dependence of wave-breaking statistics on wind stress and wave development. In: Banner, M. L. and R. H. J. Grimshaw (Eds.) *Breaking waves IUTAM Symposium* Sydney, Australia, 1991, *Springer Verlag*, 119 - 132.

Keeling, R. F., 1993: On the role of large bubbles in air-sea gas exchange and supersaturation in the ocean. *Journal of Marine Research,* **51**, 237 - 271.

Kent, E. C., T. N. Forester and P. K. Taylor, 1996: A comparison of oceanic skin effect parameterizations using shipborne radiometer data. *Journal of Geophysical Research,* **101, C7**, 16649 - 16666

Kinsman, B., 1965: Wind waves, *Prentice-Hall, Inc., Englewood Cliffs, N. J.*, 676 pp.

Kitaigorodskii, S. A., 1983: On the theory of the equilibrium range in the spectrum of wind-generated gravity waves. *Journal of Physical Oceanography,* **13**,816 - 827.

Kitaigorodskii, S. A., 1984: On the fluid dynamical theory of turbulent gas transfer across an air sea interface in the presence of breaking waves. *Journal of Physical Oceanography,* **14**, 960 - 972.

Kitaigorodskii, S. A., 1992: The dissipation subrange of wind wave spectra. In: Banner, M. L. and R. H. J. Grimshaw (Eds.) *Breaking waves IUTAM Symposium* Sydney, Australia, 1991, *Springer Verlag*, 199 - 206.

Knudsen, V. O., R. S. Alford and J. M. Emling, 1948: Underwater ambient noise. *Journal of Marine Research,* **7**, 410 - 429.

Koga, M., 1982: Bubble entrainment in breaking wind waves. *Tellus,* **34**, 481 - 489.

Komen, G. J., L. Cavaleri, M. Donelan, K. Hasselmann, S. Hasselmann and P. A. E. M. Janssen, 1994: Dynamics and modelling of ocean waves. *Cambridge University Press*, 532 pp.

Lamarre, E. and W. K. Melville, 1991: Air entrainment and dissipation in breaking waves. *Nature,* **351**, 469 - 472.

Lamarre, E. and W. K. Melville, 1992: Instrumentation for the measurement of void-fraction in breaking waves: Laboratory and filed results. *IEEE Journal of Oceanic Engineering,* **17**, 204 - 215.

Lamarre, E. and W. K. Melville, 1994: Void-fraction measurements and sound-speed fields in bubble plumes generated by breaking waves. *The Journal of the Acoustical Society of America,* **95**, 1317 - 1328.

Langmuir, I., 1938: Surface motion of water induced by wind. *Science*, **87**, 119 - 123.

Leibovich, S., 1983: The form and dynamics of Langmuir circulations. *Annual Review of Fluid Mechanics*, **15**, 391 - 427.

Leibovich, S., 1977: On the evolution of the system of wind drift currents and Langmuir circulations in the ocean. Part 1. Theory and averaged current. *Journal of Fluid Mechanics,* **79**, 715 - 743.

Li, M. and C. Garrett, 1993: Cell merging and jet/downwelling ratio in Langmuir circulation. *Journal of Marine Research*, **51,** 737 - 769.

Li, M. and C. Garrett, 1995: Is Langmuir circulation driven by surface waves or surface cooling. *Journal of Physical Oceanography*, **25**, 64 - 75.

Lienhard, J. H. and C. W. van Atta, 1990: The decay of turbulence in thermally stratified flow. *Journal of Fluid Mechanics*, **210**, 57 - 112.

Liljequist, G. H. and K. Cehak, 1984: Allgemeine Meteorologie. *Friedr. Vieweg & Sohn, Braunschweig/Wiesbaden, 3. Auflage*, 404 pp.

Ling, C. S., 1993: Effect of breaking waves on the transport of heat and vapour fluxes from the ocean. *Journal of Physical Oceanography*, **23**, 2360 - 2372.

Liss P. and L. Merlivat, 1986: Air-sea gas exchange rates: Introduction and synthesis. In: Buat-Menard, P. (Ed.): The role of air-sea exchange in geochemical cycling. *D. Reidel Publishing Company*, pp. 113- 127.

Liu, T. W. and J. A. Businger, 1975: Temperature profile in the molecular sublayer near the surface of a fluid in turbulent motion. *Geophysical Research Letters* **2**, 403 - 404.

Longuet-Higgins, M. S., 1992: The crushing of air cavities in a liquid. *Proceedings of the Royal Society of London, Series A*, **439**, 611 - 626.

Longuet-Higgins, M. S. and N. D. Smith, 1983: Measurement of breaking waves by a jump meter. *Journal of Geophysical Research*, **88**, 9823 - 9831.

Longuet-Higgins, M. S. and J. S. Turner, 1974: An 'entrainment plume' model of a spilling breaker. *Journal of Fluid Mechanics*, **63**, 1 - 20.

Mammen, T. and N. von Bosse, 1990: STEP- A temperature profiler for measuring the oceanic thermal boundary layer at the ocean-air interface. *Journal of Atmospheric and Oceanic Technology*, **7**, 312 - 322.

McWilliams, J. C., P. P. Sullivan and C. H. Moeng, 1996: Langmuir turbulence in the ocean. *Journal of Fluid Mechanics*, in press.

Mellor, G. L. and T. Yamada, 1974: A hierarchy of turbulence closure models for planetary boundary layers. *Journal of the Atmospheric Sciences*, **31**, 1791 - 1806. (Corrigenda, 1977, *Journal of the Atmospheric Sciences*, **34**, 1482).

Mellor, G. L. and T. Yamada, 1982: Development of a turbulent closure model for geophysical fluid problems. *Reviews of Geophysics and Space Physics*, **20**, 851 - 875.

Melville, W. K., 1996: The role of surface-wave breaking in air-sea interaction. *Annual Reviews of Fluid Mechanics*, **28**, 279 - 321.

Melville, W. K., 1994: Energy dissipation by breaking waves. *Journal of Physical Oceanography*, **24**, 2041 - 2049.

Melville, W. K. and R. J. Rapp, 1985: Momentum flux in breaking waves. *Nature*, **336**, 54 - 59.

Mitsuyasu, H., 1985: A note on the momentum transfer from wind to waves. *Journal of Geophysical Research*, **90**, 3343 - 3345.

Monahan, E. C., 1993: Occurrence and evolution of acoustically relevant sub-surface bubble plumes and their associated, remotely monitorable, surface whitecaps. In: Natural physical sources of underwater sound, B. R. Kerman. *Kluwer Academic Publishers*. 503 - 517.

Monahan, E. C. and I. G. O'Muirheartaigh, 1986: Whitecaps and the passive remote sensing of the ocean surface. *International Journal of Remote Sensing.*, **7**, 627 - 642.

Mudge, T. D. and R. G. Lueck, 1994: Digital signal processing to enhance oceanographic observations. *Journal of Atmospheric and Oceanic Technology*, **11**, 825 - 835.

Myer, G. E., 1969: A field study of Langmuir circulations. *Proceedings of the 12th Conference on Great Lakes Research held at the University of Michigan, 1969, International Association for Great Lakes Research.* 652 - 663.

Ninnis, R., 1991: Theory of void fraction sensors. *Report, Institute of Ocean Sciences, Sidney, BC* 11 pp.

Olsen, H. O., 1967: Theoretical and experimental investigation of impedance void meters. *Ph.D. Thesis, University of Oslo.* 141 pp.

Osborn, T., D. M. Farmer, S. Vagle, S. A. Thorpe and M. Cure, 1992: Measurements of bubble plumes and turbulence from a submarine. *Atmosphere-Ocean*, **30**, 419 - 440.

Phillips, O. M., 1985: Spectral and statistical properties of the equilibrium range of wind-generated gravity waves. *Journal of Fluid Mechanics*, **156**, 505 - 531.

Phillips, O. M. and M. L. Banner, 1974: Wave breaking in the presence of wind drift and swell. *Journal of Fluid Mechanics*, **66**, 625 - 640.

Plant, W. J., 1982: A relationship between wind stress and wave slope. *Journal of Geophysical Research*, **87**, 1961 - 1967.

Polonichko, V., J. R. Gemmrich and D. M. Farmer, 1997: Thermal inhibition of Langmuir circulation. To be submitted to *Journal of Physical Oceanography*

Prandtl, L., 1925: Bericht über Untersuchungen zur ausgebildeten Turbulenz. *Zeitschrift für angewandte Mathematik und Mechanik*, **5**, 136 - 139.

Rapp, R. J. and W. K. Melville, 1990: Laboratory measurements of deep-water breaking waves. *Philosophical Transactions of the Royal Society of London, Series A*, **331**, 731 - 800.

Richman, J. and C. Garrett, 1977: The transfer of energy and momentum by the wind to the surface mixed layer. *Journal of Physical Oceanography*, **7**, 876 - 881.

Robertson, J. E. and A. J. Watson, 1992: Thermal skin effect of the ocean and its implications for CO_2 uptake. *Nature*, **358**, 738 - 740

Root, S. L. and J. L. Hanson (editors), 1992: Critical Sea Test 7, Phase II Quick-Look Report, *The Johns Hopkins University Applied Physics Laboratory, Laurel, MD.*

Saunders, P. M., 1967: The temperature at the ocean air interface. *Journal of the Atmospheric Sciences*, **24**, 269 - 273

Schlüssel, P., H.-Y. Shin , W. J. Emery and H. Graßl, 1987: Comparison of satellite-derived sea surface temperatures with in situ skin measurements. *Journal of Geophysical Research*, **92**, 2859 - 2874.

Schlüssel, P., W. J. Emery, H. Graßl and T. Mammen, 1990: On the bulk skin temperature difference and its impact on satellite remote sensing of sea surface temperature. *Journal of Geophysical Research*, **95**, 13341 - 13356.

Schönwiese, C. D., 1985: Praktische Statistik. *Gebrüder Bornträger, Berlin - Stuttgart*, 231 pp.

Simpson J. J. and C. A. Paulson, 1980: Small-scale sea surface temperature structure. *Journal of Physical Oceanography*, **10**, 399 - 410

Skyllingstad, E. D. and D. W. Denbo, 1995: An ocean large-eddy simulation of Langmuir circulations and convection in the surface mixed layer. *Journal of Geophysical Research*, **100**, 8501 - 8522.

Skyner, D. J. and C. A. Greated, 1992: The evolution of a long-crested deep-water breaking wave. *Proceedings of the Second (1992) International Offshore and Polar Engineering Conference San Francisco, USA, 14-19 June, 1992*, 132 - 138.

Smith, J. A., 1992: Observed growth of Langmuir circulation. *Journal of Geophysical Research*, **97**, 5651 - 5664.

Smith, S. D., 1981: Coefficients for sea surface wind stress and heat exchange. *Bedford Institute of Oceanography Report Series/BI-R-81-19/December 1981*, 31 pp.

Smith, S. D., 1981: Factors for adjustment of wind speed over water to a 10-metre height. *Bedford Institute of Oceanography Report Series/BI-R-81-3/March 1981*, 29 pp.

Soloviev, A. V, N. V. Vershinsky and V. A. Beverchnii, 1988: Small-scale turbulence measurements in the thin surface layer of the ocean. *Deep Sea Research* **35**, 1859 - 1874.

Stewart, R. W., 1961: The wave drag of wind over water. *Journal of Fluid Mechanics*, **10**, 189 - 194.

Su, M-Y and J. Cartmill, 1992: Breaking waves statistics during 'SWADE'. . In: Banner, M. L. and R. H. J. Grimshaw (Eds.) *Breaking waves IUTAM Symposium* Sydney, Australia, 1991, *Springer Verlag*, 161 - 164.

Terray E. A., M. A. Donelan, Y. C. Agrawal, W. M. Drennan, K. K. Kahma, A. J. Williams III, P. A. Hwang and S. A. Kitaigorodskii, 1996: Estimates of kinetic energy dissipation under breaking waves. *Journal of Physical Oceanography*, **26**, 792 - 807.

Thorpe, S. A., 1982: On the clouds of bubbles formed by breaking wind-waves in deep water, and their role in air-sea gas transfer. *Philosophical Transactions of the Royal Society of London, Series A*, **304**, 155 - 210.

Thorpe, S. A., 1984: The effect of Langmuir circulation on the distribution of submerged bubbles caused by breaking wind waves. *Journal of Fluid Mechanics*, **114**, 237 - 250.

Thorpe, S. A., 1985: Small scale processes in the upper ocean boundary layer. *Nature*, **318**, 519 - 522.

Thorpe, S. A., 1992: Bubble clouds and the dynamics of the upper ocean. *Quarterly Journal of the Royal Meteorological Society*, **118**, 1 - 22.

Thorpe, S. A., 1992b: The breakup of Langmuir circulation and the instability of an array of vortices. *Journal of Physical Oceanography*, **22**, 350 - 360.

Thorpe, S. A., 1993: Energy loss by breaking waves. *Journal of Physical Oceanography*, **23**, 2498 - 2502.

Thorpe, S. A., 1995: Dynamical processes of transfer at the sea surface. *Progress in Oceanography*, **35**, 315 - 352.

Thorpe, S. A. and A. J. Hall, 1982: Observations of the thermal structure of Langmuir circulation. *Journal of Fluid Mechanics*, **114**, 237 - 250.

Thorpe, S. A. and A. J. Hall, 1983: The characteristics of bubble clouds, breaking waves and near-surface currents observed using side-scan sonars. *Continental Shelf Research*, **1**, 353 - 384.

Thorpe, S. A. and A. J. Hall, 1987: Bubble clouds and temperature anomalies in the upper ocean. *Nature*, **328**, 48 - 51.

Thorpe, S. A. and P.N. Humphries, 1980: Bubbles and breaking waves. *Nature*, **283**, 463 - 465.

Toba, Y., H. Kunishi, K. Nishi, S. Kawai, Y. Shimada and N. Shibata, 1971: Study on air-sea boundary processes at the Shirahama Oceanographic Tower Station. *Disaster prevention Institute. Kyoto University Annals*, **148**, 519 - 531 (in Japanese with English abstract).

Trevorrow, M. V. and I. J. Booth, 1995: Extraction of ocean wave directional spectra using steerable Doppler side-scan sonars. *Journal of Atmospheric and Oceanic Technology*, **12**, 1087 - 1100.

Trevorrow, M. V. and R. C. Teichrob, 1994: Self-contained acoustic platforms for probing ocean surface processes. *IEEE Journal of Oceanic Engineering*, **19**. 483 - 492.

Tulin, M. P. and R. Cointe, 1988: Steady and unsteady spilling breakers: Theory. In: Horikawa, K and H. Maruo. (Eds.) *Nonlinear water waves IUTAM Symposium* Tokyo, Japan, 1987, *Springer Verlag*.

Wallace, D. W. R. and C. D. Wirick, 1992: Large air-sea fluxes associated with breaking waves. *Nature*, **356**, 694 - 696.

Weissman, M. A., S. S. Ataktürk and K. B. Katsaros, 1984: Detection of breaking events in a wind-generated wave field. .*Journal of Physical Oceanography*, **14**, 1608 - 1619.

Weller, A. W. and J. F. Price, 1988: Langmuir circulation within the oceanic mixed layer. *Deep-Sea Research*, **35**, 711 - 747.

Woodcock, A. H., 1941: Surface cooling and streaming in shallow fresh and salt waters. *Journal of Marine Research*, **4**, 153 - 161

Woolf, D.. K. and S. A. Thorpe, 1991: Bubbles and the air-sea exchange of gases in near saturation conditions. *Journal of Marine Research*, **49**, 435 - 466.

Wu, J., 1995: Small-scale wave breaking: A widespread sea surface phenomenon and its consequence for air-sea exchanges. *Journal of Physical Oceanography*, **25**, 407 - 412.

Zedel, L. and D. M. Farmer, 1991: Organized structures in subsurface bubble clouds: Langmuir circulation in the open ocean. *Journal of Geophysical Research*, **96**, 8889 - 8900.

Appendix A

A.1 Calibration

A.1.1 Conductivity cell

As seen from Equation 3.2 void fraction is a function of the ratio of conductivity of the sea water to the conductivity of the air-water mixture. Hence, a relation between the recorded voltage V and the specific conductivity σ has to be obtained: $\sigma=\sigma(V)$.

A convenient way of changing conductivity in a controlled manner is to dilute saltwater with fresh water. Conductivity is a known function of temperature and salinity (see *e.g.* Apel [1987]), two quantities easily measured.

All four conductivity cells were set up in a test tank where sea water (salinity 33 ‰, temperature 18°C) was diluted gradually, achieving conductivities ranging from 4.1 S/m to 1.7 S/m. Conductivity of the sample was calculated for five calibration points and a linear regression $\sigma^{-1} = m\,V + b$ obtained, relating the specific resistance (*i.e.* inverse of specific conductivity) to instrument voltage output (Figure A.1).

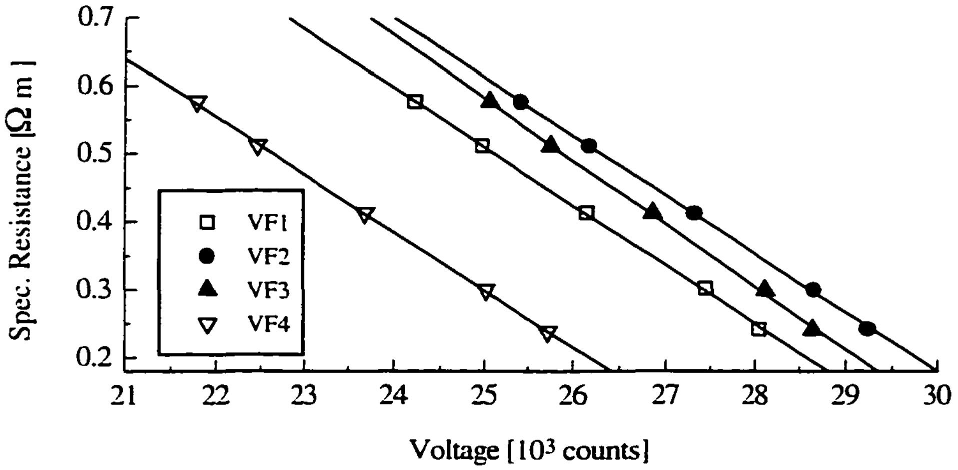

Figure A.1: Calibration curve for four conductivity cells obtained by diluting sea water.

The obtained parameters were tested in an air-bubble calibration tank. The tank consists of a 1.8 m tall Plexiglas tube of 0.3 m diameter mounted on top of a diffuser plate and a differential pressure gauge. Compressed air is released through the diffuser plate at the bottom at an adjustable flow rate, creating variable air fraction in the water in the tank. The air fraction can be calculated from the difference in hydrostatic pressure at two levels. All four conductivity sensors, mounted on a metal pipe in the center of the tank were operating. At each specific air-flow rate the differential pressure as well as the voltage were averaged over 2 minutes. Due to the geometry of the tank air-fractions of up to 25% are feasible. The results of one calibration run are shown in Figure A.2. Sensor VF3 is in excellent agreement with the calibrated void fraction. Sensor VF1 and VF2 being located further up in the tank show higher void fraction readings than obtained from the differential pressure gauge and sensor VF4 too low values. This is understandable since the rather large air bubbles created by the diffuser plate increase in size as they rise, resulting in a vertical gradient of void fraction in the tank. Hence, we conclude that the inferred void fraction from all four conductivity cells is in good agreement with the actual values.

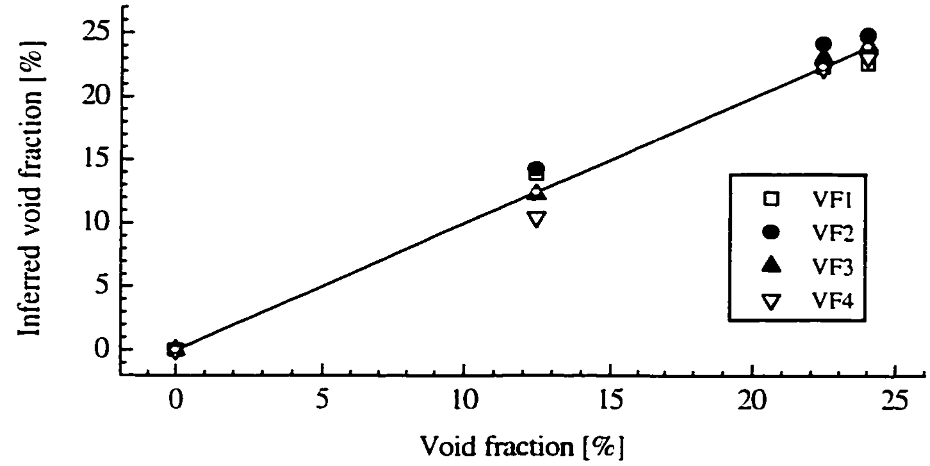

Figure A.2: Test of conductivity cell calibration in an air-bubble calibration tank.

The performance at small conductivity (large air-fractions) had to be tested with the aid of variable, but known resistors. The sensor was equipped with three resistors of equal value between adjacent pairs of sensor electrodes, while the system was operating in air. For resistances up to 18 Ω the voltage increased linearly (Figure A.3) However, at approximately 20 Ω the voltage reaches a maximum (minimum output in digital counts, since the A/D inverts the signal) and for larger resistances the transmitter is working in a nonlinear way. The expected voltage drop cannot be supplied by the transmitter so that the receiver records an apparent voltage decrease with increasing resistance. This leads to a double valued functional dependence between the recorded voltage and resistance. Using the 1 Ω reading as reference value for 0 % void, the equivalent void fraction has been calculated (Figure A.3). For void fractions up to approximately 85 %, corresponding to conductivities above 0.6 S/m, the instrument follows the linear behavior, leaving only extreme large air fractions of 85 % to 100 % without calibration. Such large air fractions have not been observed within breaking waves, and hence the nonlinear transmitter range is only of significance when the sensor breaks through the water-air interface. Please note that for the April 1995 experiment the linear range of the transmitter has been increased to resolve conductivities as low as 0.3 S/m, which eliminated the double valued behaviour of the resistance/voltage dependence.

The proximity of the surface influences the electrical field induced by the sensor electrodes and gives biased results, if the sensor comes too close to the air-water interface. To examine this effect the sensor was initially positioned 0.27 m below the water surface and raised gradually until the sensor was completely out of the water (Figure A.4). Up to a surface proximity of 40 mm the signal is not biased. However, when the top electrode touches the interface an erroneous void fraction of 20 % is introduced, which increases further until the interface is located between the second and the third electrode. As the probe is raised beyond, the resistance between the electrodes approaches infinity and the transmitter responds non linearly, i.e. the voltage output decreases.

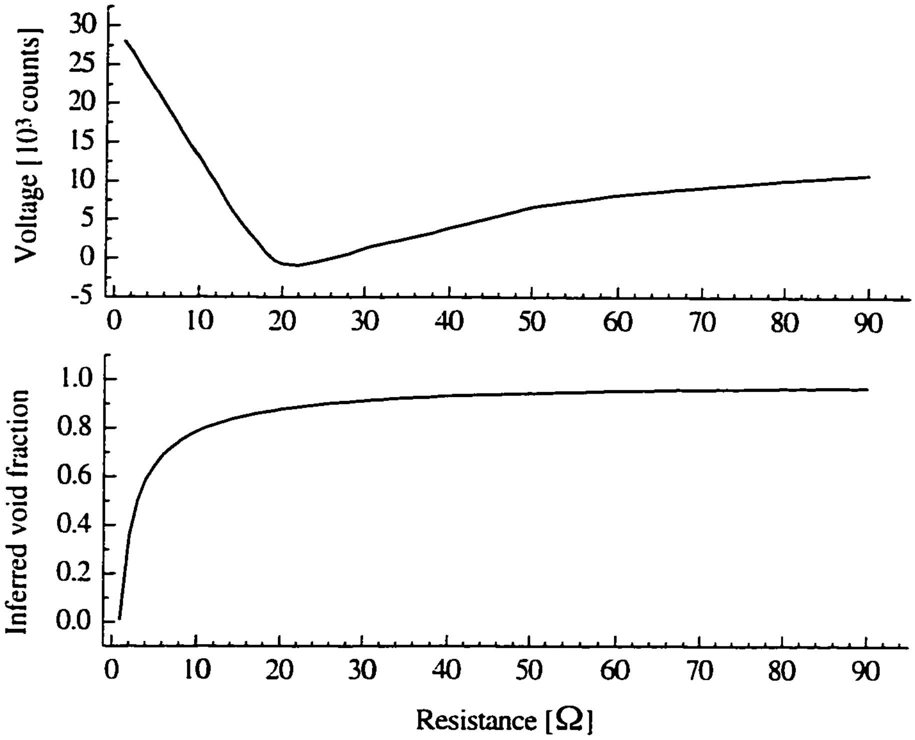

Figure A.3: Instrument response to variable resistance across the electrodes of a conductivity cell. The bottom panel shows void fraction inferred from measured voltage output.

The new design of the conductivity cells for the April 1995 experiment allowed a surface proximity of less than 20 mm without detectable apparent void fraction.

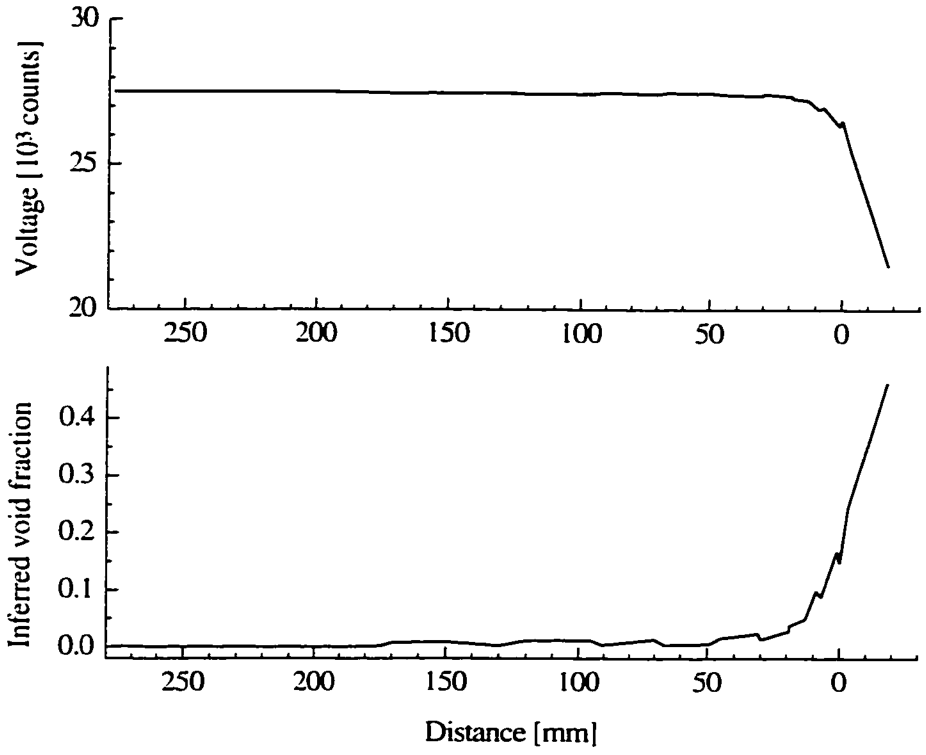

Figure A.4: Instrument response to proximity of conductivity cell to sea-air interface. Depth is measured from the top of the upper electrode. Lower panel shows apparent air fraction caused by surface proximity. (Sensor version December 1993).

A.1.2 Thermistors

A thermistor (a contraction of the words "thermal resistor") has a specific non linear temperature-resistance characteristic, which has to be calibrated. Since in practical applications the thermistor is part of a Wheatstone Bridge we are interested in the functional dependence of voltage across the Wheatstone Bridge versus temperature. Therefore the thermistors were held in a controlled temperature bath while the instrument was recording the voltage output. The calibration was carried out in the calibration facilities at the Institute of Ocean Sciences. Seven calibration points were obtained in the temperature range 0 °C - 20 °C for two sets of thermistors. Reference temperature was taken as the average of 4 bath-internal thermistors. Because of the thermal micro structure in the calibration tank the reference temperature and thermistor readings were averaged over one minute. After starting the instrument a period of at least fifteen minutes was allowed to warm up the electronics and a minimum of ten minutes after changing thermistors. A period of at least eight hours was allowed to stabilize the bath temperature. A third order polynomial between the temperature (in degree Celsius) and the recorded voltage (in digital counts) was fitted through the calibration points for each thermistor. The accuracy of this method is estimated as 1 mK.

A.1.3 Capacitance wire gauge

The capacitance wire gauge, often used in wave measurements and therefore commonly called capacitance wave height gauge, measures the capacity between the centre conductor (the wire) and the seawater. A Teflon insulator serves as dielectric. Internal electronics provided by the manufacturer convert changes of the capacity into a changing voltage which gets recorded by the main instrument electronics, in our case at a sampling rate of 343.75 Hz. A linear relationship between water height and output voltage makes for a straightforward calibration procedure. Seven calibration points ranging ± 0.22 m from the midpoint of the wire were taken in a tank filled with saltwater of 31‰ salinity at 17°C. The linear regression between water height and recorded voltage with a regression coefficient $r = 0.983$ provides a very accurate estimate of the height in undisturbed water.

In order to test the performance of the wave height gauge in an air-water mixture the device was set up in the air-bubble calibration tank (see Appendix A 1.1). Since large air-fractions create a rather irregular surface, a floating lid made of 15 mm thick ethafoam was added to the calibration tank. A hole of 10 mm diameter allowed the wire to pass through and several holes closer to the edge were added for the air to escape. Air was released into the water column via six diffusers, spanning the range from the surface to 0.3 m depth at approximately even spacing. This generates a layer of air-water mixture with increasing air fraction closer to the surface, similar to conditions within a breaking wave. The height of the water column, including the bubble layer is determined by the bottom of the floating lid and is measured with a tape measure attached to the side of the tank. Accuracy of this method is estimated at better than 5 mm. This true water height is compared with the recording of the wire gauge. A mean air fraction for each calibration point is given by the expansion of the water column above the deepest diffuser. This provides a lowest bound for the actual air fraction of the water close to the wire since air concentration is much higher in the vicinity of the diffusers, which are approximately 10 mm to the side of the wire. Four calibration points were taken. At a mean air fraction of 2.5% true and recorded height of the air water column were exactly the same. At 4.5% air fraction a discrepancy of 3 mm was observed, which lies within the error bounds of the surface estimation. However, for a mean air fraction of 7.2% the wire gauge recording was 7.3 mm too low. This error increased to 20.4 mm at 15.7% air fraction. This indicates an underestimation of the surface height of an aerated water column of large air fractions.

The main purpose of the capacitance wire gauge in our application is to provide evidence for a minimum sensor depth during breaking events, and therefore the observed bias of the wire gauge only tightens the criterion. No apparent breaking event due to the conductivity sensor approaching the surface remains undetected.

A.2 Conductivity sensor breaking through the water-air interface

In rough sea and steep waves the sensor boom sometimes can not follow the surface rapidly enough and the top sensor breaks through the water-air interface. Before the modifications for the April 1995 experiment this resulted in spurious void fraction signals. In order to recognize and subsequently eliminate these cases a series of tests were conducted.

In the first test one conductivity cell and thermistor were mounted on a separate pipe similar to the sensor boom of the instrument. The instrument itself, equipped with one conductivity cell and fixed resistors on the remaining two channels as well as three thermistors in water and one in air, was floating in undisturbed sea water nearby. During the first part of the test the separated sensor has been moved rapidly through the water interface for several times. The amount of air-entrainment and splash created hereby varied. In the second part the sensor was kept at about 5 - 10 cm depth and rotated rapidly back and forth. This sensor movement entrained enough air to create bursts of large air fractions similar to a breaking wave. Short time series of these tests are given in Figure A.5 and Figure A.6.

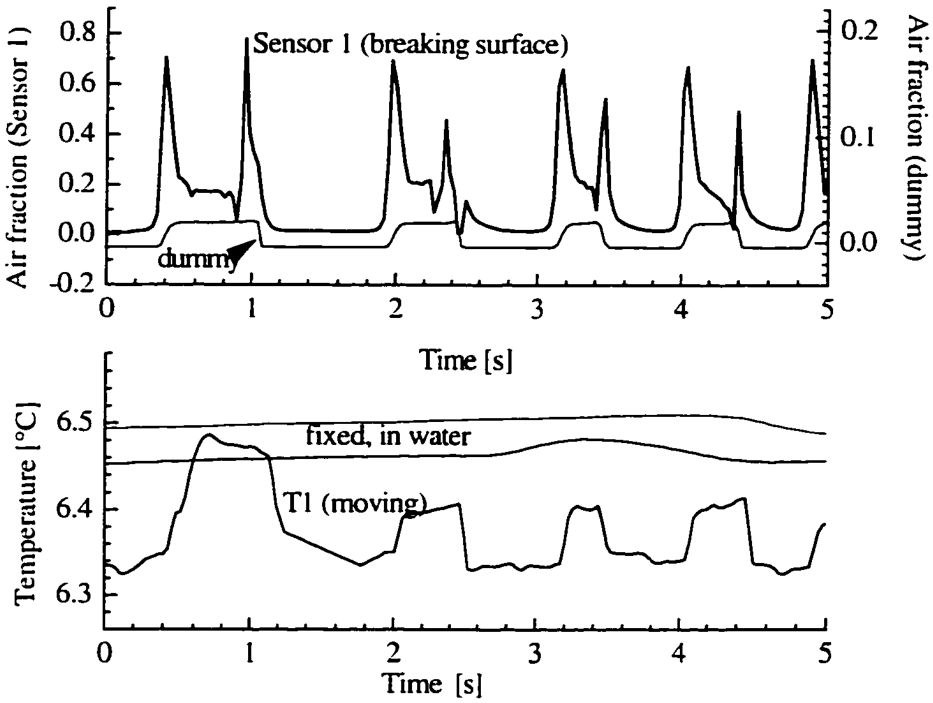

Figure A.5: Air fraction and temperature for a conductivity/thermistor cell breaking the sea-air interface. Also shown is the response of a dummy conductivity cell connected to a second void fraction channel and temperature records of two thermistors in undisturbed water nearby. (Sensor version December 1993).

The first part of the test revealed a characteristic double peaked signal when the sensor breaks through the water-air interface. As the sensor approaches the interface, the air fraction rises rapidly to a maximum value of about 0.7. Then it falls off to an in-air reading of approximately 0.2. The second peak occurs when the sensor re-submerges in water with subsequent increasing water fraction in the sample volume. This behaviour is in accordance with the findings in section A1.1. Due to delay in the recovery of the A/D converter from high voltage drops (i.e. large air fractions) the other conductivity channels produce an apparent air-fraction reading of 0.02.

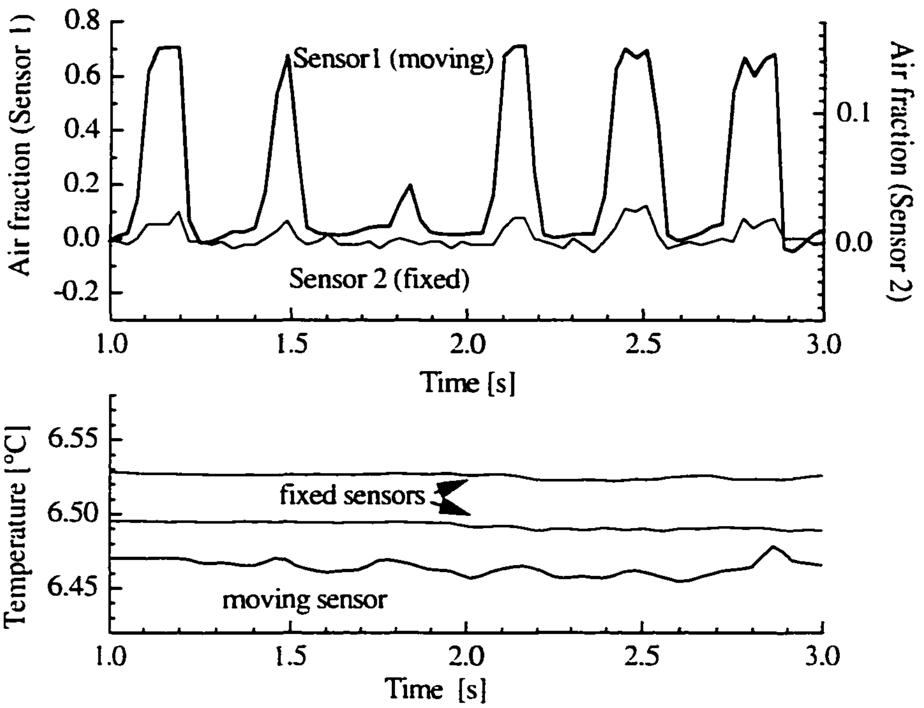

Figure A.6: Cross talk of conductivity cells and thermistors in large air fractions. (Sensor version December 1993).

The temperature record of the moving sensor shows a temperature increase of 0.3 - 0.4 K within approximately 30 ms, in some cases followed by a slow increase of approximately 0.1 K over the remaining time the sensor spent within air. The air-sea temperature difference during the test was 1.8 K under light wind conditions. A variable signal in one channel has no influence on the reading in other channels, *i.e.* there is no cross talk between thermistor channels.

Large air fraction (up to 70%) was realized in the second part of the test (Figure A.6). If the sensor does not emerge into the air no saturation of the electronics occurs, and hence no apparent drop in air fraction is observed. However, there is still a significant spurious signal (up to 0.02) on the recording of the second sensor within undisturbed water. This limits our resolution of the lower conductivity cells to signals larger than 2% air fraction.

As the water in the top few centimeters is well mixed, the temperature fluctuations are smaller than 10 mK, again showing no cross-talk with the other thermistors.

Appendix B

B.1. Thermistor reading in air-water mixture

The apparent temperature cross section in a bubbly air-water mixture detected by a thermistor depends mainly on three parameters: a) The equilibration of air to the surrounding water temperature. b) The time response of the thermistor in air and c) the time response of the thermistor in water.

Following formation of an air bubble within water of different temperature, diffusion of heat through the bubble-skin and within the air bubble will tend to equalize the temperature. The rate at which equilibrium is approached depends upon the heat diffusivity and bubble radius. Since the water temperature does not change significantly due to heat transfer from the bubble, it may be taken as constant for the purpose of calculation. The equilibration process is described by diffusion for a sphere:

$$\frac{\partial T}{\partial t}=\frac{k_t}{r^2}\frac{\partial}{\partial r}\left(r^2\frac{\partial T}{\partial r}\right)$$

$$T=0 \quad \text{for} \quad r<a,\ t=0,$$
$$T=T_a \quad \text{for} \quad r=a,\ t\geq 0, \tag{B.1}$$

where a is the radius of the bubble, T_a the water temperature and k_t the thermal diffusivity of air. Note that this neglects mixing of air within the bubble, and therefore leads to a lower bound on the calculated time taken to reach equilibrium. The solution for the average temperature T_{av} in the bubble is [Carslaw & Jaeger, 1959]:

$$\frac{T_{av}}{T_a}=6\sqrt{\frac{\zeta}{\pi}}-3\zeta+12\sqrt{\zeta}\sum_{n=1}^{\infty} ierfc\frac{n}{\sqrt{\zeta}},$$
$$\zeta=\frac{k_t t}{a^2}. \tag{B.2}$$

Figure B1 shows the temperature equilibration of bubbles as a function of time in a non-dimensional form, according to Equation B.2. For an initial temperature of the bubble 0.5 K higher than the water temperature, corresponding to our average deployment conditions and $k_t=1.5\times10^{-5}\,m^2s^{-1}$, it is seen that only bubbles of diameter larger than 6 mm take more than 0.2 s (the estimated minimum time for the bubble to reach the sensor depth) to equilibrate to within 1%. However, larger bubbles with diameter greater than 10 mm show significant temperature deviations up to a time of 0.5 s after injection.

The response of a thermistor to a step like temperature change is governed by the heat transfer equation:

$$\frac{dT}{dt} = -\frac{T - T_A}{\tau} \tag{B.3}$$

with following solution:

$$T = T_A + (T_i - T_A)e^{-t/\tau}, \tag{B.4}$$

where T_i is the initial temperature of the thermistor, T_A is the ambient temperature and τ is the thermal time constant of the device. τ is specified by the manufacturer as $\tau = 0.1$ s in air and $\tau = 0.007$ s when the thermistor is in water.

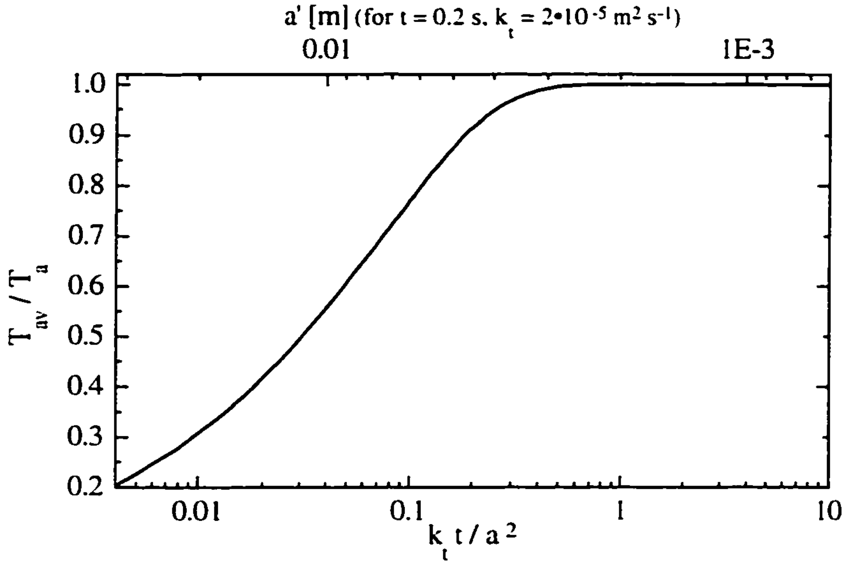

Figure B.1: Temperature equilibration of a sphere of temperature T_{av} to the surrounding temperature T_a as a function of radius a, time t and diffusivity k_t. At the top of the figure, the scale is shown for radius a', in the case of air-bubbles with $k_t = 1.5 \times 10^{-5} m^2 s^{-1}$ after a time t = 0.2 s. For example, a 3 mm radius bubble would reach equilibrium within the 0.2 s period.

We modeled the apparent temperature reading of our thermistor type in an air-water mixture of spherical bubbles of uniform size. The initial air temperature was set to be 0.5 K higher than the water temperature and we assumed no bubble would reach the thermistor depth within the first 0.2 s. The separation of adjacent bubbles was fixed at 1 mm. This represents a rather extreme example in which all the bubbles are perfectly aligned. Since the thermistor will be covered with a thin water layer even within the air bubble the thermal time constant in air has to be increased. An estimate for the thermal time constant of a wet thermistor of $\tau = 0.2$ s was obtained from dockside tests in which the thermistor breaks the water surface. Note that the additional air flow in the atmospheric boundary layer reduces τ towards a lower value than expected within an air bubble. The bubbles are advected past the thermistor by a constant flow speed v_d which is dominated by the rise speed of the bubbles. The rise speed is a function of bubble size and contamination of the water and ranges for bubbles of diameter 1 mm to 20 mm between 0.2 m/s and 0.3 m/s [Cliff *et al.*, 1978], although it should be recognized that advection may often be more important than bubble rise speed in still water.

Figure A2 shows temperature deviations as seen by the thermistor for three different bubble sizes and two different flow speeds. Due to the short equilibration time of small bubbles essentially no temperature anomaly would be recorded at our sensor depth under the assumptions stated above, for a bubble diameter less than 6 mm. Bubbles with diameter of 10 mm or larger are still noticeably warmer than the surrounding water and the time needed to traverse the bubble is long enough for the thermistor to respond. For a 1 mm separation between bubbles, the water layer between adjacent bubbles is not thick enough to cool the thermistor completely down to the water temperature resulting in a saw-tooth like temperature curve. For increased flow speed of $v_d = 1$ m/s the time spent between bubbles is too short to allow the thermistor to respond and therefor the air temperature would be recorded. However, there is strong evidence from observational and theoretical work [Longuet-Higgins, 1992] that the majority of bubbles have radii smaller than 2.5 mm. This is consistent with the subsurface video recordings in which individual bubbles of radius larger than 5 mm could only occasionally be detected in a cloud of smaller bubbles. We therefore conclude that only in rare cases when the sensor passes through larger air cavities of several centimeters diameter in plunging breakers, will the air temperature dominate the observed signal. These cases were recognized by the particular shape of the temperature signal as well as the video recording and were eliminated from the subsequent data analysis.

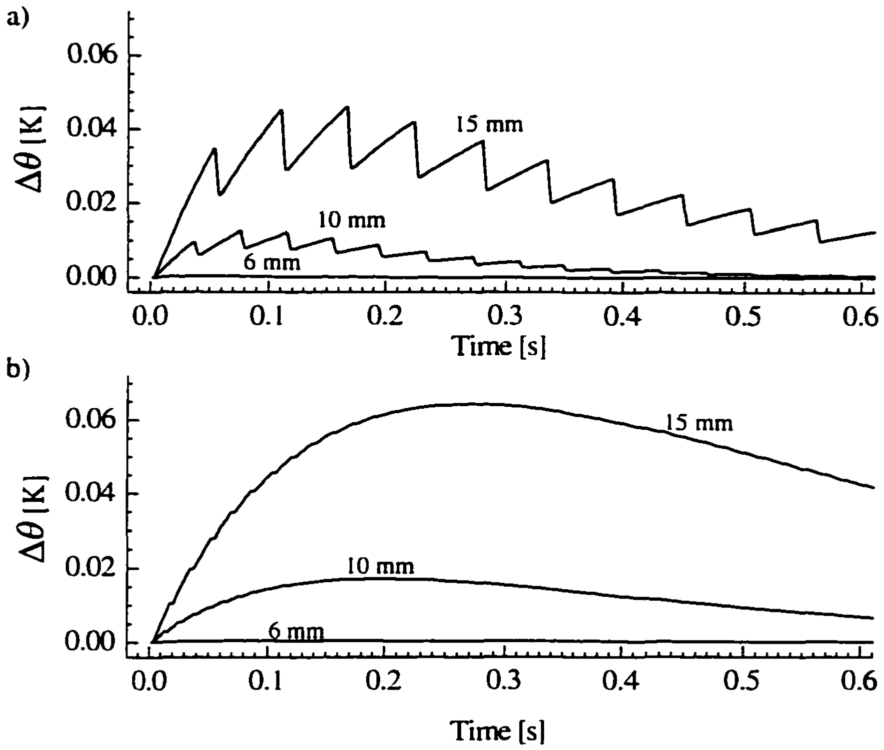

Figure B.2: Modeled temperature record of the thermistor in air bubbles of stated diameter separated by 1 mm water. The temperature of the air bubble was initially 0.5 K higher than the water temperature and prior to the 0.2 s transit time to the thermistor. a) For a bubble flow speed $v_d = 0.3$ m/s, b) for $v_d = 1.0$ m/s

Appendix C Temperature profiles

In the following 54 examples of observed temperature profiles are presented. Each plot shows the first six complete profiles at the beginning of the hour, thus providing an overview of encountered conditions.

Figure C.1 (Next nine pages): Observed near surface temperature profiles. Times of measurements are provided on each subplot.

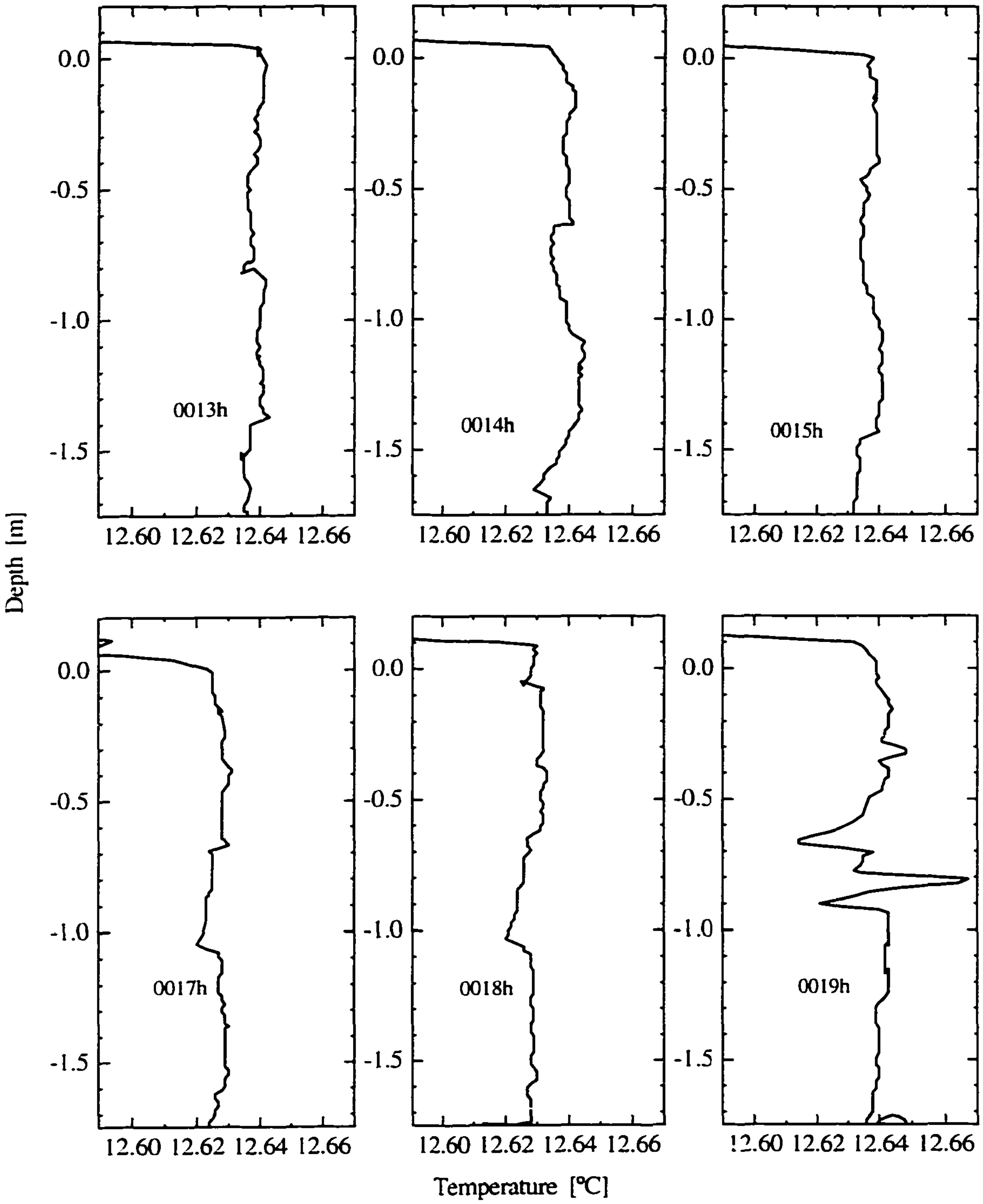
Depth [m]
0.0
-0.5
-1.0
-1.5
0013h
0014h
0015h
0017h
0018h
0019h
12.60 12.62 12.64 12.66
Temperature [°C]

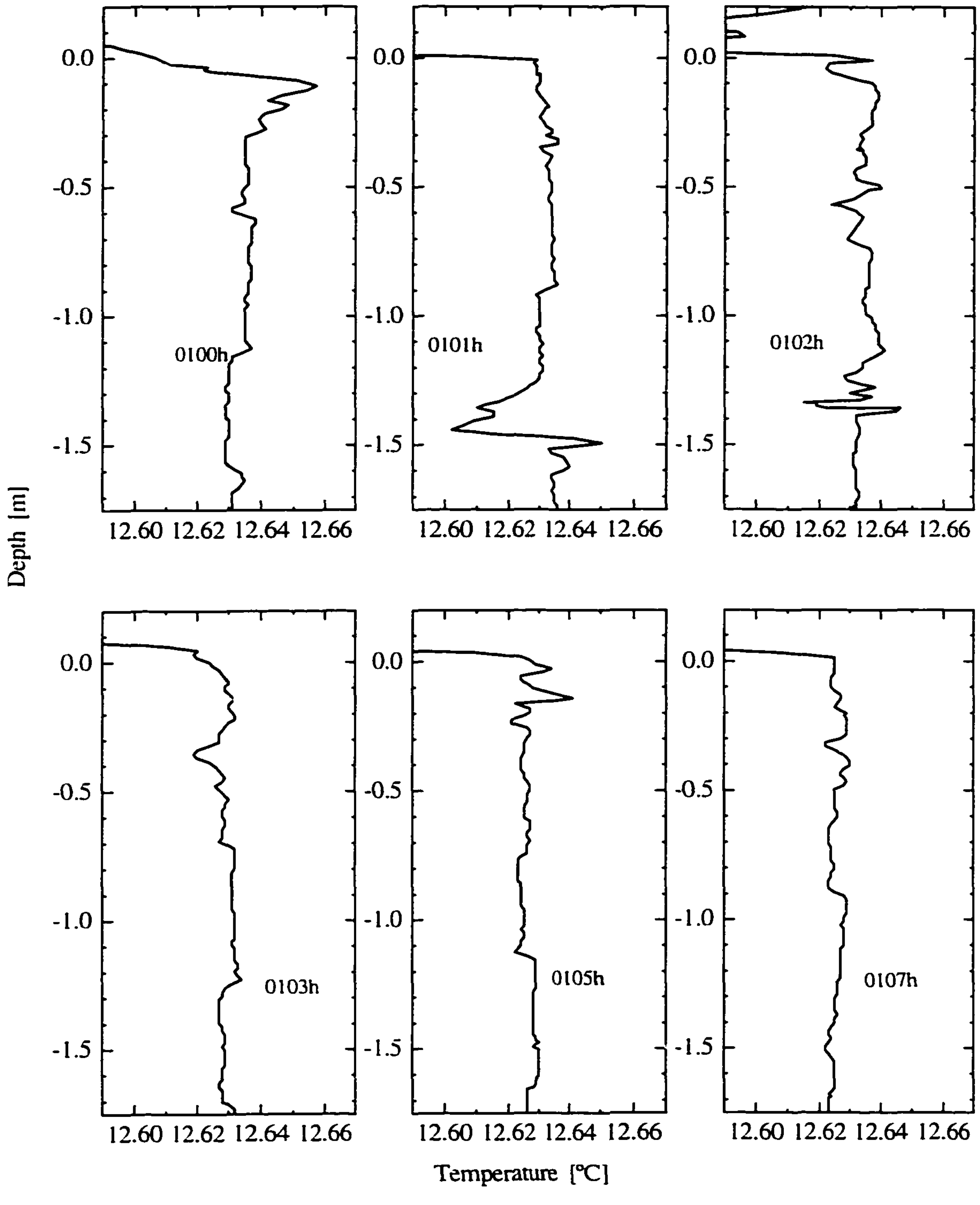
0100h
0101h
0102h
0103h
0105h
0107h
0.0
-0.5
-1.0
-1.5
12.60 12.62 12.64 12.66
Depth [m]
Temperature [°C]

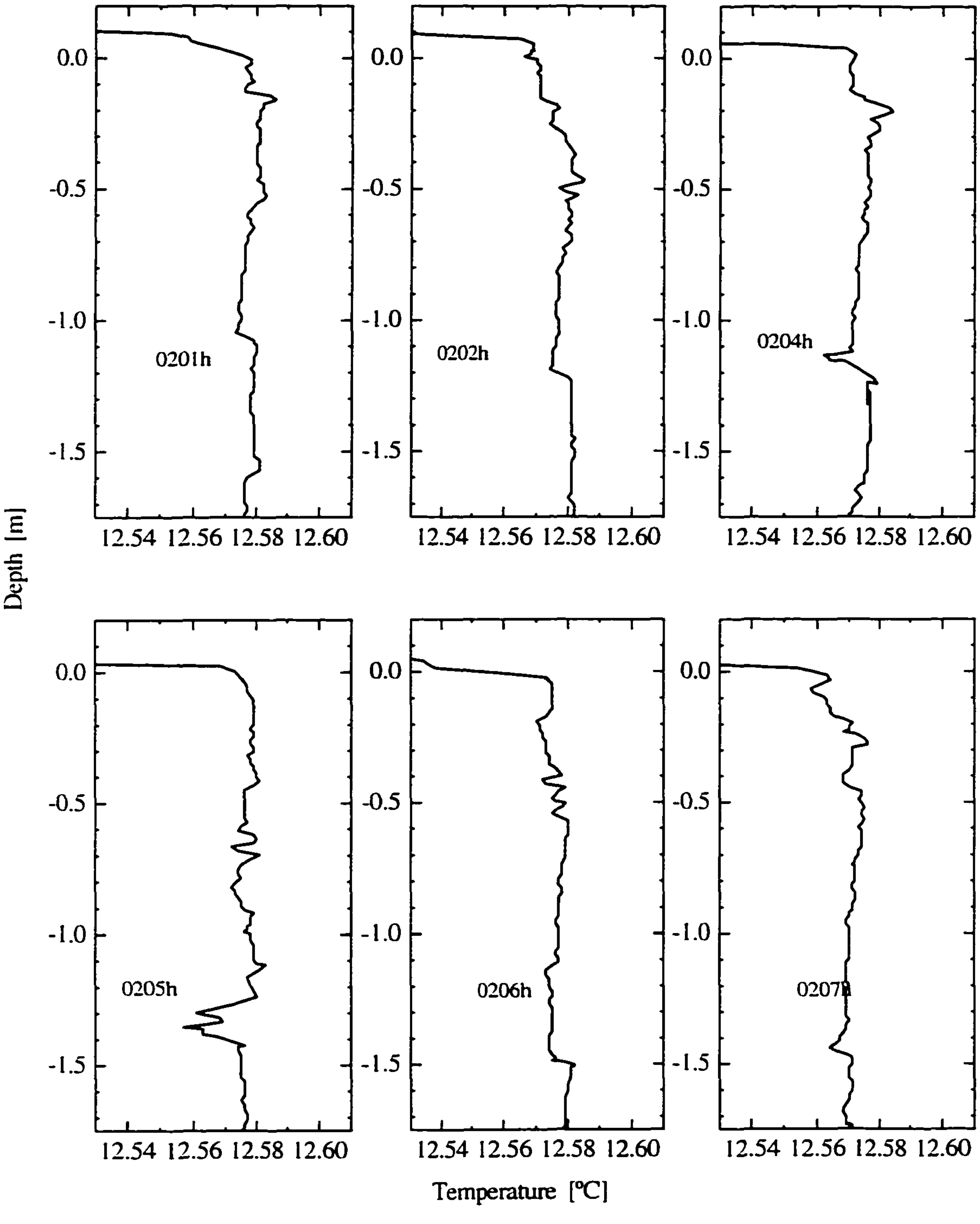
0201h
0202h
0204h
0205h
0206h
0207h
0.0
-0.5
-1.0
-1.5
12.54 12.56 12.58 12.60
Depth [m]
Temperature [°C]

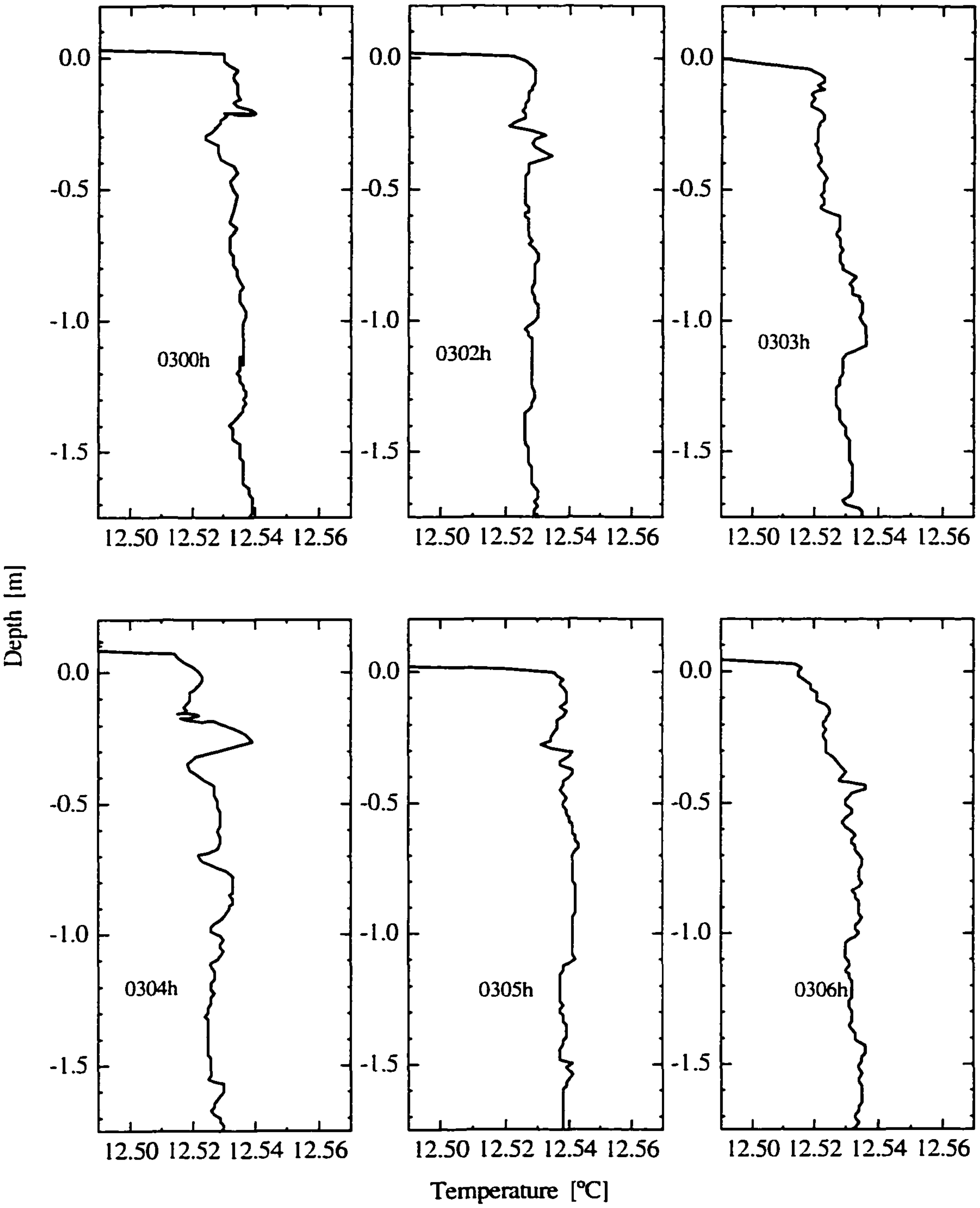
0300h
0302h
0303h
0304h
0305h
0306h
0.0
-0.5
-1.0
-1.5
12.50 12.52 12.54 12.56
Depth [m]
Temperature [°C]

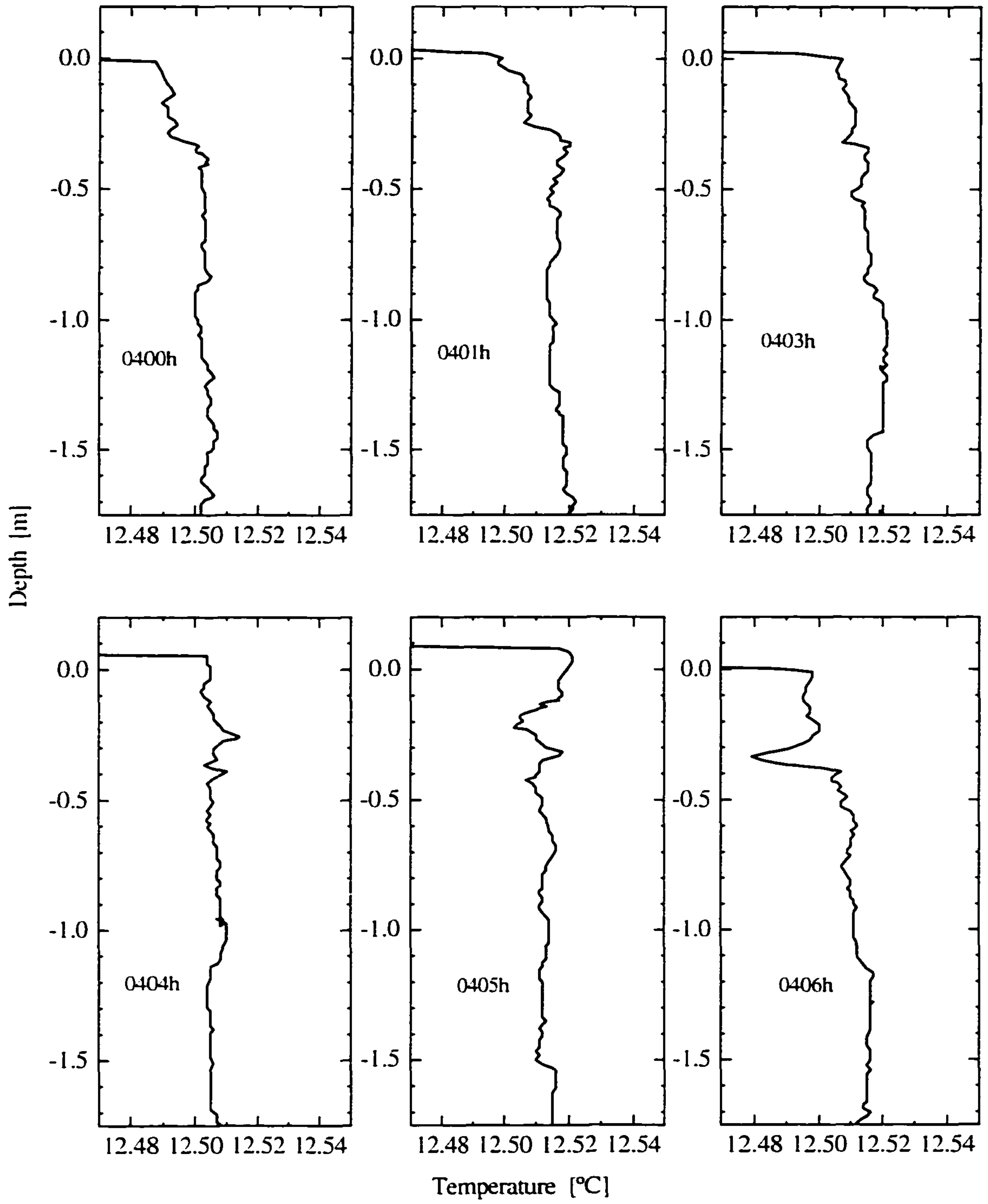
0400h
0401h
0403h
0404h
0405h
0406h
0.0
-0.5
-1.0
-1.5
12.48 12.50 12.52 12.54
Depth [m]
Temperature [°C]

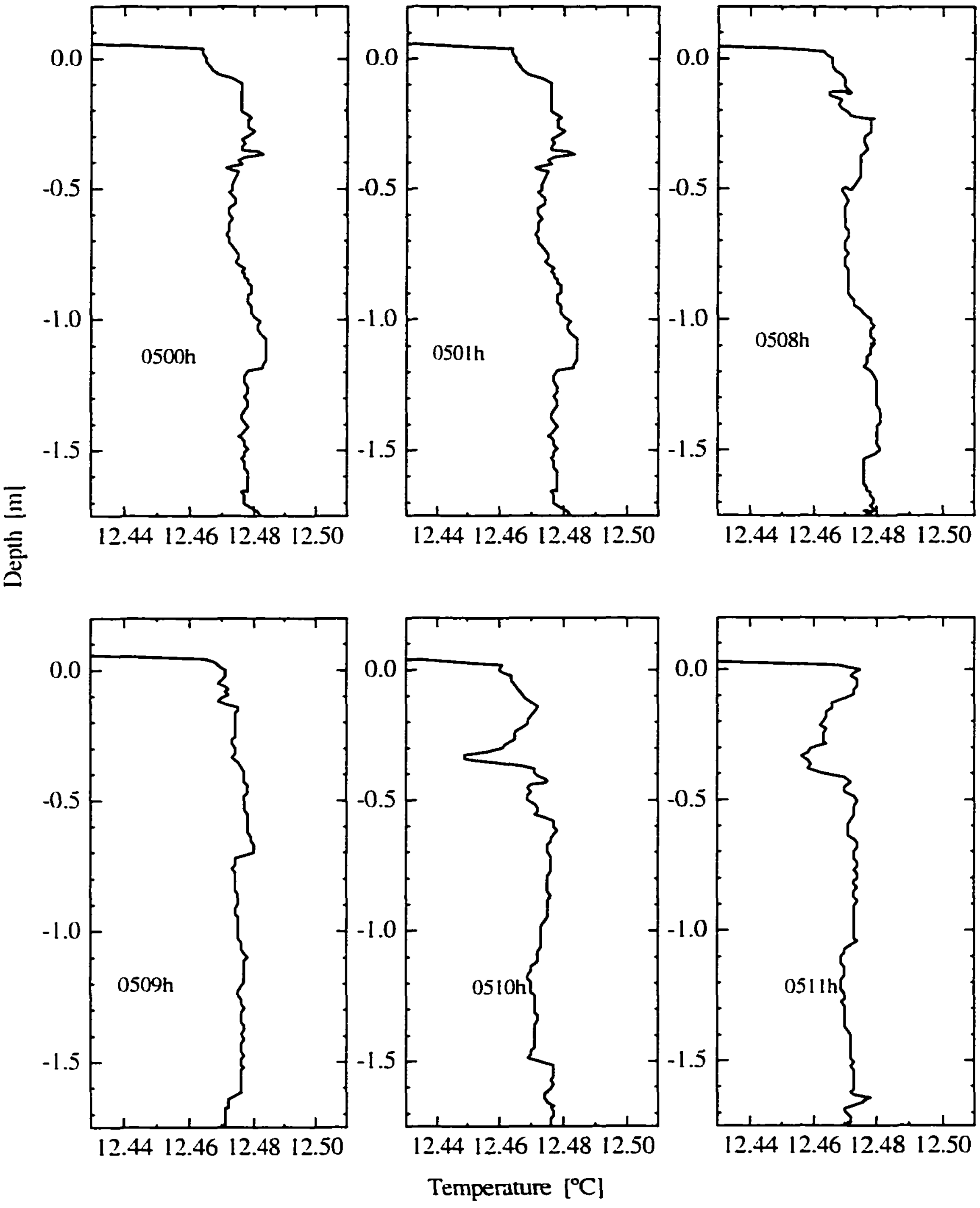
0500h
0501h
0508h
0509h
0510h
0511h
0.0
-0.5
-1.0
-1.5
12.44 12.46 12.48 12.50
Depth [m]
Temperature [°C]

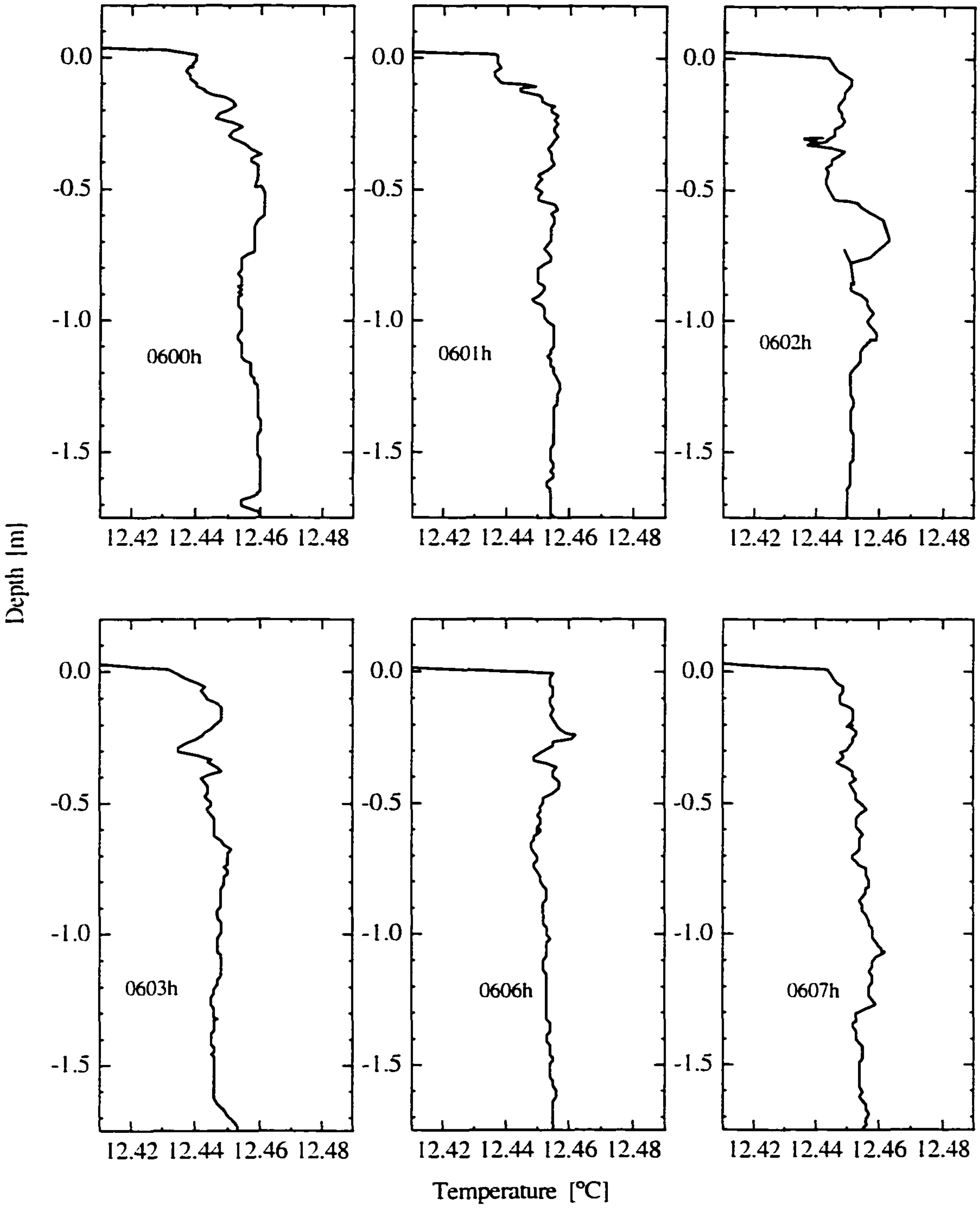
0600h
0601h
0602h
0603h
0606h
0607h
0.0
-0.5
-1.0
-1.5
12.42 12.44 12.46 12.48
Depth [m]
Temperature [°C]

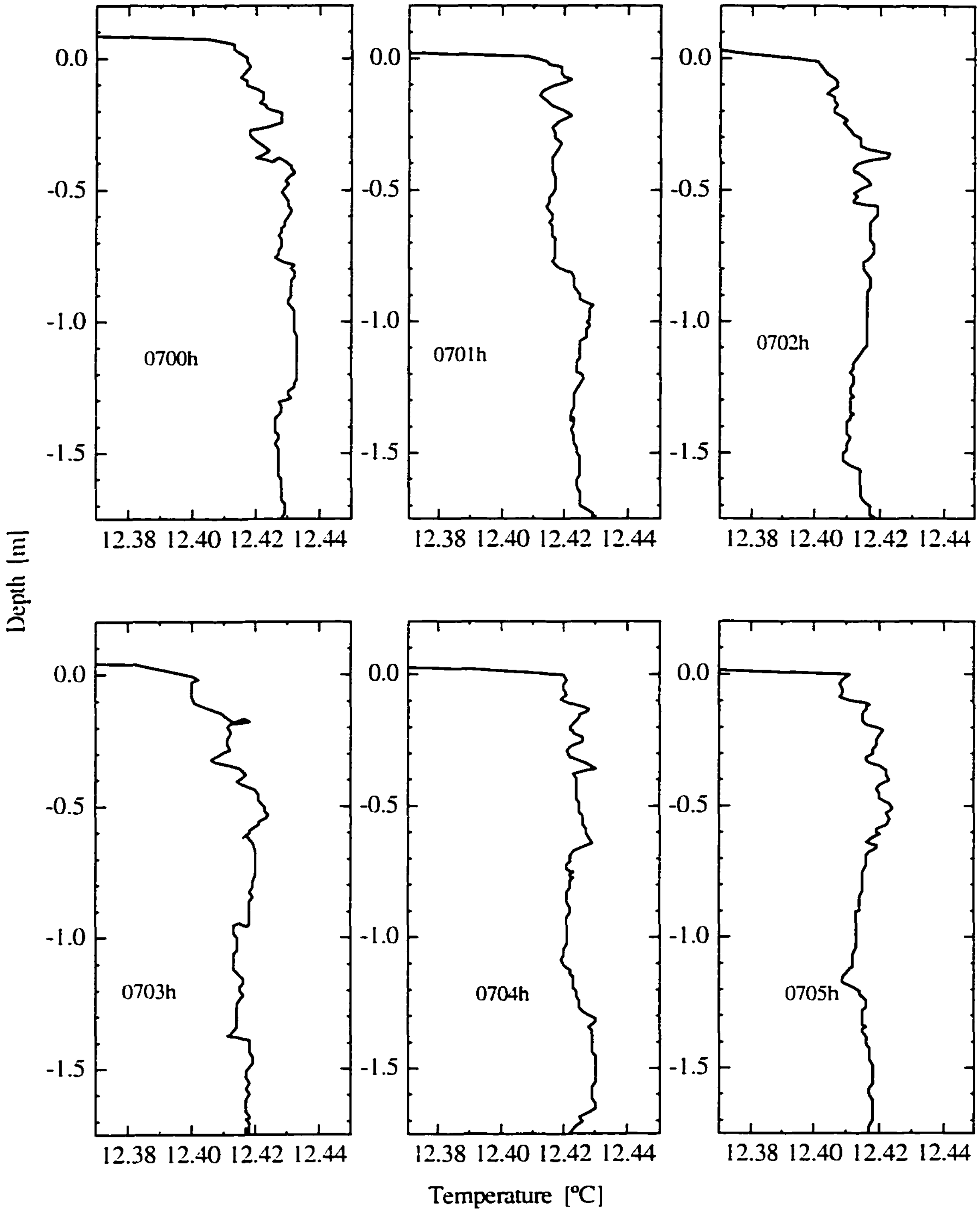
0700h
0701h
0702h
0703h
0704h
0705h
0.0
-0.5
-1.0
-1.5
12.38 12.40 12.42 12.44
Depth [m]
Temperature [°C]

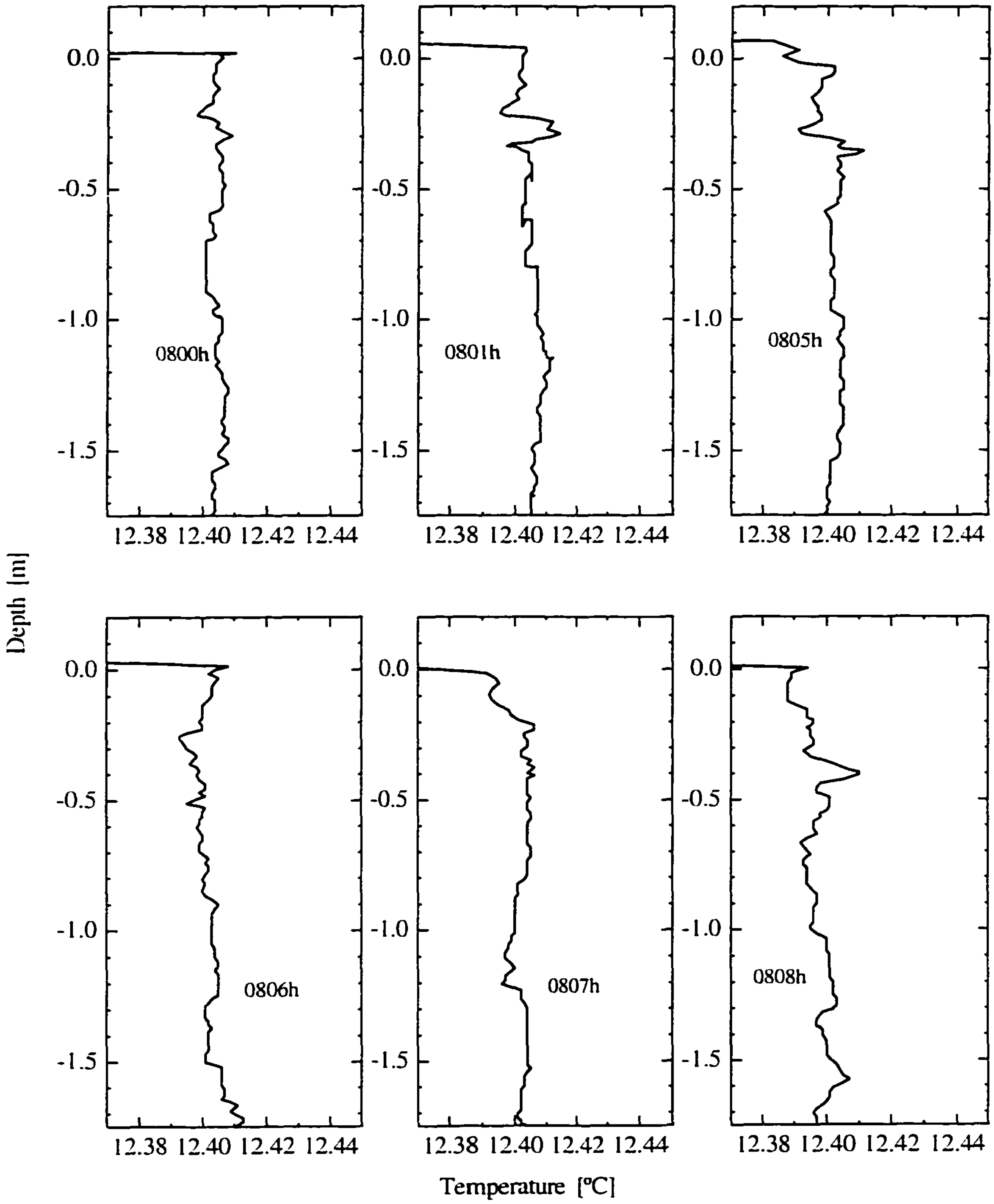
0800h
0801h
0805h
0806h
0807h
0808h
0.0
-0.5
-1.0
-1.5
12.38 12.40 12.42 12.44
Depth [m]
Temperature [°C]